August 2018

Novel Algorithms for Merging Computational Fluid Dynamics and 4D Flow MRI

Ali Bakhshinejad
University of Wisconsin-Milwaukee

Novel Algorithms for Merging Computational Fluid Dynamics and 4D Flow MRI

by

Ali Bakhshinejad

A Dissertation Submitted in

Partial Fulfillment of the

Requirements for the Degree of

Doctor of Philosophy

in Engineering

at

The University of Wisconsin–Milwaukee

August 2018

Abstract

Novel Algorithms for Merging Computational Fluid Dynamics and 4D Flow MRI

by

Ali Bakhshinejad

The University of Wisconsin–Milwaukee, 2018
Under the Supervision of Professors Roshan M. D'Souza And Vitaliy L. Rayz

Time-resolved three-dimensional spatial encoding combined with three-directional velocity-encoded phase contrast magnetic resonance imaging (termed as 4D flow MRI), can provide valuable information for diagnosis, treatment, and monitoring of vascular diseases. The accuracy of this technique, however, is limited by errors in flow estimation due to acquisition noise as well as systematic errors. Furthermore, available spatial resolution is limited to 1.5mm - 3mm and temporal resolution is limited to 30-40ms. This is often grossly inadequate to resolve flow details in small arteries, such as those in cerebral circulation. Recently, there have been efforts to address the limitations of the spatial and temporal resolution of MR flow imaging through the use of computational fluid dynamics (CFD). While CFD is capable of providing essentially unlimited spatial and temporal resolution, numerical results are very sensitive to errors in estimation of the flow boundary conditions. In this work, we present three novel techniques that combine CFD with 4D flow MRI measurements in order to address the resolution and noise issues. The first technique is a variant of the Kalman Filter state estimator called the Ensemble Kalman Filter (EnKF). In this technique, an ensemble of patient-specific CFD solutions are used to compute filter gains. These gains are then used in a predictor-corrector scheme to not only denoise the data but also increase its temporal and spatial resolution. The second technique is based on proper orthogonal decomposition and ridge regression

(POD-rr). The POD method is typically used to generate reduced order models (ROMs) in closed control applications of large degree of freedom systems that result from discretization of governing partial differential equations (PDE). The POD-rr process results in a set of basis functions (vectors), that capture the local space of solutions of the PDE in question. In our application, the basis functions are generated from an ensemble of patient-specific CFD solutions whose boundary conditions are estimated from 4D flow MRI data. The CFD solution that should be most closely representing the actual flow is generated by projecting 4D flow MRI data onto the basis vectors followed by reconstruction in both MRI and CFD resolution. The rr algorithm was used for between resolution mapping. Despite the accuracy of using rr as the mapping step, due to manual adjustment of a coefficient in the algorithm we developed the third algorithm. In this step, the rr algorithm was substituted with a dynamic mode decomposition algorithm to preserve the robustness. These algorithms have been implemented and tested using a numerical model of the flow in a cerebral aneurysm. Solutions at time intervals corresponding to the 4D flow MRI temporal resolution were collected and downsampled to the spatial resolution of the imaging data. A simulated acquisition noise was then added in k-space. Finally, the simulated data affected by noise were used as an input to the merging algorithms. Rigorous comparison to state-of-the-art techniques were conducted to assess the accuracy and performance of the proposed method. The results provided denoised flow fields with less than 1% overall error for different signal-to-noise ratios. At the end, a small cohort of three patients were corrected and the data were reconstructed using different methods, the wall shear stress (WSS) was calculated using different reconstructed data and the results were compared. As it has been shown in chapter 5, the calculated WSS using different methods results in mutual high and low shear

stress regions, however, the exact value and patterns are significantly different.

Table of Contents

List of Figures

List of Tables

Chapter 1

Introduction

1.1 Physiology

A cerebral aneurysm is an abnormal dilation of an artery usually near arterial bifurcation in circle of Willis (Fig. 1.1). The disease is the result of weakening of the intima layer of the blood vessel which results in ballooning of the lumen into an abnormal shape.

The incremental improvement in the resolution of cerebral medical imaging techniques such as MRI and CT in the recent years resulted in more incidental findings of this type of disease which some believe is as high as 7% [139, 127]. Due to poor results in treatment of subarachnoid hemorrhage (SAH) which are 40% fatal [64] there is a pressing request from the clinicians to be provided with a new patient-specific metric for evaluating the current stage and future development of the disease.

Currently, in case of aneurysm finding, the clinician needs to choose between treatment and observation based on available risk factors such as: age, gender, location and size of the disease, and other family history of SAH or similar aneurysms [64]. A better understanding of patient-specific hemodynamics can play a critical rule for better understanding of abnormal blood flow which is believed to be the main reason for the disease [68, 37]. Davies et al. [37] has shown the effect of different flow patterns on the cell arrangement by exposing the cultured cells to different shear stresses caused by different flow patterns. As it can be seen in Fig. 1.2A, cells

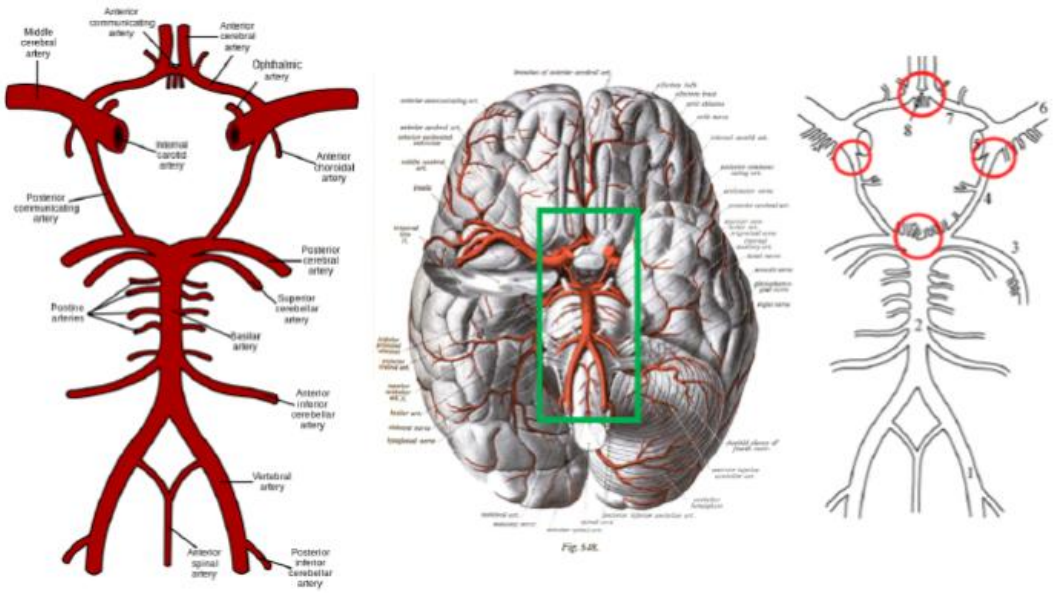

Figure 1.1: The most common locations for cerebral aneurysm, *left image* represents the Circle of Willis (COW), *middle image* shows the location of COW in the brain, and *right image* shows the most common areas of cerebral aneurysm. [69].

initially have a symmetric hexagonal shape when they are not expose to any flow. Next, cells were exposed to unidirectional flow for 24 hours which deformed them into ellipsoidal shape and aligned into the flow direction (Fig. 1.2B). After exposing the cells to a random flow pattern, cells also started to form random shapes and some cells even raised from the monolayer (Fig. 1.2C). They concluded, as long as cells were expose to unidirectional flow, they were able to handle high shear stress, however, as soon as the cells were exposed to random flow patterns, they were not able to handle shear stresses.

Near wall shear stresses can be used as an indicator of how fast flow patterns are changing near the wall. Mathematically, wall shear stress (WSS) can be calculated as a correlation of dynamic viscosity (μ), near wall velocity (v)and distance to the wall (y):

$$\mathbf{WSS} = \mu \frac{\partial \mathbf{v}}{\partial y} \tag{1.1}$$

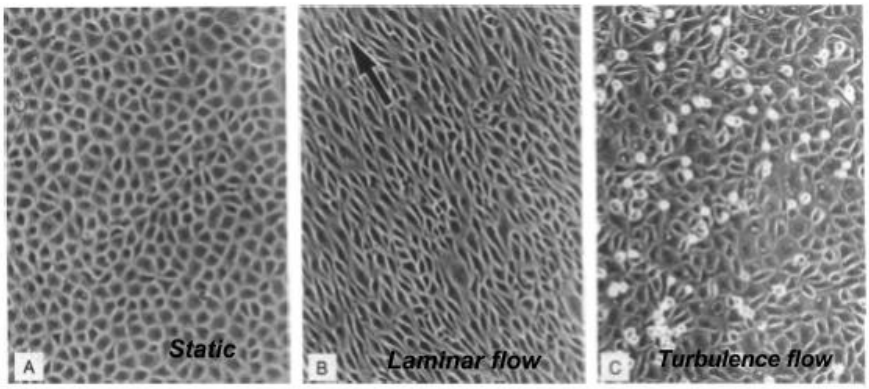

Figure 1.2: Cell configuration changes in a controlled environment due to the change of the flow from static (a), to laminar (b) and turbulence (c) [37].

having a good estimate of the blood flow near the wall can be used to accurately calculate the value of the WSS. Recently with further development of medical devices, imaging the blood flow became possible using the 4D flow MRI technique [85].

1.2 4D Flow Magnetic Resonance Imaging

4D Flow MRI refers to time-resolved three-dimensional (3D) spatial encoding combined with three-directional velocity-encoded phase contrast MRI. This method permits a detailed volumetric coverage as well as the study of blood flow dynamics in the vascular region of interest. These studies have been reported in the ventricles [133, 71, 12, 45, 123, 44, 137] and atria of the heart [52, 48, 3], aorta [132, 62, 63, 50, 20, 128], and carotid arteries [59, 86, 87, 121]. Unprocessed 4D Flow MRI data is plagued by several errors in addition to limited temporal ($\tilde{5}0\ \mu s$) and spatial resolution (1 - 1.5 mm isotropic). This limits the use of 4D Flow MRI in quantitative analysis of flow derived bio-markers such as WSS.

The physics of 4D flow is based on the measured phase change of spins moving through two opposing magnetic gradients applied in quick succession. The equation

that relates Larmor precision frequency of spins to the applied magnetic field and its gradient is given by

$$\omega_L(\mathbf{r}, t) = \gamma B_0 + \gamma \Delta B_0 + \gamma \mathbf{r}(t) \cdot \mathbf{G}(t) \tag{1.2}$$

where γ is the gyromagnetic ratio, B_0 is the static magnetic field, ΔB_0 is the local field inhomogeneity, $\vec{r}$ is the displacement and $\vec{G}(t)$ is the field gradient. Assuming that the fluid velocity $\vec{v}$ is constant during the acquisition time, the displacement vector is given by

$$\mathbf{r}(t) = \mathbf{r}_0 + \mathbf{v}(t - t_0) \tag{1.3}$$

where $\vec{r}_0$ is the displacement at time t_0. The phase is computed by integrating equation 1.2 from t_0 to the echo time (TE) as

$$\begin{aligned} \phi(\mathbf{r}, TE) &= \int_{t_0}^{TE} \omega_L = \phi_0 + \gamma \mathbf{r}_0 \cdot \int_{t_0}^{TE} \mathbf{G}(t) dt + \gamma \mathbf{v} \int_{t_0}^{TE} t \mathbf{G}(t) dt + \cdots \\ &= \phi_0 + \gamma \mathbf{r}_0 \cdot \mathbf{M}_0 + \gamma \mathbf{v} \cdot \mathbf{M}_1 + \cdots \end{aligned} \tag{1.4}$$

Here, ϕ_0 is the background phase offset due to field inhomogeneities. The second and third terms are due to the stationary and moving spins respectively. In the 4 point scan method, a reference scan along with 3 velocity encoding scans (added bipolar gradients along $x-$, $y-$, $z-$ directions) are used for each single raw data line in k-space. Subtracting the velocity scans from the reference gives the phase difference as

$$\Delta \phi = \gamma \mathbf{v} \Delta M_1 \tag{1.5}$$

The velocity-encoding parameter V_{enc} determines that maximum velocity that can be scanned. Its relationship to the difference in first gradient moment is given by

$$V_{enc} = \frac{\pi}{\gamma \Delta M_1} \tag{1.6}$$

Finally, the value of the encoded velocity is given by

$$v = V_{enc}\frac{\Delta\phi}{\pi} \tag{1.7}$$

1.3 Errors in 4D Flow MRI

Errors in 4D Flow MRI can broadly be divided into two categories, namely, time independent systematic errors and time dependent dynamic errors. Systematic errors add constant location dependent bias/shift to phase difference. Therefore they are also called phase shift errors. Dynamic errors on the other hand are both time and space varying. These include errors resulting from velocity aliasing and acquisition noise.

1.3.1 Phase shift errors

Phase shift errors are systematic phase errors of stationary as well as moving spins [79, 129]. Gradient field non-linearities [84], concomitant gradients (Maxwell terms) [10], and Eddy currents [129] are the main sources of phase shift errors in MR images.

Gradient field non-linearities are compensated by a matrix formulation that accounts for relative gradient field deviations from a theoretical model of local gradient field non-uniformity. This formulation modifies equation 1.7 to compensate for phase shift [84].

Concomitant gradients arise when the longitudinal gradient fields G_z are simultaneously activated with one of the transverse gradients (G_x, G_y). These non-linear terms are a consequence of Maxwell's equations (zero gradient and curl conditions) [93]. The issue of concomitant gradients are handled by altering the gradient design or by pulsing the main field. Other methods work on the reconstruction side [29, 31, 42] by modifying methods that have been developed for correcting gradient

field non-linearities [66, 107, 83, 92].

Eddy current correction

Background phase distortions result from inhomogeneities in the magnetic field and eddy current effects. These imperfections cause incorrect velocity measurements by adding random noise as well as random velocity values to each voxel. Since the introduction of an eddy current correction algorithm by Walker et al. [129], their proposed method been used as the gold standard in random noise and eddy current error correction for 2D and 4D flow MRI datasets. In this algorithm, the standard deviation (SD) of velocity (v_j) at each voxel (j) was calculated through time and if the SD was lower than a threshold it was considered as a static tissue. Then a plane was fitted on the static tissue on each image slice and subtracted from the dataset. This method can be accurate if the static tissue can be detected precisely. In order to improve the accuracy of static tissue detection, Ebbers et al. [43] proposed the use of higher order weighted least-square fit. The proposed weigh (w_j) at each voxel was calculated as:

$$w_j = \frac{m_j}{\left(SD_{v,j}\right)^p} \tag{1.8}$$

where p dictates the contribution of $SD_{v,j}$ to the weighting term and m_j represents the intensity of the voxel j in the magnitude image. We further improved the static tissue detection by adding a hard threshold filter on dot product of magnitude and velocity in each voxel.

The improvement between the raw 4D flow data compared to the data after eddy current correction is shown in Fig. 1.3. Fig 1.3 (a) shows the raw 4D flow MRI (raw 1 is slice view and raw 2 is particle tracing analysis in interior carotid artery (ICA)). Fig. 1.3 (b) shows correction with weighted least-square fit with a linear polynomial. Fig. 1.3 (c) shows the results for fitting quadratic polynomial. As the

second step, we zeroed down the remaining of value in the voxels selected as static tissue using a hard threshold (Fig. d-e) calculated as ten percent of max value of dot product of magnitude by velocity for each voxel.

1.3.2 Dynamic errors

Dynamic errors in 4D Flow MRI include signal dependent errors such as velocity aliasing (phase wrapping), , and random noise. We cover random noise in a separate section in detail.

Velocity aliasing/phase wrapping

Velocity aliasing occurs when the V_{enc} setting is lower than the maximum velocity. The V_{enc} parameter has to be set manually before the operator has any estimate of the maximum value of scan velocity. A velocity v with value equal to V_{enc} is mapped to phase difference $\Delta\phi = \pi$. If v is greater than V_{enc}, then the phase difference wraps around π and manifests as a negative velocity reading.

Xiang [134] developed an algorithm called temporal phase unwrapping (TPU) where the wrapped phase data was successfully unwrapped in time using only one-dimensional temporal integration. Cusack and Papadakis [35] developed a greedy algorithm to correct considering temporal and spatial information along with thresholding based on the estimated noise level in an iterative manner. Other methods have used assumptions of spatial and temporal continuity of the 4D Flow MRI signal [104, 114, 135, 125]. For example, the method by Loecher et al. [78], solves a constrained optimization problem based on the solution of the Laplacian of the phase, assuming phase continuity in three spatial and the temporal axes.

Another set of techniques uses multiple V_{enc} scans [106, 22]. The low V_{enc} scans have low noise but velocity aliasing. The high V_{enc} scans on the other hand will have no velocity aliasing but will have high noise. In a pre-processing step, the high V_{enc}

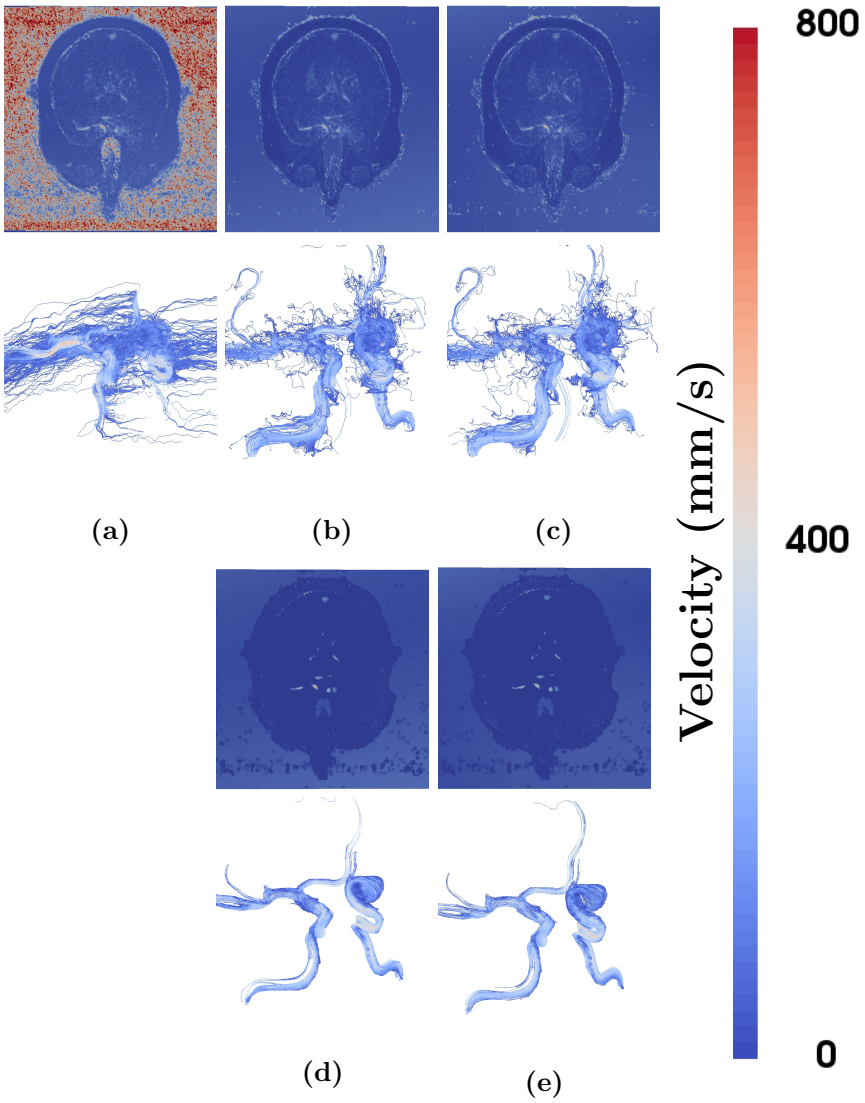

Figure 1.3: The effect of Eddy current correction on the particle tracing analysis. (a) shows an slice of raw 4D flow MRI as well as particle tracing analysis in the internal carotid arteries. (b) is after eddy current correction using first order polynomial fit. (c) shows the results after correction using a quadratic polynomial. Image (d) shows the results of applying hard thresholding on static tissue after first order polynomial fit. And (e) shows the result after hard thresholding of data after correction using quadratic polynomial fit.

scans are used to unwrap the low V_{enc} scans and simultaneously reduce noise.

1.4 Processing of 4D Flow MRI for Noise Reduction and Enhancement of Spatial Resolution

Random acquisition noise and spatial resolution are important factors that affect computation of flow dependent parameters such as wall shear stresses, viscous dissipation, and flow vorticity which require spatial derivative of the velocity field. Random noise in general is amplified by derivatives and low spatial resolution increases the discretization error. In case of certain intra-cranial aneurysms (where luminal diameters can frequently be $< 4mm$), at best, 4D Flow data will have about 4 voxels across the diameter in a typical setting ($1mm \times 1mm \times 1mm$ isotropic spatial resolution). Furthermore, noise can cause the velocity field to be rendered non divergence-free. Directly using this velocity field in analysis such as contrast injection simulation will become numerically unstable. Processing methods to handle noise and resolution issues can be broadly classified into three main categories: 1) Computational Fluid Dynamics (CFD)-independent methods, 2) patient-specific CFD models, and 3) Coupled 4D Flow MRI-CFD methods.

1.4.1 CFD-independent methods

CFD-independent methods, as the name suggests, do not involve computationally expensive patient specific CFD simulations in order to de-noise unprocessed 4D-Flow MRI. In addition to de-noising, these method try to impose mass conservation constraint on the data. The mass conservation constraint manifests as a divergence-free condition on the velocity field since blood in general is an incompressible fluid.

Regularization-based methods

One category of methods formulates the de-noising problem as a vector total variation regularization [13, 119, 118, 15, 58, 2] given by the equation:

$$\mathbf{f}^* = \underset{\mathbf{f}}{argmin}\ \mathcal{D}(\mathbf{f}; \mathbf{v}_M) + \sum_i w_i ||\mathcal{R}_i(f)||_p^p \tag{1.9}$$

Here $\mathcal{D}$ is data fidelity term (usually the Euclidean norm) that keeps the solution $\mathbf{f}$ close to the unprocessed 4D Flow data $\mathbf{v}_M$, $\mathcal{R}_i$ is the regularization function that imposes different flow physics constraints such as divergence-free and/or incompressibility [117, 2, 118] on the solution and w_i is the strength of regularization. Here $||.||_p$ is the vector (or tensor) l_p norm. Suter et al. [117], Arigovindan et al. [2], and Tafti et al. [118] only considered spatial regularization. Suter et al. and Arigovindan et al. have suggested the use of quadratic (L_2) regularization. However, Tafti et al. [118] showed that the discontinuities at the flow boundaries are better preserved by using l_1-norm regularization.

Bostan et al. [15] defined three different characteristics in continuous domain to apply to the measured flow field as:

$$\mathcal{R}_1(\mathbf{f}) = w_c \int_{\mathbb{R}} \int_{\mathbb{R}^3} |\nabla \times \mathbf{f}(\mathbf{x}, t)| d\mathbf{x} dt \tag{1.10}$$

$$\mathcal{R}_2(\mathbf{f}) = w_d \int_{\mathbb{R}} \int_{\mathbb{R}^3} |\nabla \cdot \mathbf{f}(\mathbf{x}, t)| d\mathbf{x} dt \tag{1.11}$$

$$\mathcal{R}_3(\mathbf{f}) = w_t \int_{\mathbb{R}} \int_{\mathbb{R}^3} |\partial_t \mathbf{f}(\mathbf{x}, t)|^2 \mathbf{x} dt \tag{1.12}$$

where eqs. 1.10 and 1.11 are used to penalize the total curl and divergence, and eq. 1.12 is defined based on smooth flow assumption for laminar flow. The

discretized optimization equation was given by

$$\mathcal{J}_\delta(\mathbf{f};\mathbf{y}) = \frac{1}{2}\|\mathbf{f}-\mathbf{y}\| + \mathcal{R}^s_\delta(\mathbf{f}) + \mathcal{R}^t_\delta(\mathbf{f}) \tag{1.13}$$

$\mathcal{R}^s_\delta(\mathbf{f}), \mathcal{R}^t_\delta(\mathbf{f})$ represented the spatial and temporal regularization terms given by

$$\mathcal{R}^s_\delta(\mathbf{f}) = \lambda_c \sum_{n\in\mathcal{N}} \mathrm{curl}_\delta(\mathbf{f}_n) + \lambda_d \sum_{n\in\mathcal{N}} \mathrm{div}_\delta(\mathbf{f}_n) \tag{1.14}$$

$$\mathcal{R}^t_\delta(\mathbf{f}) = \lambda_t \|\partial_{t,\delta}\vec{f}\|^2 \tag{1.15}$$

Equation 1.13 was solved in an iterative manner using an argument of separability of $\mathcal{R}^s_\delta$ using a novel method based on the Fletcher-Fenchel duality [14].

In another approach, Bostan et al. [13] used nuclear total variation (TVN) regularizer in order to solve Eq. 1.9. This regularizer can model the dependencies among the different components of the vector field more efficiently compared to the previous model. The Jacobian J generates the gradient of the vector field. The TVN method is formulated such that nuclear norm of the Jacobian evaluated at every spatial location of the flow. Therefore, the Eq. 1.9 can be re-written as:

$$\mathbf{f}^* = \underset{f}{argmin}\ \frac{1}{2}||\mathbf{v}_M - \mathbf{f}||_2^2 + w\sum_{j=1}^{k}||\mathbf{J}\mathbf{f}_j||_N \tag{1.16}$$

where $\sum_{j=1}^{k}||\mathbf{J}\mathbf{f}_j||_N$ is the discrete TVN that employs the l_1 norm and the discrete Jacobian ($\boldsymbol{J}$) of the vector field.

Projection-based methods

The second set of methods uses projection of the unprocessed noisy 4D Flow data into a divergence-free space to eliminate noise[113, 96, 94].

Song et al. [113] developed a method using finite differences to project 4D Flow

data onto the space of divergence-free fields (PSDF). Noise that is not divergence free was therefore eliminated. Using Helmotz representation of continuously differentiable vectors fields, the acquired data $\mathbf{v}_M$ was represented as

$$\mathbf{v}_M = \nabla p + \nabla \times \mathbf{q} \tag{1.17}$$

where p is a scalar field and $\mathbf{q}$ is a vector field. Taking divergence of equation 1.17,

$$\nabla \cdot \mathbf{v}_M = \nabla^2 p \text{ in } \Omega \tag{1.18}$$

where Ω is the flow domain. Equation 1.18 was solved for scalar field p with boundary condition

$$p = 0 \text{ on } \partial\Omega \tag{1.19}$$

where $\partial\Omega$ is the boundary of the flow domain Ω. Finally, the divergence free component of $\mathbf{v}_M$ was computed as

$$\mathbb{P}\mathbf{v}_M = \mathbf{v}_M - \nabla p \tag{1.20}$$

where $\mathbb{P}$ is the projection operator. Numerically, $\mathbf{P}$ was implemented as

$$\mathbb{P} = I - E^T(EE^T)^{-1}E \tag{1.21}$$

where E is the discretized divergence operator.

Busch et al. [21] developed an algorithm based on the combination of divergence-free radial basis functions (RBF) [80] and normalized convolution. The RBFs are divergence-free by definition, therefore, allow processing of three-dimensional velocity profiles while conserving the continuity equation. The velocity vector at location $\mathbf{r}$ is given as a vector weighted sum of matrix valued RBFs evaluated at distinct

locations $\mathbf{n}_j$

$$\mathbf{v}(\mathbf{r}) = \sum_{j=1}^{n} \mathbf{\Phi}\left(\mathbf{r} - \mathbf{r}_j\right) \mathbf{c}_j \tag{1.22}$$

The matrix of divergence-free RBFs can be written as:

$$\mathbf{\Phi}(r) = \left[(1 - \frac{|r|^2}{2\Upsilon^2})I + \frac{1}{2\Upsilon^2} r r^T\right] \exp(-\frac{|r|^2}{2\Upsilon^2}) \tag{1.23}$$

where I is the identity matrix and Υ determines the size of the support for the Gaussian function. The vector of coefficients is found using a least square fit to the acquired 4D Flow Data [111]. This process results in a system of equations given by

$$\begin{bmatrix} \mathbf{\Phi}(\mathbf{r}_1 - \mathbf{n}_1) & \cdots & \mathbf{\Phi}(\mathbf{r}_1 - \mathbf{n}_n) \\ \cdots & \cdots & \cdots \\ \mathbf{\Phi}(\mathbf{r}_n - \mathbf{n}_1) & \cdots & \mathbf{\Phi}(\mathbf{r}_n - \mathbf{n}_n) \end{bmatrix} \begin{bmatrix} \mathbf{c}_1 \\ \cdots \\ \mathbf{c}_M \end{bmatrix} = \begin{bmatrix} \mathbf{v}_1 \\ \cdots \\ \mathbf{v}_n \end{bmatrix} \tag{1.24}$$

Here the locations $\mathbf{r}_i$ where the divergence-free velocity field is reconstructed are the same locations $\mathbf{n}$ where 4D Flow Data is sampled.

Since both of the FDM and RBF methods impose strict divergence-free constraints on the flow field, they can suffer greatly from inaccuracies in the segmentation of the flow field. To remedy this, Ong et al. [96] developed a method combining divergence-free wavelets (DFWs) [94] with coefficient thresholding [39] and SureShrink [40] to enforce a softer divergence-free constraint on the flow field, reducing the sensitivity of the noise-reduction to segmentation errors. DFWs are vector-wavelets capable of separating flow data into divergence-free and non-divergence-free wavelet coefficients. Subsequently, the noise reduction is achieved by shrinking the two components' coefficients. Coefficient shrinkage is done by employing a soft-thresholding strategy. SureShrink aims to find optimal thresholds for coefficient shrinking as means to automate the process. The algorithm works based on mini-

mizing mean square error in the wavelet domain, given the level of noise. To estimate the noise level, at first, simple thresholding is applied to eliminate flow in regions of low image magnitude. The noise in the remaining flow regions can be approximated as additive Gaussian noise with standard deviation of V_{enc}/SNR [57]. Finally, to reduce the blocking artifacts of the DFWs, cycle spinning is used as discussed in [34].

Combined projection and regularization methods

An interesting approach by Ong et al. [95] and Santelli et al. [105] combines projection onto a divergence-free basis and optimization to simultaneously reconstruct and denoise k space 4D Flow Data. Given that the blood flow is incompressible, the phase of the signal, which is an alias to the velocity, is represented using a divergence-free wavelets basis. The magnitude signal is represented using a regular spatial wavelet basis. Since both magnitude and phase signals are sparse in their respective wavelet bases, a compressed sensing framework [121] using l_1 norm minimization is used to denoise the data and apply the divergence-free constraint. The optimization problem solved is given by

$$\min_{m\in\mathbb{R}_+,\phi\in\mathbb{R}} \frac{1}{2}\|Ame^{j\phi} - y\|_2^2 + \lambda_m\|\Psi_m m\|_1 + \lambda_\phi\|\Psi_\phi K_v\phi\|_1 \tag{1.25}$$

where m is the computed magnitude, ϕ is the phase, y is the raw 4D Flow Data in k space, K_v transforms phase to velocity, Ψ_m is the spatial wavelet for m and Ψ_ϕ is the divergence free wavelet for velocity. Soft thresholding is used to enforce approximate or "soft" divergence-free conditions. The method is made phase-wrap tolerant via phase cycle spinning.

1.4.2 Patient-specific CFD model

CFD-independent methods are fast and capable of significantly decreasing noise. However, none of these methods are capable of enhancing spatial resolution. CFD is an alternative to resolve the 4D flow MRI's spatio-temporal resolution problem. CFD has been used to predict blood flow patterns in different regions including but not limited to cerebral [102] and intracranial aneurysms [16, 116], the thoracic aorta [24] , and the carotid bifurcation [89, 72, 122]. Unlike 4D flow MRI, CFD simulations can be also used for post-operative flow simulations to ensure the best outcome of the operation [101]. The work flow of this group of methods can be divided into three steps: 1) patient-specific mesh generation, 2) boundary condition estimation, and 3) solving Navier-Stokes equations.

Mesh Generation

In order to numerically solve any partial differential equation, a discretized representation of the domain (i.e. mesh) is required. The input to mesh generation is the geometry of the object, in this case the blood vessels. Therefore, the first step in generating the computational mesh is the generation of blood vessel geometry from the MRI-scans through the process of segmentation.

The best source image to generate geometry is contrast-enhanced MR angiography (CE-MRA). However, this involves injection of a contrast agent that may not be suitable for all subjects. Time of flight (TOF-MRA) may be used when CE-MRA is not suitable. However, TOF-MRA has several sources of errors including in-plane saturation artifacts (when vessel in the plane of acquisition), shine-through artifacts (artifact of the maximum intensity projection (MIP) algorithm), flow-reversal artifacts (signal suppression due to retrograde flow), and susceptibility artifacts (caused due to magnetic field distortions near metal implants). The magnitude image from

4D Flow image may be used for generating the blood vessel geometry. However, it has typically very low resolution. There are ongoing efforts to merge several images (for example, TOF-MRA+Magnitude+MIP of 3 velocities) to eliminate various artifacts.

Once the blood vessel geometry is available from segmentation, mesh generation itself is not an issue as there are several commercial or free robust mesh generators. Furthermore, most commercial numerical solvers come with inbuilt mesh generators.

Boundary Conditions

Solving the time dependent flow physics typically requires imposition of initial and boundary conditions. Typically, in CFD modeling of blood flow, vessel walls are assume to be rigid (especially in case of blood vessels surrounded by tissue such as those in the brain or in the liver) with no-slip condition where the fluid touches the vessel wall. Next, the time varying inlet and outlet flow rates have to be specified. Inlet and outlet flow rates can be obtained from the 4D Flow data by placing planes normal to the blood vessel centerline at the inlets and outlets and integrating the velocity data over the area. To minimize the effect of noise, this analysis has to be done over multiple planes and the results averaged. Because of various factors (measurement errors, spatial resolution etc.) the computed inlet and outlet flow rates will not match thus violating the incompressibility constraint. Typically, either the inlet or the outlet flow rate is assumed to be true. The other flow rate is then divided in proportion to the measured flow rates from 4D Flow data in the different branches. CFD simulation packages such as ANSYS typically allow specifying such boundary conditions (for example, time varying inlet flow rate and time varying outlet flow proportions). Another issue is that the temporal resolution of 4D Flow is not sufficient to maintain numerical stability of the typical solvers. Therefore,

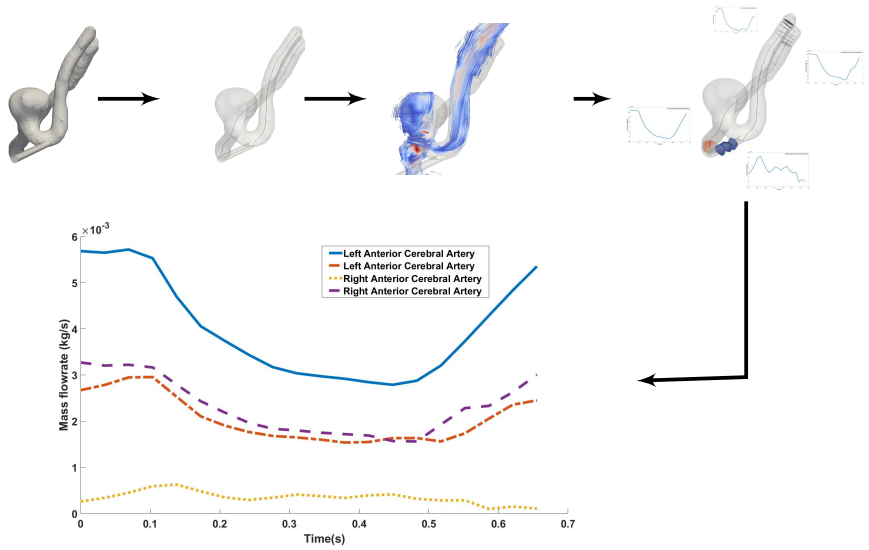

Figure 1.4: The process of calculating boundary conditions for a patient-specific model starts with the high-resolution co-registered surface file. The first step is to calculate the centerline of the geometry. Next, the 4D flow data is opened on top of the surface file and finally, for each inlet and outlet from the region of interest, we estimate the flow rate at up to five different planes.

either a FFT-based or polynomial-based interpolation with re-sampling is used to address this issue.

Some researchers have used lumped mass approximation using Windkessel model to model the dynamics of the downstream vasculature connected to region of interest to model outlet boundary conditions. Based on time varying terminal pressure data observed at a convenient downstream location, the outlet back-pressure is calculated based on RCR equivalent circuit.

Solving Navier-Stokes equations

The general Navier-Stokes equations for fluid motion can be written as [11]:

$$\rho\left(\frac{\partial \mathbf{v}}{\partial t} + \mathbf{v}.\nabla\mathbf{v}\right) = -\nabla\mathbf{p} - \nabla.\boldsymbol{\tau} + \mathbf{b} \tag{1.26}$$

where ρ is the fluid density, $\mathbf{v} = (u, v, w)$ represents the velocity vector in all three spatial directions, t stands for time, ∇ is the gradient operator, $\mathbf{p}$ is the pressure, $\boldsymbol{\tau}$ stands for the stress tensor, and $\mathbf{b}$ represents the body forces acting on the fluid. As mentioned, blood flow is usually assumed as incompressible Newtonian flow with constant viscosity μ and constant density ρ. The rigid body assumption omits $\mathbf{b}$, body forces. Therefore, the simplified equation will be:

$$\rho\left(\frac{\partial \mathbf{v}}{\partial t} + \mathbf{v}.\nabla\mathbf{v}\right) = -\nabla\mathbf{p} + \mu\Delta\mathbf{v} \tag{1.27}$$

where Δ is the Laplacian operator. Incompressible flow without source has to satisfy the continuity equation as well as Eq. 1.27, which can be formulated as [11]:

$$\nabla.\mathbf{v} = 0 \tag{1.28}$$

The momentum equation (Eq. 1.27) and continuity equation (Eq. 1.28) are non-linear and coupled and must be solved for unknown velocity field ($\mathbf{v} = (u, v, w)$) as well as pressure gradient ($\nabla\mathbf{p}$). In order to solve these equations, one of the well known semi-implicit or implicit CFD iterative algorithms such as; semi-implicit method for pressure linked equations (SIMPLE), semi-implicit method for pressure linked equations-consistent (SIMPLEC), semi-implicit method for pressure-linked equations revised (SIMPLER) or pressure implicit with splitting of operator (PISO), can be used [90]. Based on the user's desire for using finite volume (FV) or finite element (FE) method, one of the available solvers can be used to solve these equations such as ANSYS Fluent (ANSYS Inc., Canonsburg, PA) and OpenFOAM [131] which are using FV method or StarCCM+ which is uses FE method.

CFD method is capable of providing user-defined high spatio-temporal resolution. The accuracy of this approach critically depends on the assumptions made in the process of developing the model such as rigid walls and viscosity models (New-

tonian versus non-Newtonian fluid) as well as the accuracy of boundary conditions. However, it has been shown by different groups that this approach is usually in a good agreement with 4D flow MRI [136, 126, 102].

Different research groups have used this method and have reported different aspects of that. Rayz et al. [102] have shown the sensitivity of CFD to boundary conditions and reported good agreement between CFD and 4D flow MRI in a case of proper boundary measurement. Vali et al. [126] reported a CFD simulation model for post-operation flow patterns and quantitatively compared their results with *in-vivo* X-ray angiography. In this simulation, they have used Fourier analysis of the discrete flow measurements in order to estimate their inlet(s)/outlet(s) waveforms.

On the other side of the spectrum, there have been some efforts to validate patient-specific CFD simulations against in-vitro particle image velocimetry (PIV) in order to provide proofs for CFD to be an alternative to 4D flow MRI. Hoi et al. [60] reported a comparison between CFD and in-vitro PIV using artificial geometry. They have conducted research on the effect of geometry changes on the flow pattern. In this work they have reported a direct connection between the geometry details and flow patterns as well as significant effects of geometry mis-segmentation on hemodynamic parameter calculation. Ford et al. [49] also reported a good agreement between CFD and PIV measurements with patient-specific geometry. Raschi et al. [100] compared the results between CFD and *in-vitro* PIV for patient-specific geometries of growing cerebral aneurysm. They have reported good agreement between two methods in most areas except low velocity regions such as near the wall flow. Despite the reported differences, they have concluded that both methods can be used for patient-specific hemodynamic analysis.

1.4.3 Coupled 4D Flow MRI-CFD methods

Some of more recent techniques have attempted to combine 4D flow MRI and CFD to address limitations of both approaches, namely spatio-temporal resolution issues in 4D flow MRI and inaccuracy of assumptions (boundary conditions, and models used) in CFD. Unlike the pure CFD approaches where only the inflow and outflow waveforms are measured from 4D flow MRI for establishing boundary conditions, in the coupled 4D flow MRI-CFD approaches, the entire data in the region of interest is used to *correct* the CFD simulations.

This group of methods is based on the idea of prediction-correction algorithms. In other words, these methods are solving Navier-Stokes equation (Eq. 1.27) based on measured boundary conditions observed from 4D flow MRI data and try to minimize the error (correct the integration) between the integration and measurements at each reading using different methods.

De Hoon et al. [38] reported an algorithm where they coupled a simplified fluid solver "fluid implicit particle" (FLIP) [19], which was originally developed for computer graphics, with measured 4D flow MRI. In this model, they further simplified Eq. 1.27 by assuming inviscid blood flow to:

$$\frac{\partial \mathbf{v}}{\partial t} = -\mathbf{v}.\nabla\mathbf{v} - \frac{1}{\rho}\nabla\mathbf{p} \tag{1.29}$$

In their iterative algorithm, the simulation starts with initializing positions and velocities of FLIP particles using 4D flow MRI data. Then for each simulation time step, which is equal to the 4D flow MRI time steps, the algorithm minimizes the difference between the simulated velocity ($\mathbf{v}_{CFD}$) and 4D flow MRI measured data ($\mathbf{v}_M$) in multiple steps. Step one is to compute the velocity of each grid cell based on a weighted average of neighboring particle velocities and measured 4D flow

MRI data. Step two independently advects FLIP particles using simulated velocity and measured data using a second-order Runge-Kutta ODE solver. The velocity difference ($\mathbf{v}_{diff}$) is defined as the difference between estimated velocity and the measured 4D flow MRI velocity. Next by substituting the velocity difference into Eq. 1.29 the difference can be calculated as:

$$\frac{\partial \mathbf{v}_{diff}}{\partial t} = -\mathbf{v}_{CFD}.\nabla \mathbf{v}_{CFD} + \mathbf{v}_{M}.\nabla \mathbf{v}_{M} - \frac{1}{\rho}\nabla \mathbf{p} \tag{1.30}$$

Next step is to add the difference velocity calculated using eq. 1.30 to particle velocities and calculate the new velocity. The final step is to update the velocity as $\mathbf{v}_{CFD}^{new} \leftarrow \mathbf{v}_{CFD}^{n+1} - \mathbf{v}_{diff}^{n+1}$.

Furthermore, the reported algorithm runs in the 4D flow MRI resolution and has produced some preliminary results with a viscous fluid assumption.
1 In another approach, Koltukluoglu et al. [74] proposed an algorithm using Helmholtz-Hodge theorem. In this method, first, they up-sampled 4D flow MRI data into mesh resolution using linear interpolation. Since the up-sampled data does not obey the incompressible flow constraints, next the data was projected onto a divergence-free space using Helmholtz-Hodge decomposition. In their model, for regularity reasons, they have made a few assumptions such as the 4D flow MRI field ($\mathbf{v}_M$) is quadratically integrable, the domain of solution (Ω) is bounded, a simply-connected and Lipschitz subdomain of $\mathbb{R}^3$. Using mentioned assumptions and Helmholtz-Hodge theorem, the following space splitting holds:

$$(L^2(\Omega))^3 = \mathcal{H}_{div,0}(\Omega) \oplus \mathcal{H}_{curl,0}(\Omega) \oplus \mathcal{H}_{har}(\Omega) \tag{1.31}$$

where $\mathcal{H}_{div,0}(\Omega)$ and $\mathcal{H}_{curl,0}(\Omega)$ are the Sobolev space of square integrable vector fields with a square integrable divergence and a free-divergence, and a square integrable curl and a free-curl, respectively. The $\mathcal{H}_{har}$ is the space of harmonic scalar

functions $q \in \mathcal{H}^1(\Omega)$ having zero Laplacian. Using Eq. 1.31, the measured 4D flow MRI data ($\mathbf{U}_M$) can be written as:

$$\mathbf{v}_M = \hat{\mathbf{v}} + \mathbf{v}_\wedge + \mathbf{v}^* \tag{1.32}$$

where $\hat{\mathbf{v}} \in \mathcal{H}_{div,0}(\Omega)$, $\mathbf{v}_\wedge \in \mathcal{H}_{curl,0}(\Omega)$ and $\mathbf{v}^* \in \mathcal{H}_{har}(\Omega)$. Having upsampled divergence-free data they then calculated a CFD solutions using Windkessel model as boundary condition and then compared CFD with upsampled 4D flow MRI. In each iteration, calculated CFD velocities were used as initial values for a new simulation until the error between two datasets satisfied the convergence criteria.

Rispoli et al. [103] reported another algorithm using an edited version of SIMPLER algorithm in Cartesian grids where they added an extra step to the algorithm using Tikhonov regularization [108] to calculate a flow field that satisfies the physics of flow while being close enough to the measured 4D flow MRI data. In this implementation, they used a pseudo-transient solution with spatially-varying time steps in the algorithm [90]. The pseudo-transient solution in this case is to run CFD simulations between available 4D flow MRI measurements with constant boundary conditions for each simulation. In this method, using SIMPLER algorithm, first velocities are estimated using momentum equation (eq. 1.27) and constant boundary condition between available 4D flow MRI readings as:

$$\mathbf{\Pi}_{n-1}\mathbf{v}_n = \mathbf{b}_{n-1} \tag{1.33}$$

where $\mathbf{\Pi}_{n-1}$ is a $D \times D$ square hepta-diagonal matrix, where D is the number of mesh nodes, containing the previous iteration information of all three components of velocity as well as density and viscosity. The velocity vector, $\mathbf{v}_n$, is represent-

ing current time step velocity components to be calculated. The right hand sides vectors, $\mathbf{b}_{n-1}$, contains previous time step velocity information as well as current pressure gradient and the physical properties of the flow (density ρ, and viscosity μ).

For a given time step, convergence is achieved when the continuity equation (Eq. 1.28) is satisfied. In each iteration, velocity profiles, $\mathbf{v}_n$, as well as pressure gradients are updated till the convergence. Having the velocity profiles, Rispoli et al. [103] minimized the error between CFD and 4D flow MRI using the following equations:

$$F(\mathbf{v}_n) = \frac{1}{2}||\mathbf{\Pi}_{n-1}\mathbf{v}_n - \mathbf{b}_{n-1}||^2 + w||\mathbf{\Gamma}\mathbf{v}_n - \mathbf{v}_M||^2 \tag{1.34}$$

The first term in the right-hand side of Eq. 1.34 is essentially Eq. 1.33, the second term is the comparison between CFD results and 4D flow MRI measurements ($\mathbf{v}_M$). Coefficient w is adjustable scalars that determines the influence of 4D flow MRI on the final solution. $\mathbf{\Gamma}$ is a down-sampling matrix to relate CFD resolution into 4D flow MRI resolution, it can just as well be described as an averaging or blurring model. Having matrix $\mathbf{\Gamma}$, and using Eqs. 1.34, the velocities can be calculated as:

$$\mathbf{v}_n = \left(\mathbf{\Pi}_{n-1}^T\mathbf{\Pi}_{n-1} + w\mathbf{\Gamma}^T\mathbf{\Gamma}\right)^{-1}\left(\mathbf{\Pi}_{n-1}^T\mathbf{b}_{n-1} + w\mathbf{\Gamma}^T\mathbf{v}_M\right) \tag{1.35}$$

The updated velocity profiles used as initial conditions for the next iteration.

This thesis will focused on development of multiple post-processing algorithms for 4D flow MRI scans. We limit our focus to brain aneurysms due to the importance and limitations of MRI images for this disease due to their sizes. We will present

our algorithms (Ensemble Kalman Filter, Proper Orthogonal Decomposition-ridge regression, and Proper Orthogonal Decomposition-Dynamic Mode Decomposition), and will follow up with a case study on the effect of different reconstruction methods on the value and patterns of WSS.

Chapter 2

Post-processing 4D Flow MRI Using Ensemble Kalman Filter (EnKF)[1]

2.1 Introduction

Kalman Filter was initially introduced by Kalman [67] as a linear sequential filter, which means the model is integrated forward in time and whenever the measurements are available, these data are used to reinitialize the model before the integration continues.

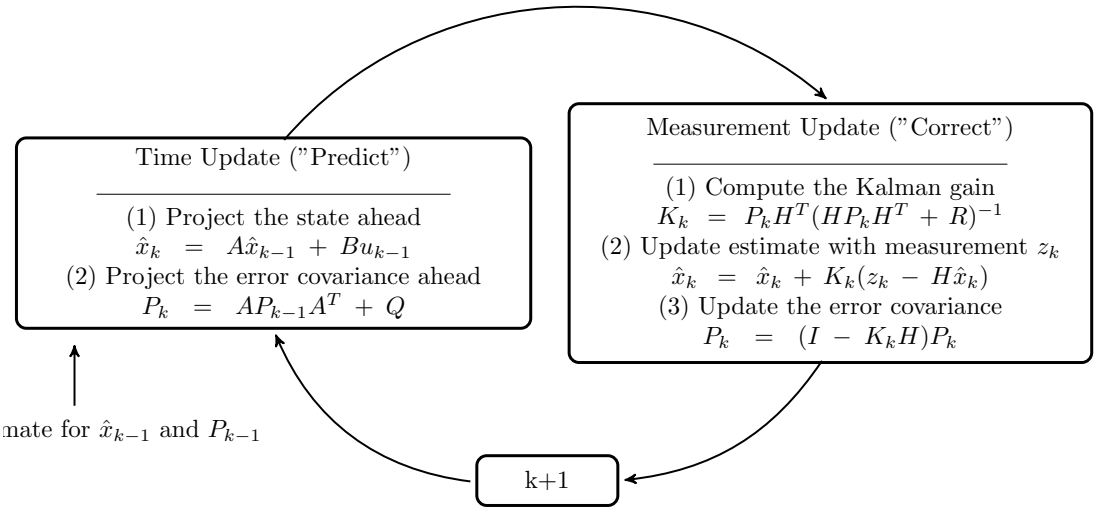

Figure 2.1: Kalman filter is a prediction/correction method. In the prediction step, model is integrated forward in time until point where measurements are available and integration reinitialize before the integration continues. [130]

Fig. 2.1 represents the Kalman filter algorithm as a prediction/correction method.

[1]This preliminary results were presented at:

[8] Bakhshinejad, A., Rayz, V., & DSouza, R. M. (2016). Reconstructing Blood Velocity Profiles from Noisy 4D-PCMR Data using Ensemble Kalman Filtering. In Biomedical Engineering Society (BMES) 2016 Annual Meeting. inproceedings.

At step one, the state of the system ($\hat{x}_k$) is predicted based on previous time step results ($\hat{x}_{k-1}$) and the boundary condition (u_{k-1}). The second step is calculation of the error covariance based on the error covariance of the previous time step ($\boldsymbol{P}_{k-1}$) as well as the process noise covariance ($\boldsymbol{Q}$). In the correction step, Kalman gain ($\boldsymbol{K}_k$) is calculated based on the error covariance and the measurement noise covariance ($\boldsymbol{R}$). The estimated state and error covariance is updated based on the calculated Kalman gain. The matrix $\boldsymbol{H}$ relates the state ($\hat{x}_k$) to the measurement (z_k).

As mentioned, the Kalman filter is formulated for linear systems. In order to deal with non-linear systems, an Extended Kalman Filter (EKF) was introduced. All steps of EKF are similar except for the error covarience calculation where $\boldsymbol{A}$ is the tangent linear operator (Jacobian) of the system. Due to calculation expense of the EKF, Ensemble Kalman Filter (EnKF) was proposed by Evensen [46].

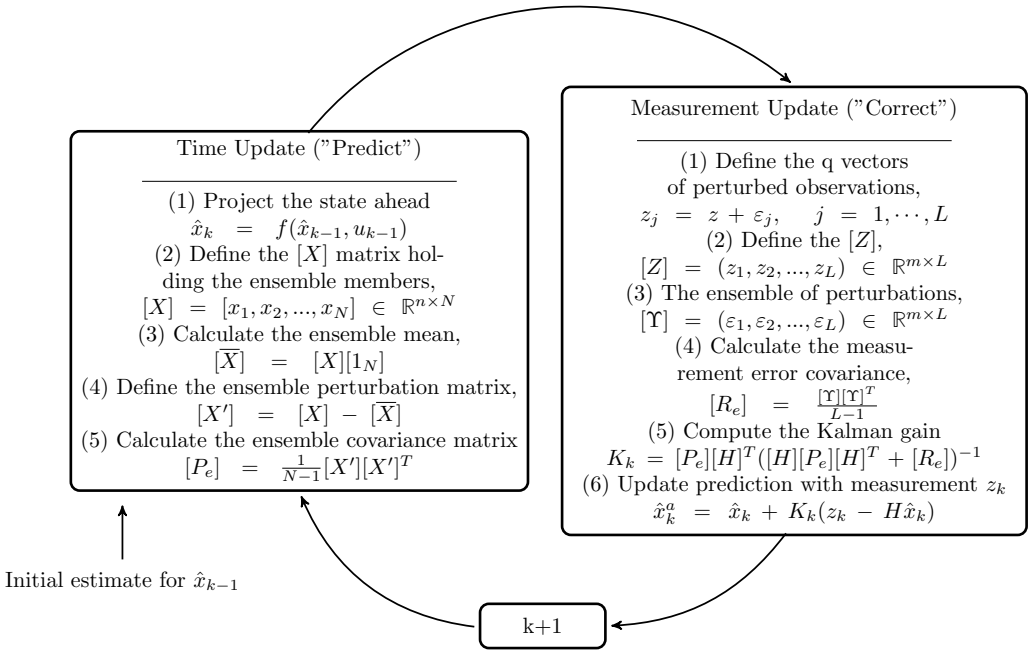

Figure 2.2: Ensemble Kalman filter (EnKF) is a prediction/correction method based on Kalman Filter. In the prediction step, the model is integrated forward in time until a point at which measurements are available, at which point the integration is reinitialized and continues forward.

Figure 2.2 shows the steps of EnKF as presented by Evensen [46]. As shown in

the figure, EnKF is a multi-step prediction/correction method based on KF. The prediction steps are as follow:

1. Predict each ensemble based on previous time step's state (x_{k-1}) and boundary condition as (u_{k-1}):

$$\hat{x}_k = f(x_{k-1}, u_{k-1}) \tag{2.1}$$

2. Define matrix $[X]$ holding all ensemble members as:

$$[X] = [x_1, x_2, \cdots, x_N] \quad \in \mathbb{R}^{n \times N} \tag{2.2}$$

where N is the number of ensemble members and n is the size of the model state vector.

3. The ensemble mean ($[\overline{X}]$) is:

$$[\overline{X}] = [X][1_N] \tag{2.3}$$

where $[1_N]$ is a $N \times N$ matrix with all elements equal to $1/N$.

4. Having the ensemble mean, ensemble perturbation can be calculated as:

$$[X'] = [X] - [\overline{X}] = [X]([I] - [1_N]) \tag{2.4}$$

5. The ensemble covariance matrix ($[P_e] \in \mathbb{R}^{n \times n}$) can be defined as:

$$[P_e] = \frac{[X']([X'])^T}{N-1} \tag{2.5}$$

With the ensemble covariance matrix ($[P_e]$), one can correct the predicted state ($\hat{x}_k$) using Kalman gain using the following steps:

1. For each measurement vector $z \in \mathbb{R}^m$, with m being the size of the measurement vector, one can define the L vectors of perturbed measurements as:

$$z_j = z + \varepsilon_j, \quad j = 1, \cdots, L \tag{2.6}$$

2. Define matrix $[Z]$, with each perturbed observation as a column as:

$$[Z] = [z_1, z_2, \cdots, z_L] \in \mathbb{R}^{m \times L} \tag{2.7}$$

3. The ensemble of perturbation is defined as

$$[\Upsilon] = [\varepsilon_1, \varepsilon_2, \cdots, \varepsilon_L] \in \mathbb{R}^{m \times L} \tag{2.8}$$

4. With having the ensemble of perturbation, the measurement error covariance matrix can be calculated as:

$$[R_e] = \frac{[\Upsilon][\Upsilon]^T}{L - 1} \tag{2.9}$$

5. Kalman gain can be calculated as:

$$K_k = [P_e][H]^T([H][P_e][H]^T + [R_e])^{-1} \tag{2.10}$$

6. And finally, the predicted state will be corrected using Kalman gain as:

$$[X]^a = [X] + K_k([Z] - [H][X]) \tag{2.11}$$

Adopting the EnKF method, we developed an algorithm in order to de-noise the 4D flow MRI data as well as increase the resolution to an arbitrary high resolution.

In this approach, we integrate the Navier-Stokes (NS) equations for an incompressible fluid (a valid assumption for blood flow in small vessels) until the points at which we have 4D flow MRI readings. At time steps where we have 4D flow data, the NS integration is re-initiated using EnKF method as described in details in the following section.

2.2 Method

The flowchart of our algorithm is shown in Fig. 2.3. We begin by constructing the boundary conditions (flow inlet) from the actual 4D flow MRI data. In this case, the inlet and outlet flow rate is estimated at several cutting planes at the inlet and outlet. Subsequently, the sample mean flow rates and the sample variance is computed. Based on these boundary conditions (BCs), a finite ensemble of BCs is generated using Gaussian sampling. This ensemble is used to compute an ensemble of simulations. The 4D flow MRI data are typically available only at intervals of 0.025 s. However, for the types of geometry in the study and discretization, this time interval results in large discretization errors as well as numerical instability for the explicit integrator. We therefore use a much smaller time step in the CFD integrator. We further use cubic interpolation on the BCs for intermediate time steps between 4D flow MRI data time steps. One of the ensemble solutions is used as ground truth. Simulated 4D flow MRI is generated by adding white noise to the solution. In the current study, we are assuming that we have 4D flow MRI values at each of the locations in the unstructured CFD mesh. In reality, 4D flow MRI is based on a regular grid with a sampling size that is much lower than the number of finite volume cells in the CFD mesh. This will be handled in a fully developed version of this paper.

The EnKF process estimates the best solution in three steps: prediction, comput-

ing prediction and observation covariance matrices, and analysis. In the prediction part, an ensemble of velocity vectors $\mathbf{x}^f$ is marched forward in time (k) by integrating the Navier-Stokes equation for incompressible fluids as a function of previous iteration's output and BCs as:

$$\mathbf{x}_k^{f_i} = \mathbf{f}\left(\mathbf{x}_{k-1}^{a_i}, \mathbf{u}_{k-1}^{i}\right) \tag{2.12}$$

where $\mathbf{u}$ is the BC. In each iteration 50 different ensemble predictions were calculated with perturbed initial conditions. Each one of these solutions was used as ensemble member $\mathbf{X}^{f_i} \in \mathbf{R}^n$

$$[A]^f = (\mathbf{x}^{f_1}, \mathbf{x}^{f_2}, \cdots, \mathbf{x}^{f_N}) \in R^{n \times N} \tag{2.13}$$

Where N is the number of ensemble members and n is the size of the model state vector. Then the sample ensemble perturbation matrix is calculated as:

$$\left[\hat{X}^f\right] = [A] - \overline{\left[A^f\right]} \tag{2.14}$$

where the matrix $\overline{\left[A^f\right]}$ has an ensemble mean as each column.

The ensemble covariance matrix $P_e \in R^{n \times n}$ is defined as:

$$[P]_e = \frac{\left[\hat{X}\right]\left[\hat{X}\right]^T}{N-1} \tag{2.15}$$

The vector of measurements $\mathbf{d} \in R^m$, where m is the number of observations, is given by:

$$[D] = \begin{bmatrix} \mathbf{d}_1 & \mathbf{d}_2 & \cdots & \mathbf{d}_N \end{bmatrix} \in R^{m \times N} \tag{2.16}$$

where $\mathbf{d}_j = \mathbf{d} + \varepsilon_j$, ε is the perturbation vector sampled based on observation noise

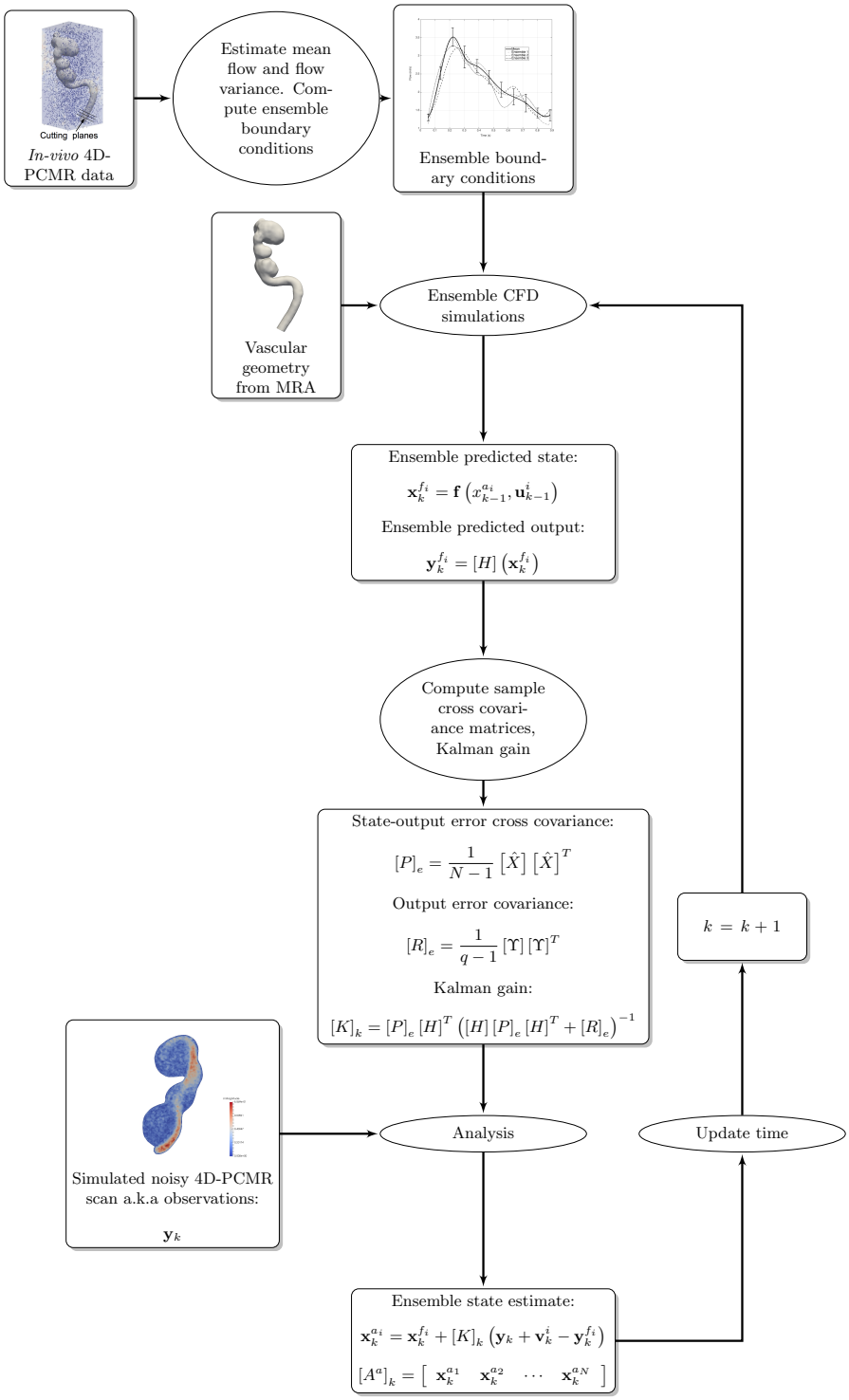

Figure 2.3: Flow-chart of the hemodynamic velocity reconstruction process using ensemble Kalman Filter (EnKF) algorithm.

characteristics. The matrix of perturbation is given as:

$$[\Upsilon] = \begin{bmatrix} \varepsilon_1 & \varepsilon_2 & \cdots & \varepsilon_N \end{bmatrix} \in R^{m \times N} \tag{2.17}$$

From here the measurement error covariance matrix was calculated as

$$[R]_e = \frac{[\Upsilon]\,[\Upsilon]^T}{N-1} \tag{2.18}$$

And finally the analysis matrix was calculated as:

$$[A^a]_k = \left[A^f\right]_k + [P]_e\,[H]^T \left([H]\,[P]_e\,[H]^T + [R]_e\right)^{-1} \left([D] - [H]\left[A^f\right]_k\right) \tag{2.19}$$

where $[A^a]_k = \begin{bmatrix} \mathbf{x}_k^{a_1} & \mathbf{x}_k^{a_2} & \cdots & \mathbf{x}_k^{a_N} \end{bmatrix}$ is ensemble Kalman filtered state estimate and $[H]$ is the observation matrix which is set to the identity matrix in this exercise since we are assuming that we have sensor readings at all CFD mesh nodes. The results from this point are used as initial condition for the next time step. We used the open source OpenFOAM CFD library for the patient-specific flow simulation. The open source Octave computing library was used to compute covariance and analysis matrices.

In equation 9, it is impossible to directly compute and store $\left([H]\,[P]_e\,[H]^T + [R]_e\right)^{-1}$ even for small number of observations (m=10000). We therefore use the QR approach [55]. Note that

$$[Z] = \begin{bmatrix} [U] & [V] \end{bmatrix} \begin{bmatrix} [U] \\ [V] \end{bmatrix} = \left([U]\,[U]^T + [V]\,[V]^T\right) \tag{2.20}$$

Assigning $[U] = [H]\left[\hat{X}\right], [V] = [\Gamma]$ we have

$$[Q][R] = \begin{bmatrix} [U] & [V] \end{bmatrix}$$

$$[Z] = [Q][R][R]^T[Q]^T$$

Computing $[Z]^{-1}\,\mathbf{v}$ is equivalent to solving $[Z]\,\mathbf{w} = v$. In other words

$$[Q][R][R]^T[Q]^T\,\mathbf{w} = \mathbf{v}$$

Clearly

$$\mathbf{w} = \left([Q]\left\{\left([R][R]^T\right)^{-1}\left\langle[Q]^T\,\mathbf{v}\right\rangle\right\}\right)$$

Here the brackets indicate the order of computation <> followed by {} followed by (). The matrix $([R][R]^T)^{-1} \in R^{2N\times 2N}$ is quite small and easy to compute and store.

2.3 Results

High-resolution contrast-enhanced magnetic resonance angiography (CE-MRA) images were used to construct patient-specific vascular geometry. The patient was imaged at the Vascular Imaging Research Center (VIRC), University of California, San Francisco (UCSF). The voxel size in the CE-MRA images was 0.7mm x 0.7mm x 0.7 mm and the contrast ratio of the luminal to background intensity was in the range of 8 to 10. MIMICS^{TM} (Mimics 17.0, Materialise Inc, Leuven, Belgium) was used to create a three-dimensional iso-surface corresponding to the luminal boundaries. A threshold intensity value was adjusted to ensure that the segmented iso-surface coincides with the luminal boundaries. The geometry obtained from the segmentation process included the aneurysm with its proximal and distal vessels.

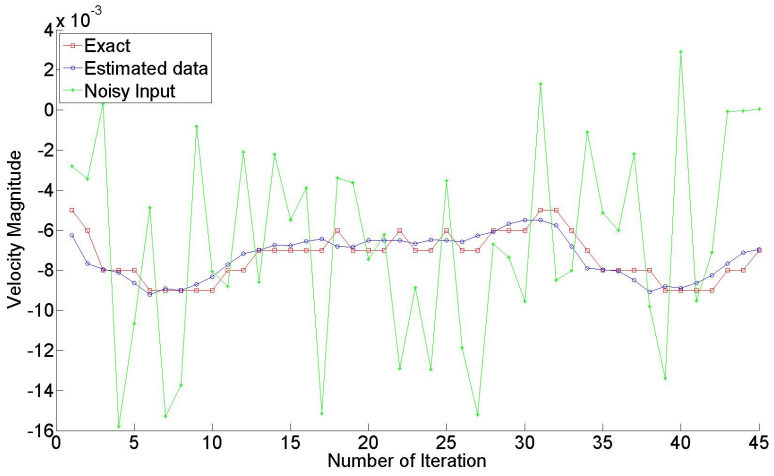

Figure 2.4: Comparison between noise-free CFD, noisy, and reconstructed/estimated velocity magnitudes at one randomly chosen node.

The iso-surface was then imported into a pre-processing software ANSYS ICEM CFD (ANSYS, Inc, Canonsburg, PA), where the computational domain and mesh were created. In order to obtain the flow waveform in the arteries, five 2D analysis planes were extracted from 4D flow MRI data for each proximal (inlet) and distal (outlet) vessel and the through-plane flowrate was calculated using Ensight (CEI, Apex, NC) for each plane. The sample mean flow μ_v^i and variance σ_v^i were then computed at different time steps. Gaussian noise with zero mean and variance of 10% of max velocity magnitude of the original CFD data was used to corrupt the CFD solution in order to simulate 4D flow MR data acquisition. We used an ensemble size of 50. The opensource CFD toolkit OpenFoam [131] was used for simulation. Kalman filter computation was conducted using opensource Octave. We were able to reconstruct the original data with less than 1% error. Figure 2.4 shows the comparison of velocity magnitude of the original CFD solution, the noisy data, and the reconstructed data at a randomly chosen location inside the aneurysmal artery.

Chapter 3

Post-processing 4D Flow MRI Using Proper Orthogonal Decomposition (POD)[1]

3.1 Introduction

Proper orthogonal decomposition (POD) is a data analysis method aimed to approximate high-dimensional data with extracting basis functions containing characteristics from the system of interest [28]. The POD is also known as Principle Component Analysis, the Karhunen-Loeve Decomposition, and the singular value decomposition.

In other words, the aim of POD is to approximate a function as a finite sum of variables in the form of

$$f = \sum_{i=1}^{M} \phi_i \hat{y}_i \tag{3.1}$$

where the approximation becomes exact when M approaches infinity. For that, let $\mathbb{X}$ be *Hilbert space* with inner product $< ., . >$ and norm $||.|| = \sqrt{< ., . >}$. Given a

[1]The results from this chapter was published in the Journal of Biomechanics. The preliminary results were also published in multiple conferences as following:

[6] Bakhshinejad, A., Baghaie, A., Vali, A., Saloner, D., Rayz, V. L., & DSouza, R. M. (2017). Merging computational fluid dynamics and 4D Flow MRI using proper orthogonal decomposition and ridge regression. Journal of Biomechanics, 58, 162173. https://doi.org/10.1016/j.jbiomech.2017.05.004

[41] DSouza, R. M., **Bakhshinejad, A.**, Baghaie, A., & Rayz, V. L. (2016). Reconstructing High Fidelity Hemodynamic Flow Fields by Merging Patient-Specific Computational Fluid Dynamics (CFD) and 4D Phase Contrast Magnetic Resonance Data. In ISMRM Workshop on Quantitative MR Flow. inproceedings.

[4] **Bakhshinejad, A.**, Baghaie, A., Rayz, V. L., & DSouza, R. M. (2016). A proper orthogonal decomposition approach towards merging CFD and 4D-PCMR flow data. In The 28th Society for Magnetic Resonance Angiography. inproceedings.

[5] **Bakhshinejad, A.**, Baghaie, A., Rayz, V. L., & DSouza, R. M. (2016). Towards Reconstructing Blood Velocity Profiles from Noisy and Sparse Time Resolved Phase Contrast Magnetic Resonance Flow Data. misc.

series of snapshots (y_i) in the $\mathbb{X}$ space we can define:

$$\mathtt{y} = span\{y_1, y_2, \cdots, y_n\} \subset \mathbb{X} \tag{3.2}$$

Having $\mathtt{y}$, POD generates a set of orthonormal basis of dimension k ($k \leq n$), which minimizes the error from approximating the snapshots as:

$$min_{\{\phi\}_{i=1}^{k}} \sum_{j=1}^{n} ||y_j - \hat{y}_j||^2, \quad s.t. < \phi_i, \phi_j >= \delta_{ij} = \begin{cases} 0 & i \neq j \\ 1 & i = j \end{cases} \tag{3.3}$$

where $\hat{y}_j(x) = \sum_{i=1}^{k} < y_j, \phi_i > \phi_i(X)$ is an approximation of y_i using $\{\phi\}_{i=1}^{k}$ and can be solved using singular value decomposition (SVD).

The POD was developed by several people and has been used in variety of applications. Low-dimensional description of turbulent fluid flows [61, 56, 9], structural vibrations [70, 77, 112], and damage detection [53, 76], to name a few applications in dynamic systems.

In this work, we adopted the POD method to generate a low-dimensional space of solutions using computational fluid dynamics (CFD) results as our snapshots. In this method with projecting noisy data on low-dimensional basis functions we were able to de-noise 4D flow MRI data as well as increase the resolution to an arbitrary high resolution.

3.2 Methods

The flowchart of our algorithm is shown in Fig. 3.1. We begin by constructing the boundary conditions (flow inlet and outlet) from the actual 4D flow MRI data. As shown in Fig. 3.1, the flow rate is estimated by placing cutting planes on the geometry at a number of locations at the inlet(s) and outlet(s) and computing the normal components of the velocities. We then average the values to reduce the ef-

fect of noise. The 4D flow MRI data is available only at intervals of 83.28 ms. This $\Delta t_{4DflowMRI}$ results in large errors in the discretization for CFD simulation as well as numerical instability. Therefore, the time interval used in our CFD simulation is $\Delta t_{CFD} = 0.02\Delta t_{4DflowMRI}$. The boundary condition (BC) is then interpolated using cubic splines in-between 4D flow MRI data points and sampled at the time increments of CFD. The sample BC variance is computed and an ensemble of BCs is computed. The actual BC is somewhere in-between these ensemble BCs. The ensemble BCs are used along with the vascular geometry to compute an ensemble of solutions. At each 4D flow MRI time step, the 3D velocity profile is called a snapshot. These snapshots are then used to compute the proper orthogonal decomposition.

3.2.1 Proper Orthogonal Decomposition (POD)

We generate our POD basis functions using the method of snapshots [110]. A matrix of solutions from the ensemble of solutions is organized as:

$$[Z_H] = \begin{bmatrix} [X_H^1] & [X_H^2] & .. & [X_H^k] & .. \end{bmatrix} \tag{3.4}$$

where $[X_H^k] \in \mathcal{R}^{N_H \times N_D}, k = 1 : N_Q$ is the sequence of velocity profiles by time of the k^{th} ensemble solution, N_H is the dimension of the 3-D velocity vector in CFD mesh resolution, N_D is the number of time steps in the input 4D flow MRI data, and N_Q is the number of ensemble solutions. Therefore, the total number of snapshots in $[Z_H]$ is given by $N_s = N_D \times N_Q$. Consequently, $[Z_H] \in \mathcal{R}^{N_H \times N_s}$. The solutions are also downsampled to the 4D flow MRI voxel grid using inverse distance weighting (IDW) [81] as:

$$[Z_L] = [S][Z_H] \tag{3.5}$$

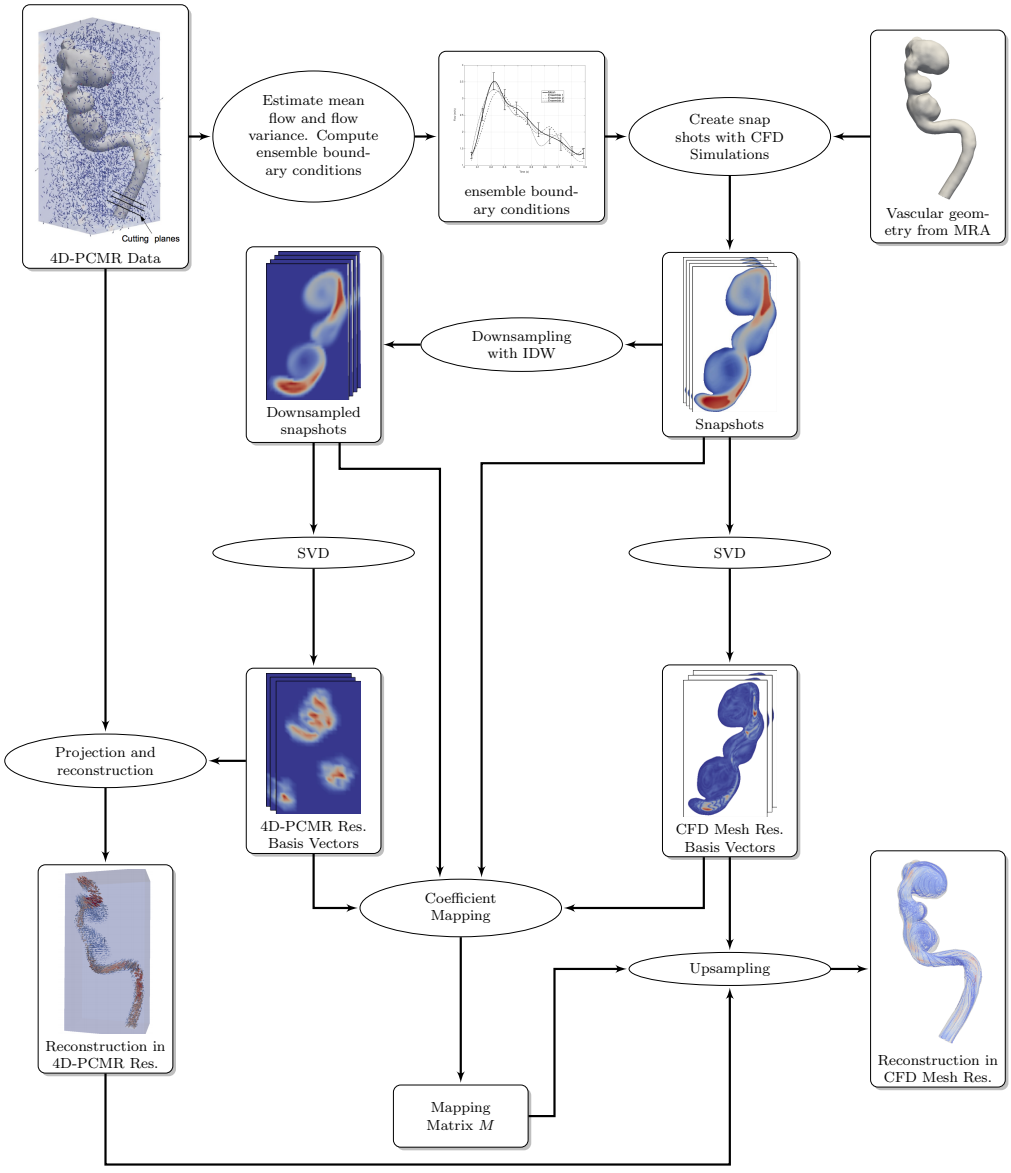

Figure 3.1: Flow-chart of the hemodynamic velocity reconstruction algorithm based on proper orthogonal decomposition (POD).

where $[S] \in \mathcal{R}^{N_L \times N_H}$ is the weighting matrix. IDW is commonly used to sample scattered data onto a regular grid, and N_L is the number of voxels in the 4D flow MRI data cube.

We next proceed to compute the singular value decomposition (SVD) [55] of the matrices $[Z_H], [Z_L]$ as:

$$\begin{aligned} [Z_H] &= [U_H]\,[\Sigma_H]\,[V_H]^T \\ [Z_L] &= [U_L]\,[\Sigma_L]\,[V_L]^T \end{aligned} \tag{3.6}$$

The matrices $[U_H] \in \mathcal{R}^{N_H \times N_s}, [U_L] \in \mathcal{R}^{N_L \times N_s}$ consists of left eigen vectors, the $[\Sigma] \in \mathcal{R}^{N_s \times N_s}$ is diagonal and contains the singular values and the matrices $[V_H], [V_L]$ contains the right eigen vectors. The matrices $[U_H], [U_L]$ form the basis that span the space of all possible solutions in the CFD mesh space and the downsampled 4D flow MRI voxel space respectively.

3.2.2 Noise Free Reconstruction at 4D flow MRI Resolution

The 4D flow MRI signal is the summation of the actual velocity and noise. While as the actual velocity signal obeys the flow physics, i.e., satisfies momentum and mass conservation equations, noise does not. Therefore, the actual velocity lies in the space of solutions spanned by the basis vectors $[U_L]$ and the noise signal is orthogonal to this space. Therefore, if we project the 4D flow MRI signal onto the basis vectors $[U_L]$, we should be able to recover the actual velocity. The projection is given by:

$$[\alpha_L] = [U_L]^T\,[Y_L] \tag{3.7}$$

where $[Y_L]$ is the 4D flow MRI raw data. Finally the estimate of the actual flow

in the 4D flow MRI voxel space is obtained as:

$$\left[\hat{Y}_L\right] = [U_L] \cdot [\alpha_L] \tag{3.8}$$

3.2.3 Noise Free Reconstruction at CFD Mesh Resolution Using Coefficient Mapping

4D flow MRI voxel space resolution is typically not enough to capture fine details of the flow field. On the other hand, CFD can resolve these details to an arbitrarily fine level (depending on the availability of computing power, random access memory (RAM) and time).Therefore, the problem here is to find if the low resolution flow estimate can be upsampled to the high resolution CFD mesh.

In our work, we used a coefficient mapping approach based on ridge regression to obtain the flow estimate. The estimate of flow velocity at the CFD mesh resolution is given by

$$\left[\hat{Y}_H\right] = [U_H]^T [\alpha_H] \tag{3.9}$$

To find $[\alpha_H]$, we use the relation

$$[\alpha_H] = [M] [\alpha_L] \tag{3.10}$$

where $[M] \in \mathcal{R}^{N_s \times N_s}$ is the mapping matrix. To obtain $[M]$ we use ridge regression that mimimizes an objective function given by

$$[M]^* = \arg\min_{[M]} \left\| \left[\alpha_H^i\right]_{i=1}^{N_Q} - [M] \left[\alpha_L^i\right]_{i=1}^{N_Q} \right\|_F^2 + \beta \|[M]\|_F^2 \tag{3.11}$$

where

$$\left[\alpha_H^i\right] = \left[U_H\right]^T \left[X_H^i\right]$$
$$\left[\alpha_L^i\right] = \left[U_L\right]^T \left[X_L^i\right] \tag{3.12}$$

The equations above compute the projections of the CFD mesh resolution ensemble solution snapshots and their respective downsampled 4D flow MRI resolution solution snapshots on the basis vectors. β is a regularization parameter which minimizes the effects of outliers in the data. *Basically, with ridge regression, we force the matrix* $[M]$ *to map known projection coefficients obtained from ensemble solutions in a least squared sense.* The optimal solution is given by

$$[M] = \left(\left[\alpha_H^i\right]_{i=1}^{N_Q} \right) \left(\left[\alpha_L^i\right]_{i=1}^{N_Q} \right)^T \times \left(\left(\left[\alpha_H^i\right]_{i=1}^{N_Q} \right) \left(\left[\alpha_L^i\right]_{i=1}^{N_Q} \right)^T + \beta.\mathbf{I} \right)^{-1} \tag{3.13}$$

where $\mathbf{I}$ is an identity matrix of size $N_s \times N_s$.

Empirically, we have observed that choice of parameter β can impact the quality of the upsampled solution we obtain. When β is small (10^{-2}), then upsampled data picks up certain amount of numerical oscillations. When β is large (100) it tends to smooth out sharp features. A method to optimally determine β automatically is a problem that we will research in the near future.

3.2.4 Down-sampling Using Inverse Distance Weighting (IDW)

Down-sampling is done to compute values of the field on a regular grid from an unstructured mesh. Using spatial binning, we assigned the mesh finite volume centers (mfvc) of the CFD mesh to voxels of the 4D flow MRI grid. The velocity at the center of every voxel was then computed as

$$\mathbf{v}_L = \frac{\sum_{i=1}^{N} w_i \mathbf{v}_H^i}{\sum_{i=1}^{N} w_i} \tag{3.14}$$

where $\mathbf{v}_L$ is the downsampled velocity vector, $\mathbf{v}_H^i$ in the velocity vector at the i^{th} mfvc assigned to the given voxel, N_p is the total number of mfvcs assigned to the given voxel using spatial binning. The weight is computed as

$$w_i = \exp\left(-\frac{\|p_c - p_i\|^2}{\gamma(\Delta x^2 + \Delta y^2 + \Delta z^2)}\right) \tag{3.15}$$

where p_c is the center of the voxel, p_i is the cell center of the i^{th} mfvc in the voxel, and $\Delta x, \Delta y, \Delta z$ are the x, y, z dimensions of the voxel. γ controls the level of blurring.

3.2.5 Creating Numerical Phantom

A numerical phantom was created to reflect actual data processing conditions. Patient-specific vascular geometry was used. Boundary conditions were derived from actual 4D flow MRI flow data.

Creating Patient Specific Vascular Geometry

High-resolution contrast enhanced MR angiography (CE-MRA) images were used to construct patient-specific vascular geometry. The patient was imaged at the Vascular Imaging Research Center (VIRC), University of California, San Francisco (UCSF). The voxel size in the CE-MRA images was 0.7mm x 0.7mm x 0.7 mm and the contrast ratio of the luminal to background intensity was in the range of 8 to 10. MIMICS^{TM} (Mimics 17.0, Materialise Inc, Leuven, Belgium) was used to create a three-dimensional iso-surface corresponding to the luminal boundaries. A threshold intensity value was adjusted to ensure that the segmented iso-surface coincides with the luminal boundaries. The geometry obtained from the segmentation

process included the aneurysm with its proximal and distal vessels. The iso-surface was then imported into a pre-processing software ANSYS ICEM CFD (ANSYS, Inc, Canonsburg, PA), where the computational domain and mesh were created. The computational mesh has roughly 1.8 Million finite volume cells.

Patient Specific Boundary Conditions

The patient-specific boundary conditions were obtained from *in-vivo* phase-contrast magnetic resonance (4D flow MRI). Three-dimensional velocity field during one cardiac cycle was extracted from 4D flow MRI data-set using an in-house software. In order to obtain flow waveform in the arteries, five 2D analysis planes were extracted from 4D flow MRI data for each proximal (inlet) and distal (outlet) vessel and the through-plane flowrate was calculated using Ensight (CEI, Apex, NC) for each plane. The sample mean flow μ_v^i and variance σ_v^i was then computed at different time steps.

A ensemble of 6 random sample flows using Gaussian distribution with the previously obtained mean flow and variance was computed at each time step. Since the temporal resolution of the 4D flow MRI was low for CFD simulation (typically 10-20 time-frames are collected during a cardiac cycle), piece-wise cubic interpolation was used to ensure minimal discretization error and numerical instability in the CFD simulation. The ensemble flows were then used as boundary conditions for the ensemble solutions of flow in the patient specific geometry.

CFD Simulation

The open source software OpenFoam [131] was used to compute the CFD solutions. We used the time varying pressure implicit with splitting of operator (PISO) to integrate the discretized Navier Stokes equation. Reynold's number calculated at the

inlet was estimated to be ≈ 400. At this value of Reynold's number, the flow can be assumed to be laminar [109]. Dynamic viscosity of blood was set to 3.5×10^{-3}Pa. Flow was assumed to be Newtonian with rigid aneurysm geometry. The time step for the for the PISO solver was set to 1.67ms. We are limited by the numerical stability of solver algorithm. An ensemble of 6 simulations was generated from the 6 random sample flows. One of the 6 ensemble solutions was randomly selected to be the ground truth. The remaining 5 solutions were used to compute the basis vectors as explained previously.

Simulated Noisy 4D Flow MRI data

To create the simulated noisy 4D flow MRI data, the ground truth solution in CFD mesh space was down-sampled to the 4D flow MRI grid. Then, the velocity data is transformed using five-point balanced encoding method proposed in [65]. This is followed by adding various levels of complex Gaussian noise (10% and 50 % of the maximum velocity magnitude) to the complex data. Finally, the inverse five-point balanced encoding transform was applied to obtain the noisy velocity fields [96].

3.2.6 Error Analysis

Error metrics used for comparison between our technique and finite difference method (FDM), divergence-free radial basis functions (RBF), divergence-free wavelets with SureShrink and median absolute deviation (MAD) with and without cycle spinning (DFW-sm, DFWsms) were the same as those in [96]. These include the velocity normalized root mean squared error (vNRMSE), the speed normalized root mean squared error (sNRMSE), and direction error (DE). For completeness, we include these herewith:

$$\text{Velocity NRMSE} = \frac{1}{\max_i |\mathbf{v}_{i,ph}|} \sqrt{\frac{1}{N} \sum_{i=1}^{N} |\mathbf{v}_{i,ph} - \mathbf{v}_{i,recon}|^2} \tag{3.16}$$

$$\text{Speed NRMSE} = \frac{1}{\max_i |\mathbf{v}_{i,ph}|} \sqrt{\frac{1}{N} \sum_{i=1}^{N} \left(|\mathbf{v}_{i,ph}| - |\mathbf{v}_{i,recon}|\right)^2} \tag{3.17}$$

$$\text{Direction Error} = \frac{1}{N} \sum_{i=0}^{N} \left(1 - \frac{|\mathbf{v}_{i,ph} \cdot \mathbf{v}_{i,recon}|}{|\mathbf{v}_{i,ph}||\mathbf{v}_{i,recon}|}\right) \tag{3.18}$$

$$\text{PVNR} = 20 \log_{10} \left(\frac{1}{\text{Velocity NRSME}}\right) \tag{3.19}$$

where N is the number of voxels within the segmented data, $\mathbf{v}_{i,ph}$ is the numerical phantom velocity in the i^{th} voxel of the segmented data and $\mathbf{v}_{i,recon}$ is the reconstructed velocity.

3.2.7 In-vivo 4D Flow MRI Data

4D flow MRI imaging was performed on an aneurysm patient using a 3T MRI scanner (Siemens, Skyra). The number of 4D flow MRI slices was 144 with in-plane matrix size of 194×144 pixels (voxel size of 1.25mm × 1.25mm × 1.33mm). The sequence parameters used for the MRI were as follows: TR/TE = 5.2/3.78 ms, flip angle = 8^o, and temporal resolution = 83.28 ms. The VENC was set to 100cm/s. 4D flow MRI data were imported in DICOM format to a pre-processing in-house software where the velocity data was extracted and saved for post-processing.

3.3 Results

3.3.1 Tests with Numerical Phantom

The methods developed in this work were compared to existing methods such as finite difference method (FDM), radial basis functions (RBF), and divergence free wavelets (DFW) using the numerical phantom described previously. The support of RBF basis functions was set to 7×7×7 experimentally. The number of iterations for the LSQR solver was set to be 20. The kernel size for FDM is 3x3x3 is fixed. The minimum size for the wavelet scaling subband was set to 10 for both DFW-sm (with automated selection of subband dependent threshold using SureShrink (SS) and median absolute deviation(MAD)) and DFW-sms (with SS, MAD, and partial cycle spinning). For DFW-sms, the number of spins was set to 4 which is equivalent to 16 random shifts[96]. As in the case of RBF, the parameters for DFW-sm, and DFW-sms were adjusted to achieve the best error performance for the dataset.

Fig. 3.2 illustrates the POD reconstruction results. Compared to the ground truth in Fig. 3.2(b), the de-noised velocity magnitude profile in 4D flow MRI resolution in Fig. 3.2(e) is clearly missing details in the high velocity regions as indicated by the arrows. These details are visible in the CFD mesh resolution reconstruction.

Next comparison tests were conducted with RBF, FDM, DFW-sm, and DFW-sms. Tests were run for two different noise levels (28.17dB PVNR corresponding to noise variance $\sigma = 10\%|\mathbf{v}_{max}|$ and 13.2dB PVNR corresponding to noise variance of $\sigma = 50\%|\mathbf{v}_{max}|$) at 4D flow MRI resolution of $40 \times 80 \times 80$. One additional test was run with noise level at 50% noise with the 4D flow MRI resolution at $21 \times 51 \times 25$. This is the resolution of the *in-vivo* patient data acquisition. Each of these tests were run 20 times and the sample means and variances of various error metrics were tabulated in Table 3.1.

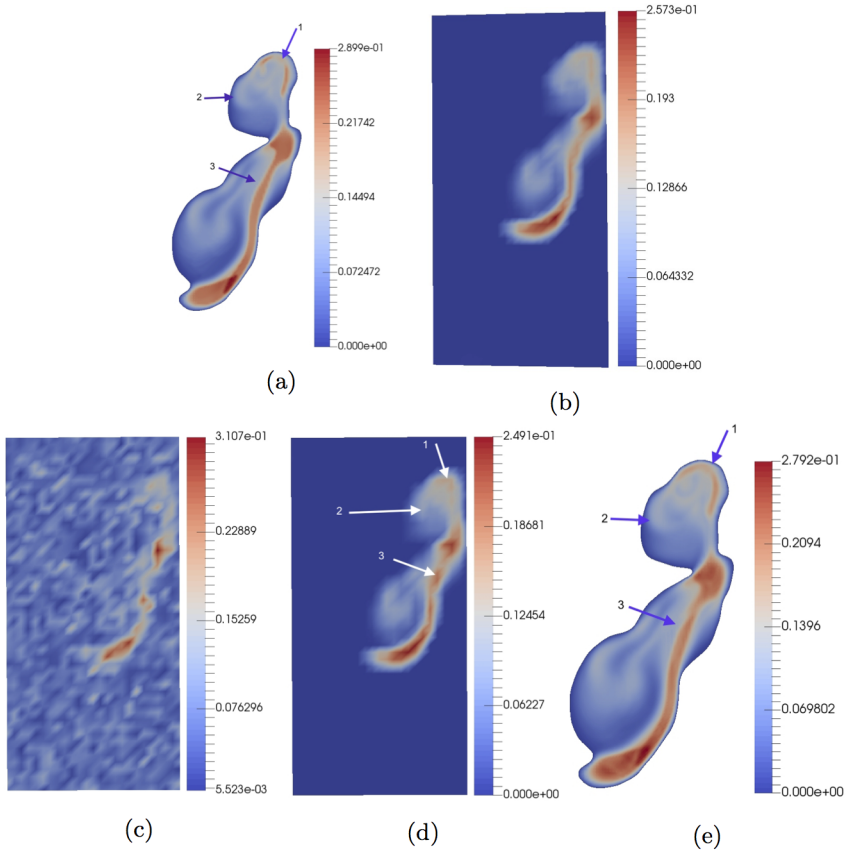

Figure 3.2: Reconstruction of velocity profile using POD. A random two dimensional cross-section was chosen for visualization purposes. Each sub-figure shows the velocity map of the selected cross-section in meter per second. (a) Original velocity profile (ground truth) sampled at a 2-D cross-section. (b) Down-sampled ground truth. (c) Simulated noisy 4D flow MRI. (d) De-noised velocity profile in 4D flow MRI resolution. (e) Reconstructed velocity profile in CFD mesh resolution. Notice that fine details missing in the reconstructed velocity profile in the 4D flow MRI resolution are revealed in the reconstructed velocity profile in CFD mesh resolution (see arrows pointing regions).

Table 3.1: Comparison metrics for segmented voxels with 10-50% noise level for $40 \times 80 \times 80$ resolution and 50% for $21 \times 51 \times 25$ resolution. These are sample mean and variance of 20 trials for each comparison are listed.

Resolution/Noise Level	Metrics/Method	Initial Noisy	FDM	RBF	DFW-sm	DFW-sms	POD
$40 \times 80 \times 80$	vNRMS	0.039100 ± 0.000112	0.064865 ± 0.000075	0.032695 ± 0.000083	0.036840 ± 0.000560	0.029270 ± 0.000393	**0.004590 ± 0.000055**
10%	sNRMS	0.022970 ± 0.000098	0.036590 ± 0.000107	0.022840 ± 0.000075	0.026980 ± 0.000605	0.023110 ± 0.000435	**0.003715 ± 0.000049**
	DE	0.057935 ± 0.000723	0.073955 ± 0.000793	0.038520 ± 0.000801	0.024470 ± 0.000511	0.012370 ± 0.000508	**0.000185 ± 0.000037**
	vNRMS	0.078755 ± 0.000221	0.085045 ± 0.000154	0.046730 ± 0.000184	0.058575 ± 0.001114	0.045880 ± 0.000620	**0.005915 ± 0.000169**
20%	sNRMS	0.047560 ± 0.000233	0.048730 ± 0.000117	0.030500 ± 0.000172	0.044085 ± 0.001375	0.037410 ± 0.000723	**0.004800 ± 0.000130**
	DE	0.117110 ± 0.000772	0.114755 ± 0.000832	0.066040 ± 0.000971	0.043105 ± 0.002119	0.021405 ± 0.000610	**0.000260 ± 0.000050**
	vNRMS	0.120120 ± 0.000401	0.112140 ± 0.000310	0.065615 ± 0.000322	0.075890 ± 0.000744	0.059255 ± 0.000774	**0.007715 ± 0.000272**
30%	sNRMS	0.074495 ± 0.000338	0.065800 ± 0.000367	0.041915 ± 0.000328	0.057570 ± 0.001213	0.049115 ± 0.000921	**0.006245 ± 0.000211**
	DE	0.171225 ± 0.001349	0.157620 ± 0.001162	0.095495 ± 0.001266	0.059875 ± 0.002764	0.029335 ± 0.001492	**0.000430 ± 0.000057**
	vNRMS	0.164840 ± 0.000596	0.144370 ± 0.000555	0.088170 ± 0.000359	0.091715 ± 0.001070	0.070835 ± 0.000624	**0.009965 ± 0.000365**
40%	sNRMS	0.105305 ± 0.000450	0.086980 ± 0.000350	0.056735 ± 0.000375	0.068920 ± 0.001000	0.059050 ± 0.000871	**0.008065 ± 0.000331**
	DE	0.218580 ± 0.001800	0.199195 ± 0.001220	0.125245 ± 0.001458	0.079265 ± 0.003582	0.037845 ± 0.001595	**0.000730 ± 0.000098**
	vNRMS	0.216380 ± 0.000888	0.183390 ± 0.000863	0.114670 ± 0.000728	0.108770 ± 0.002401	0.082435 ± 0.000775	**0.012835 ± 0.000660**
50%	sNRMS	0.142665 ± 0.000604	0.113515 ± 0.000704	0.074955 ± 0.000691	0.080960 ± 0.001491	0.068160 ± 0.001117	**0.010395 ± 0.000544**
	DE	0.259455 ± 0.001487	0.238690 ± 0.001684	0.156835 ± 0.001717	0.100970 ± 0.007125	0.049930 ± 0.002881	**0.001185 ± 0.000150**
$21 \times 51 \times 25$	vNRMS	0.217025 ± 0.002955	0.181650 ± 0.002163	0.129055 ± 0.002100	0.127545 ± 0.002768	0.092225 ± 0.001404	**0.032320 ± 0.001784**
50%	sNRMS	0.143245 ± 0.002402	0.112725 ± 0.001885	0.085240 ± 0.001918	0.085915 ± 0.001730	0.064945 ± 0.001425	**0.024830 ± 0.001300**
	DE	0.256875 ± 0.003177	0.234325 ± 0.003102	0.168690 ± 0.003423	0.146700 ± 0.008493	0.095905 ± 0.004848	**0.013465 ± 0.002194**

As can be seen from Fig. 3.3, at 10% noise level and 4D flow MRI resolution of $40 \times 80 \times 80$, for all methods, the visual quality is almost the same. The overall quantitative error metrics shown in Table 1 indicate that in order of performance, FDM performs the worst (it actually amplifies noise), DFW-sm is next, followed by RBF, DFW-sms, and POD. As can be seen, the second best technique DFW-sms has about 6.127×, 6.22×, and 66.86× the vNRMS, sNRMS, and DR error of POD. When the noise is increased to 50% (Fig. 3.4) with the same 4D flow MRI resolution, it can be seen that all methods including FDM reduce the error. However, the performance degrades with higher noise. The error metrics in Table 1 indicate that by order of performance, FDM performs the worst, RBF is next, followed by DFW-sm, DFW-sms, and POD. In this case, the second best method DFW-sms has about 6.42×, 6.55×, and 42.135× the vNRMS, sNRMS, and DR error of POD. Additionally, as indicated by the white arrows in Fig. 3.4, RBF, FDM, and DFW-sm have significant distortion in high velocity as well as low velocity details. DFW-sms distorts low velocity details. POD is able to reconstruct these velocity details much better (Fig. 3.4 (h)).

Fig. 3.5 illustrates the results of tests when noise was set to 50% with reduced 4D flow MRI resolution of $21 \times 51 \times 25$ (resolution of *in-vivo* data). As indicated, in regions indicated by arrows all previous reconstruction techniques have significant distortion in velocity patterns. POD reconstruction works much better as shown in Fig.3.5(e).

Fig. 3.6 illustrates the velocity magnitudes at 2 1-D cross sections as shown in Fig. 3.6(b). Results for 10% noise level indicate all previous methods work reasonably well (Fig. 3.6 (c),(d)). POD seems to have the least distortion. For the 50% noise level, DFW-sms and DFW-sm seem to have surprisingly large amount of

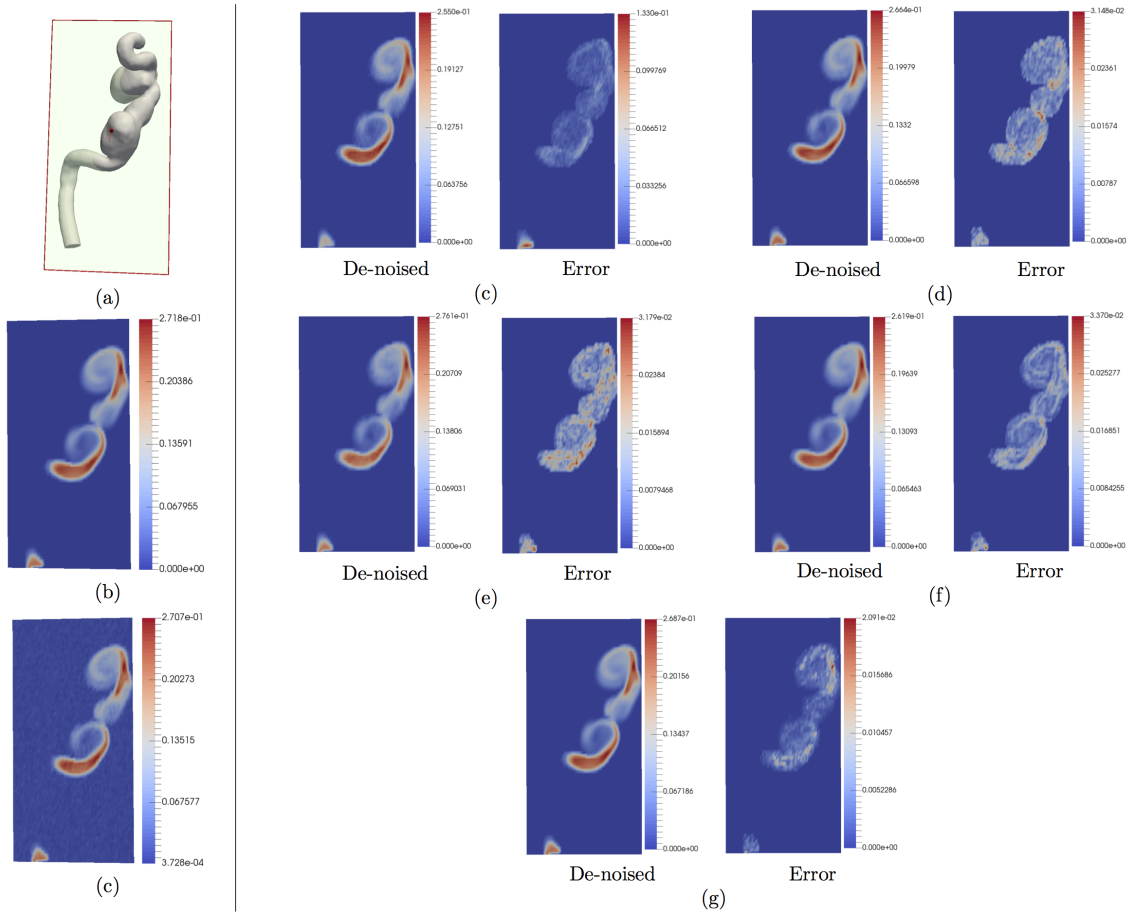

Figure 3.3: De-noising comparison on simulated data. In this test, the noise variance was set to be $\sigma = 10\%|\mathbf{V}_{max}|$. The 4D flow MRI resolution was set to $40 \times 80 \times 80$. (a)2-D section location for sampling velocity. (b) Down-sampled ground truth at the 2-D section. (c) Simulated noisy 4D flow MRI. (d) De-noising using FDM. (e) De-noising using RBF. (f) De-noising using DFM-sm. (g) De-noising using DFM-sms. (h) De-noising using POD. All methods visually appear to more or less preserve details in the velocity profile.

distortion as indicated in Fig.3.6(f). POD on the other hand is able to recover the velocity profile significantly better (Fig.3.6(g)).

3.3.2 Tests on *in vivo* Data

We also tested our algorithm on *in-vivo* data.(Fig. 3.7). In this case, the ground truth is not available. Fig. 3.7 (d), (e) show the results of our de-noising with reconstruction at CFD mesh resolution and streamlines respectively. We then compared

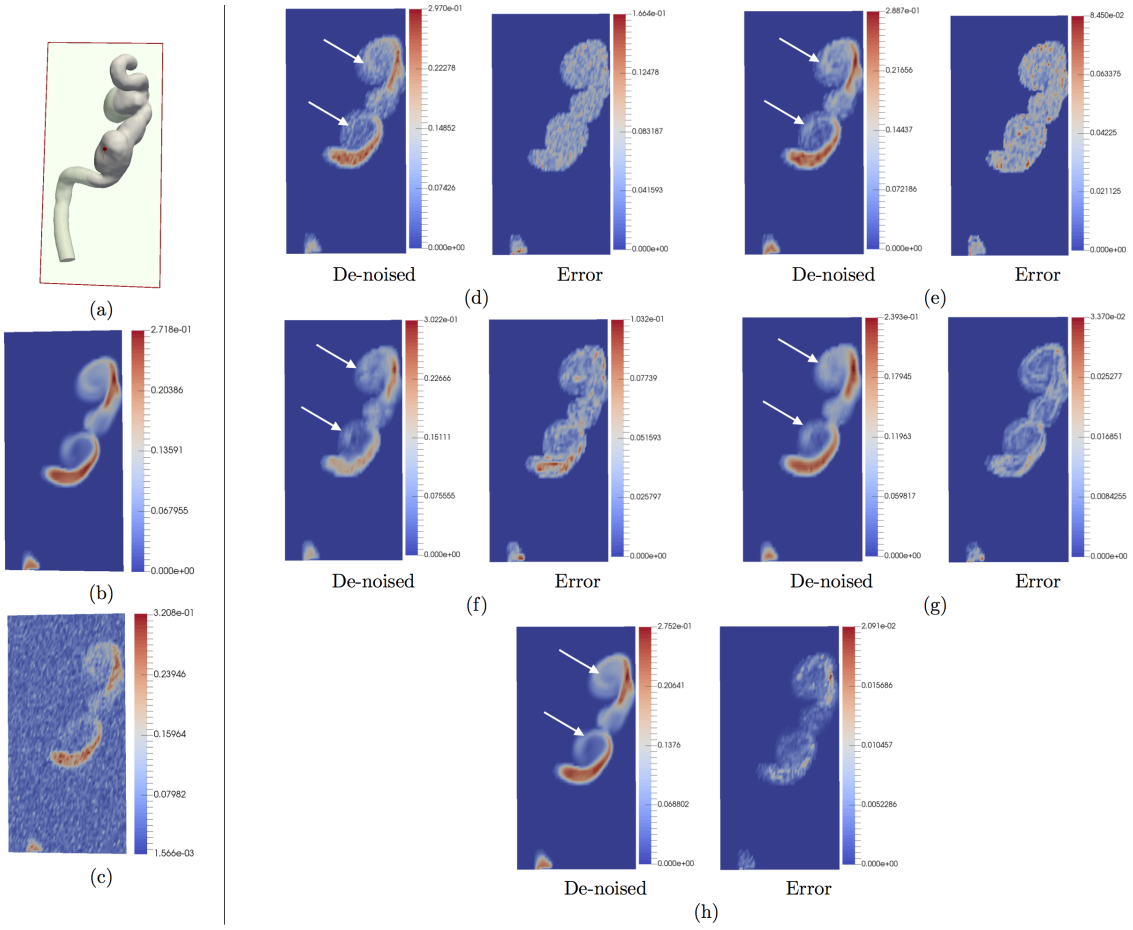

Figure 3.4: De-noising comparison on simulated data with high noise and high 4D flow MRI resolution. In this test, the noise variance was set to be $\sigma = 50\%|\mathbf{V}_{max}|$. The 4D flow MRI resolution was set to $40 \times 80 \times 80$. (a) 2D section at which velocity magnitudes were sampled. (b) Downsampled ground truth at this section. (c) Simulated noisy 4D flow MRI. (d) De-noising using FDM. (e) De-noising using RBF. (f) De-noising using DFW-sm. (g) De-noising using DFW-sms. (h) De-noising using POD. For FDM, RBF, DFM-sm, DFM-sms, white arrows indicate features that are distorted. In case of POD, these features are preserved quite well.

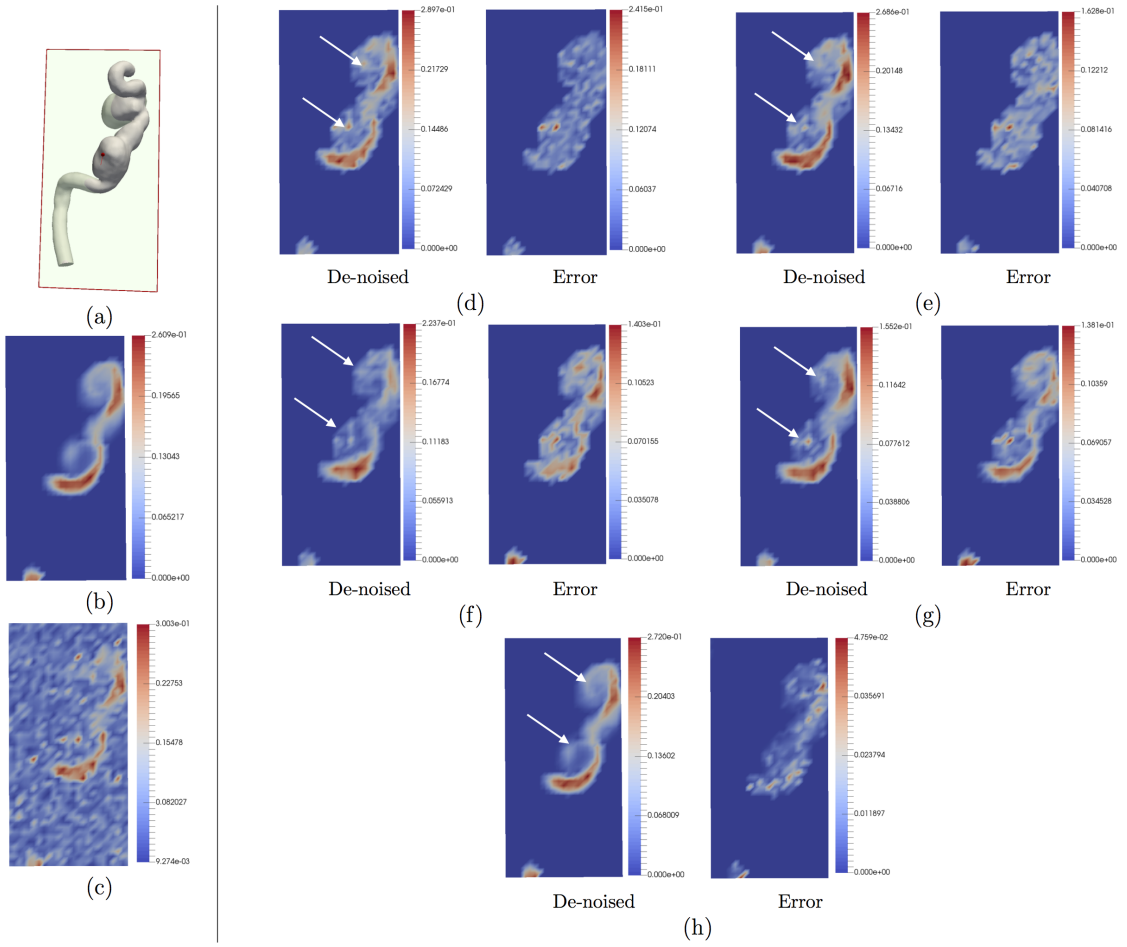

Figure 3.5: De-noising comparison on simulated data with high noise and low 4D flow MRI resolution. In this test, the noise variance was set to be $\sigma = 50\%|\mathbf{V}_{max}|$. The 4D flow MRI resolution was set to $21 \times 51 \times 25$ which is the same for *in-vivo* 4D flow MRI. (a) 2D section at which velocity magnitudes were sampled. (b) Downsampled ground truth. (c) Simulated noisy 4D flow MRI. (d) De-noising using FDM. (e) De-noising using RBF. (f) De-noising using DFW-sm. (g) Reconstruction using DFW-sms. (h) De-noising using POD. Clearly, as shown in the regions pointed to by the arrows, the POD method is able to preserve details in the flow much better than all other methods.

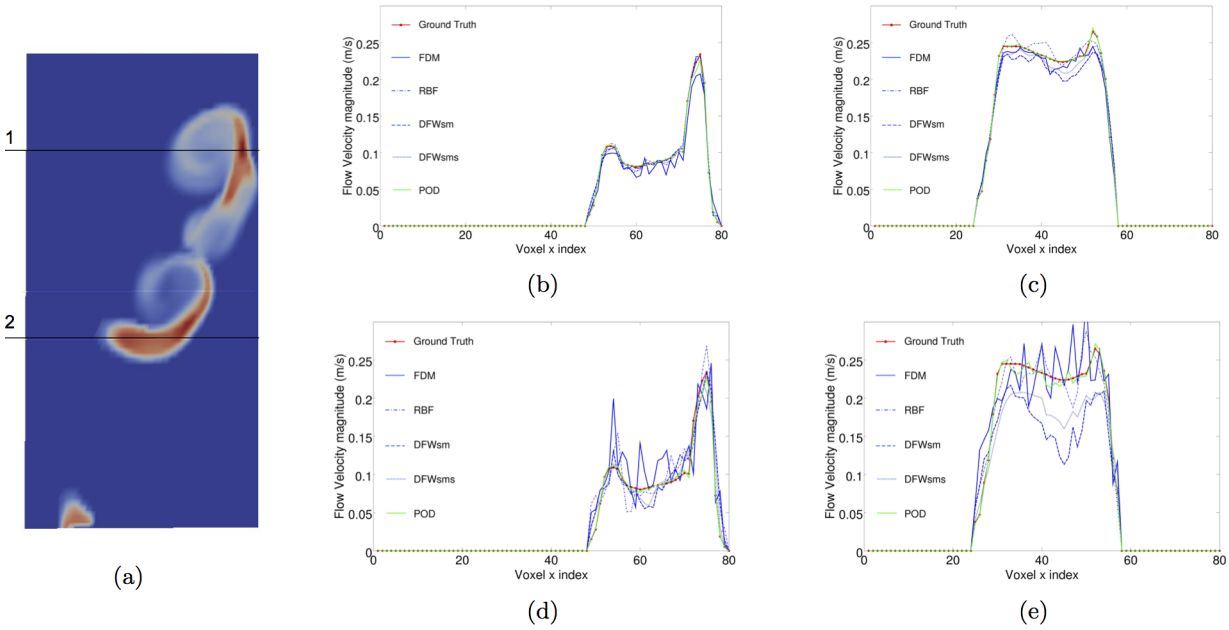

Figure 3.6: Comparison of velocity profiles along 1-D sections. In this test, the 4D flow MRI resolution was set to 40×80×80. (a) Location of sampled 1-D sections. (b), (c) Velocity profile comparison when noise variance was set to be $\sigma = 10\%|\mathbf{V}_{max}|$ at 1-D sections '1' and '2' respectively. (d),(e) Velocity profile comparison when noise variance was set to be $\sigma = 50\%|\mathbf{V}_{max}|$ at 1-D sections '1' and '2' respectively. Clearly, POD performs much better than all other methods. There is significant degradation in the results of other methods when noise level is increased.

our results against reconstruction using DFW (Fig. 3.8). As in [96], we performed streamline tests. Streamlines were constructed from the velocity data for the raw 4D flow MRI data, reconstruction with DFW, and reconstruction with POD in 4D flow MRI mesh resolution. We used the ParaView software to build streamlines from velocity data. Significant manual adjustment of parameters (threshold, sub band level etc.) with DFW had to be performed to generate results. DFM-sms failed to produce any coherent results. An emitter plane was place near the inlet and an analysis plane was placed near the outlet. Since this aneurysm has only one inlet and one outlet, it can be assumed that all streamlines released at the emitter should reach the analysis plane. In case of DFW, only 7.3 % of the streamlines reached the analysis plane. For POD-based de-noising in 4D flow MRI resolution, 87.8 % reached the analysis plane. For comparison, in case of the raw 4D flow MRI data, only 1% reached the analysis plane. Clearly, the POD approach greatly improves streamline lengths.

3.4 Discussions

A new method based on proper orthogonal decomposition for reconstructing high resolution hemodynamic velocity profiles from low resolution noisy time resolved phase contrast magnetic resonance was developed. Furthermore, a novel technique based on ridge regression was developed for up-sampling of the results from the 4D flow MRI voxel grid to the unstructured high resolution CFD mesh. The performance of the proposed techniques was tested against existing techniques such as FDM, RBF, and DFW using a numerical phantom. Since our techniques use actual CFD simulation to generate basis vectors, unlike most of the previous methods, our solutions conform to both the momentum balance as well as mass balance parts of the Navier-Stokes equation. The ability to up-sample means that our technique can be used to potentially recover minute flow details that are not visible at the

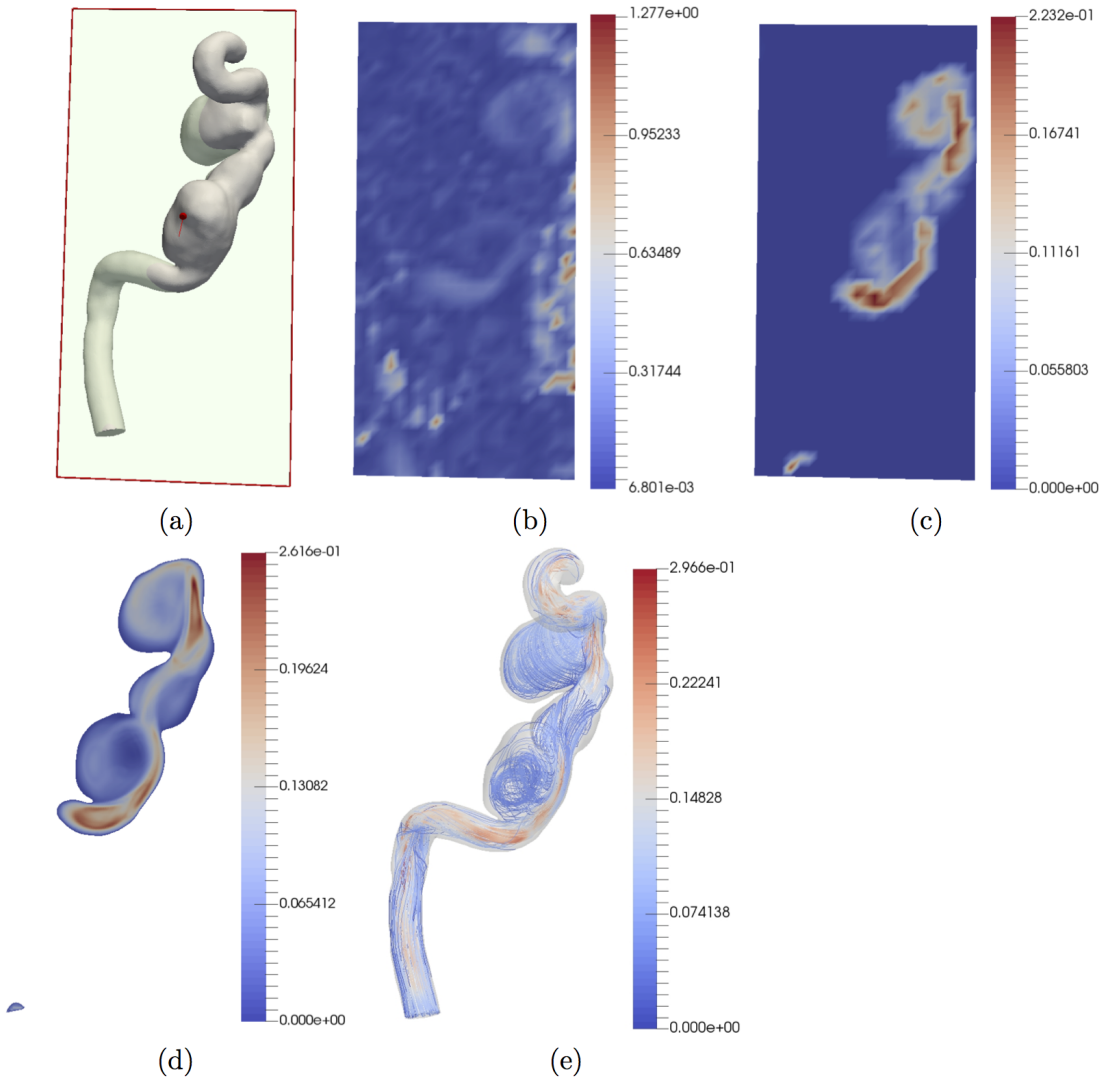

Figure 3.7: De-noising and reconstruction from *in-vivo* data. (a) 2-D section at which results are displayed. (b) Raw 4D flow MRI *in-vivo* data. (c) POD-based de-noising in 4D flow MRI resolution. (d) POD-based reconstruction using ridge regression in CFD mesh resolution. (e) Streamlines of CFD mesh resolution reconstruction.

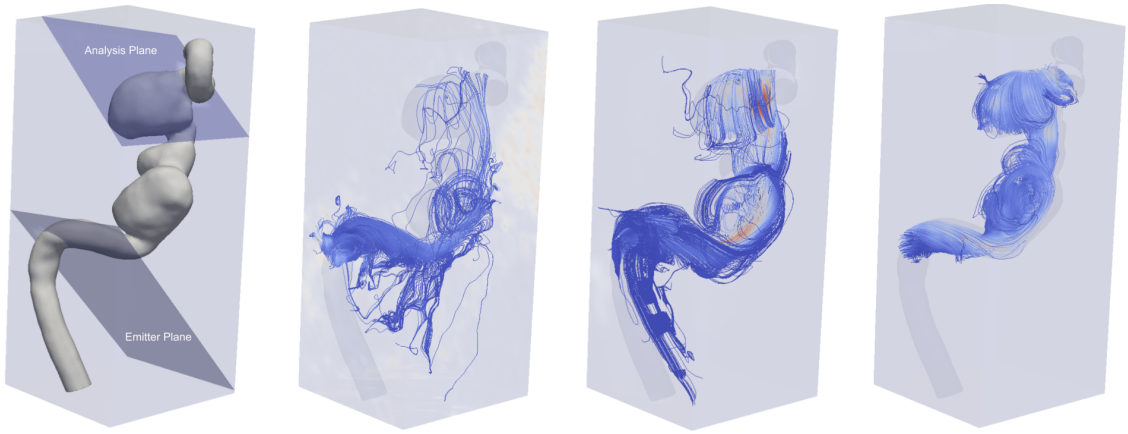

Figure 3.8: Comparison of de-noising on *in-vivo* 4D flow MRI data using streamlines. (a) Location of emitter and analysis planes. (b) *In-vivo* 4D flow MRI streamlines. (c) DFW streamlines (with manual optimization of parameters for the algorithm). (d) POD streamlines.

resolution of 4D flow MRI acquisition. Alternatively, our technique can be used in situations where size of the blood vessels in question limits the resolution of the 4D flow MRI acquisition.

In our work we have assumed laminar Newtonian flow model in the CFD simulation based on the Reynold's number. However, non-Newtonian flow models can easily be incorporated without any change in the basic process. Uncertainty in the viscosities and other parameters can be handled by process of sampling which will increase the number of CFD solutions used to generate the basis vectors.

Tuning of the parameters plays a significant role in the performance of the techniques used for de-noising of PCMR data. For the FDM, there are no parameters that need to be set since it works based on a Laplacian operator defined in a $3 \times 3 \times 3$ neighborhood around each voxel. On the other hand, for RBF, the radius (r) of radial basis kernels should be specified which results in a support size of $(2r+1) \times (2r+1) \times (2r+1)$. Moreover, the number of iterations for the LSQR solver

needs to be specified. For the divergence-free wavelet based techniques, DFW-sm and DFW-sms, the user should specify the minimum size for the wavelet scaling sub-bands. Additionally, the number of cycle spins should be determined for the DFW-sms. As for our algorithm, γ and β are the two parameters that need to be specified. γ controls the influence of neighboring points in the down-sampling step using the inverse distance weighting interpolation while β is the regularization parameter for computing the mapping between the basis vectors from the 4D flow MRI domain to the CFD mesh domain. It ensures optimal suppression of the possible outliers. In the current work, the values for the parameters are chosen experimentally based on the quantitative measures when comparing with the ground truth data (Fig. 3.9).

Currently, a major limitation of our technique is computational complexity. Several ensemble CFD simulations have to be executed to capture the space of solutions in the vicinity of the actual flow field. Our test case aneurysm had a single inlet and a single outlet. We empirically set the number of ensemble simulations to 6. In case of vasculature with multiple inputs and outputs, the number of simulation as well as the method to sample the simulation will become critical. A systematic method has to be developed to accomplish this in an optimal manner.

The most time consuming part of our technique is the process of executing the high fidelity finite volume CFD simulations with a mesh size of approximately 1.8 M nodes. Depending on the required details in the reconstructed flow field, one may be able to reduce the mesh size. Reducing the time for the simulations can be achieved by parallelizing the process of CFD simulations. The common practice involves using local or cloud-based computer grids. For our work, we utilized Google Cloud which reduced the computational time needed for high resolution simulations significantly. Earlier versions of the simulations on an AMD Phenom II X4 920

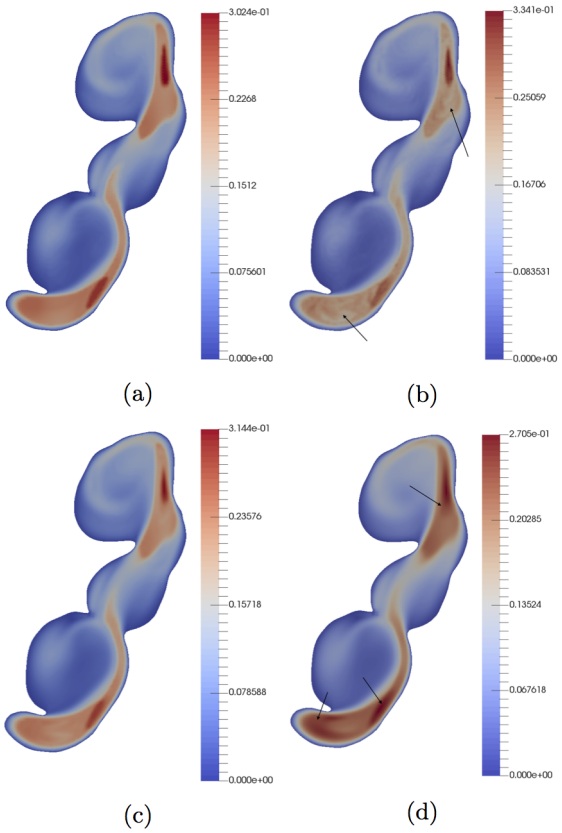

Figure 3.9: Effect of regularization parameter β in ridge regression based coefficient mapping on up-sampling. (a) Original velocity magnitude profile at a cross-section. (b) Velocity profile for $\beta = 0.01 \quad , PSNR = 29.3dB$ (c) Velocity profile for $\beta = 1 \quad , PSNR = 33.2dB$ (d) Velocity profile for $\beta = 100 \quad , PSNR = 29.7dB$. Large β tends to smooth out features especially in high velocity regions, while small β tends to pick up numerical disturbances in high velocity regions. The low velocity regions seem to remain unaffected.

Processor computer with 16 GB of RAM in Ubuntu 14.04 LTS environment in OpenFOAM 3.0 and without any multi-core modifications took around 10 hours per simulation. Using the current Google Cloud based platform, we reduced the time to around 1 hour for the six simulations, combined. Currently, we use an explicit time solver and are limited by the numerical stability of the integrator. We are in the process of investigating explicit integrators with relaxation which enable larger time steps. There is also the option of using fully implicit block coupled solver which may be even more efficient [36]. Another alternative is to integrate graphics processing unit (GPU) based solvers into our CFD simulation.

Chapter 4

4D Flow MRI Denoising and Spatial Resolution Enhancement: Application of Proper Orthogonal Decomposition Coupled with Dynamic Mode Decomposition[1]

4.1 Introduction

In the previous chapter we introduced a method for denoising and super-resolution of 4D Flow data using proper orthogonal decomposition (POD) [41, 6]. The basic method was implemented as a two step process: 1) projecting 4D Flow data on a set of POD basis vectors in the uniform grid of the volume, 2) up-sampling the projected data into a high resolution unstructured CFD mesh using ridge regression for coefficient mapping. The POD basis vectors are obtained from the snapshots of a CFD simulation with the boundary conditions obtained directly from the 4D Flow data. The ridge regression process required specification of optimization parameters which had significant effect on the accuracy of the solution. In this paper, we replace the ridge regression algorithm with a method based on dynamic model decomposition (DMD). The DMD method does not require parameter tuning and is completely autonomous.

[1]The results from this chapter was resulted in the following publications:

[47] Fathi, M. F., **Bakhshinejad, A.**, Baghaie, A., Saloner, D., Sacho, R. H., Rayz, V. L., & DSouza, R. M. (2018). Denoising and Spatial Resolution Enhancement of 4D Flow MRI Using Proper Orthogonal Decomposition and Lasso Regularization. Computerized Medical Imaging and Graphics.https://doi.org/10.1016/J.COMPMEDIMAG.2018.07.003

[1] **Bakhshinejad, Ali**, Fathi, M. F., Baghaie, A., Sacho, R. H., Nael, K., Saloner, D., DSouza, R. (2018). 4D Flow MRI Denoising and Spatial Resolution Enhancement: Application of Proper Orthogonal Decomposition Coupled with Dynamic Mode Decomposition. Under Review at the Journal of Biomechanics.

4.2 Methods

Figure 4.1 shows the developed algorithm. This algorithm is based on our previously published work using POD [6]. 4D Flow MRI data is sampled on the inlet and outlet boundaries at multiple cross-sectional planes normal to the centerlines to generate the boundary conditions. These boundary conditions are used to run a CFD simulation using geometry obtained from either contrast enhanced magnetic resonane angiography (CE-MRA) or time of flight (TOF)-MRA. Time resolved solution snapshots x_i of the CFD simulation are collected in a matrix $\mathbf{X}_H$

$$\mathbf{X}_H = \begin{bmatrix} x_1 & x_2 & \cdots & x_i & \cdots \end{bmatrix}$$

The snapshots are downsampled from the CFD mesh to the much coarser 4D Flow grid by averaging velocity values of finite volume centers (FVCs) that fall inside a grid voxel. This operation is formulated as a matrix operation as

$$\mathbf{X}_L = \mathbf{M}\mathbf{X}_H$$

Next the POD basis vectors at both 4D Flow resolution ($\mathbf{U}_L$) and CFD resolution ($\mathbf{U}_H$) are computed using singular value decomposition (SVD) of $\mathbf{X}_L$ and $\mathbf{X}_H$ respectively. The 4D Flow data $\mathbf{Y}$ is then projected on to the basis $\mathbf{X}_L$ as

$$\hat{\mathbf{C}}_L = \mathbf{U}_L^T \mathbf{Y}$$

The denoised flow field in the low resolution 4D Flow grid is then given by

$$\hat{\mathbf{Y}_L} = \mathbf{U}_L \hat{\mathbf{C}}_L$$

The projection coefficients in the high resolution are computed as

$$\hat{\mathbf{C}}_H = \mathbf{A}\hat{\mathbf{C}}_L$$

where $\mathbf{A}$ is the coffiecient mapping matrix. Finally, the flow field in the high resolution of the CFD mesh is given by

$$\hat{\mathbf{Y}}_H = \hat{\mathbf{C}}_H\mathbf{U}_H$$

Previously, the coefficient mapping matrix $\mathbf{A}$ was found using a process of ridge regression. In this paper, we describe a new method using techniques from DMD.

4.2.1 Mapping projection coefficients using DMD

We use the snapshots of the CFD simulation x_i to *learn* the coefficient projected matrix $\mathbf{A}$. In high resolution, the projection coefficients of the snapshots are given by

$$\mathbf{C}_H = \mathbf{U}_H^T\mathbf{X}_H$$

Similarly, in low resolution

$$\mathbf{C}_L = \mathbf{U}_L^T\mathbf{X}_L$$

We now compute matrix $\mathbf{A}$ such that

$$\mathbf{C}_H = \mathbf{A}\mathbf{C}_L$$

We use the DMD algorithm illustrated in Algorithm 1 to compute the matrix $\mathbf{A}$. Rather than using all available dynamic modes, we only pick an optimal number of modes (r in line 2 of Algorithm 1) using the method of singular value hard thresholding (SVHT) to compute $\mathbf{A}$ [54]. The SVHT prevents over-fitting which

can result in spurious artifacts. The matrix $\mathbf{A}$ is then given by

$$\mathbf{A} = \mathbf{\Phi}\mathbf{\Lambda}\mathbf{\Phi}^{\dagger}$$

where $\mathbf{\Phi}^{\dagger}$ is the pseudo-inverse of $\mathbf{\Phi}$

Algorithm 1: The overall procedure of DMD algorithm

Data: The low and high resolution coefficients matrices $\mathbf{C}_L$ and $\mathbf{C}_H$, the number of modes to pick r

Result: The matrix of DMD modes $\mathbf{\Phi}$, the vector of corresponding eigenvalues $\boldsymbol{\lambda}$

1 Find the SVD of $\mathbf{C}_L$ such that $\mathbf{C}_L = \mathbf{U}\mathbf{\Sigma}\mathbf{V}^*$;

2 Truncate $\mathbf{U}$ to the first r columns;

3 Truncate $\mathbf{\Sigma}$ to the upper-left $r \times r$ matrix;

4 Truncate $\mathbf{V}^*$ to the first r rows;

5 Define $\tilde{\mathbf{A}} \triangleq \mathbf{U}^*\mathbf{C}_H\mathbf{V}\mathbf{\Sigma}^{-1}$;

6 Find the eigenvalues $\boldsymbol{\lambda}$ and eigenvectors $\mathbf{W}$ of $\tilde{\mathbf{A}}$, i.e. $\tilde{\mathbf{A}}\mathbf{W} = \mathbf{W}\,\mathrm{diag}(\boldsymbol{\lambda})$;

7 Compute the DMD modes $\mathbf{\Phi} \triangleq \mathbf{C}_H\mathbf{V}\mathbf{\Sigma}^{-1}\mathbf{W}$;

8 **return** $\boldsymbol{\lambda}$, $\mathbf{\Phi}$

4.3 Results

4.3.1 Benchmarking tests using numerical phantoms

The numerical phantom was generated by running a reference CFD simulation using realistic boundary conditions and actual patient geometry obtained from MRA scans. The reference CFD simulation was down-sampled to the 4D-Flow MRI grid and noise added in complex k-space as in [96]. We used velocity-normalized root mean square error (vNRMSE), speed-normalized root mean square error (sNRMSE), and direction error (DE) to quantify errors.

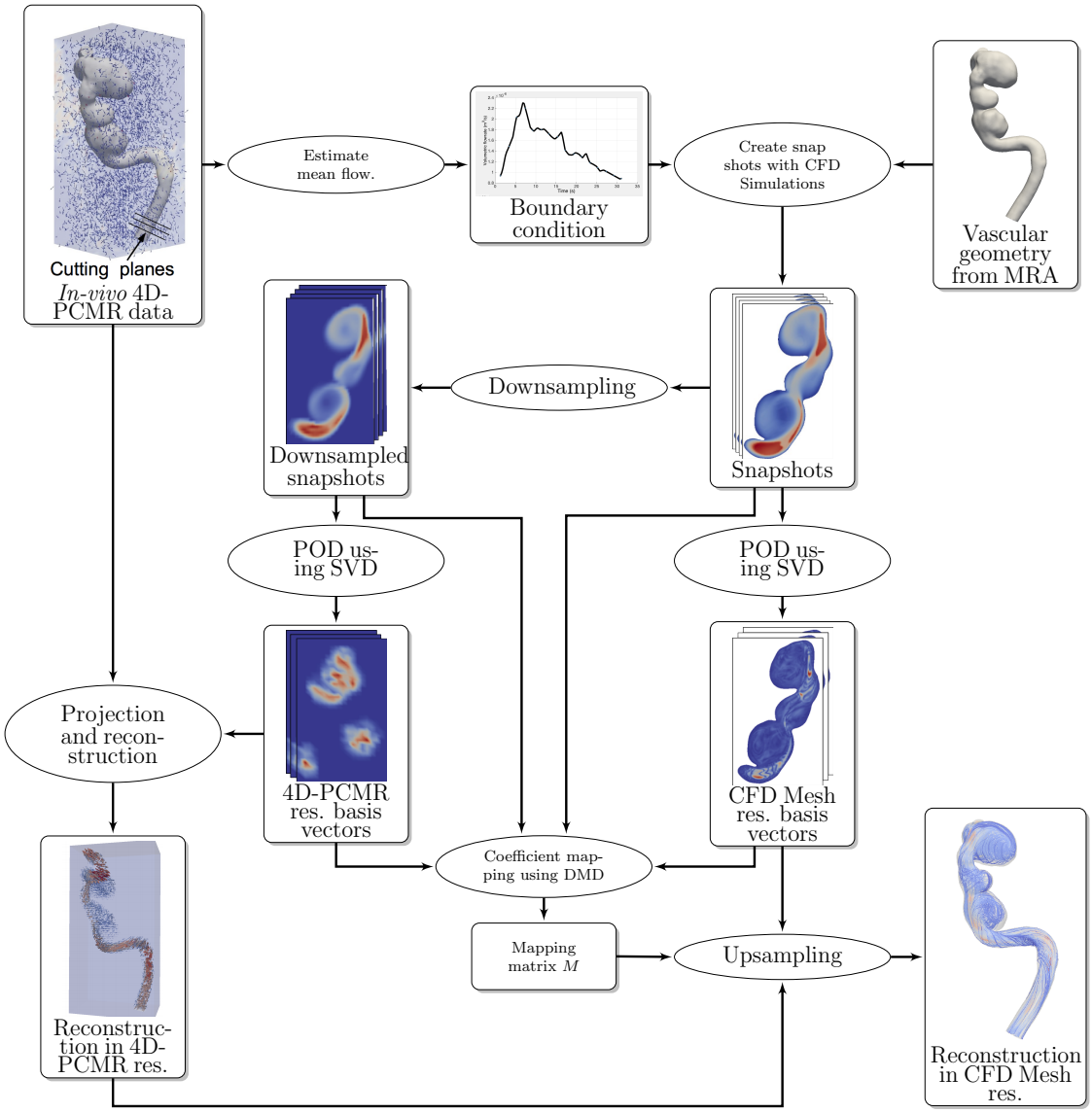

Figure 4.1: Flow-chart of the hemodynamic velocity reconstruction process using dynamic mode decomposition (DMD).

Table 4.1: Error metrics of denoising and data reconstruction using different methods for a numerical phantom. The noise level was equal to 15% of the maximum velocity magnitude. All the reported results are in the regular grid of the 4D-Flow MRI.

Metric / Method	d-CFD reference + noise	DFW-sm	DFW-sms	TV	POD-RR	POD-DM
vNRMSE	6.00	5.14	4.21	3.60	0.29	0.28
sNRMSE	3.85	4.12	3.62	2.94	0.19	0.20
DE	9.58	3.65	2.22	2.55	0.14	0.15

Comparison with state-of-the-art denoising methods

The results from the POD-DMD method were compared with state-of-the-art methods (i.e. Divergence-free wavelet with SureShrink (DFW-sm), Divergence-free wavelet with SureShrink and cycle spinning (DFW-sms), and Total Variation (TV)) [96, 13]. We created a numerical phantom with noise of amplitude equal to 15% of peak velocity values. (Fig. 4.2 (a) to (c)). It can be seen that the POD-DMD/RR method generates errors that are an order of magnitude lower (Fig. 4.2(d), Table 4.1). Furthermore, both POD-RR and POD-DMD are able to accurately super-resolve velocity fields in the CFD mesh. Note that in POD-RR, the weighting factor β was chosen using a time-consuming hand tuning approach to minimize error. In case of POD-DMD, the process was entirely autonomous.

$$\text{vNRMSE} \triangleq \frac{1}{\max_i \left(\left|\mathbf{u}^L_{i,ref}\right|\right)} \sqrt{\frac{1}{N}\sum_{i=1}^{N}\left|\mathbf{u}^L_{i,ref} - \mathbf{u}^L_{i,rec}\right|^2} \tag{4.1}$$

$$\text{sNRMSE} \triangleq \frac{1}{\max_i \left(\left|\mathbf{u}^L_{i,ref}\right|\right)} \sqrt{\frac{1}{N}\sum_{i=1}^{N}\left(\left|\mathbf{u}^L_{i,ref}\right| - \left|\mathbf{u}^L_{i,rec}\right|\right)^2} \tag{4.2}$$

$$\text{DE} \triangleq \frac{1}{N}\sum_{i=1}^{N}\left(1 - \frac{\left|\mathbf{u}^L_{i,ref} \cdot \mathbf{u}^L_{i,rec}\right|}{\left|\mathbf{u}^L_{i,ref}\right|\left|\mathbf{u}^L_{i,rec}\right|}\right) \tag{4.3}$$

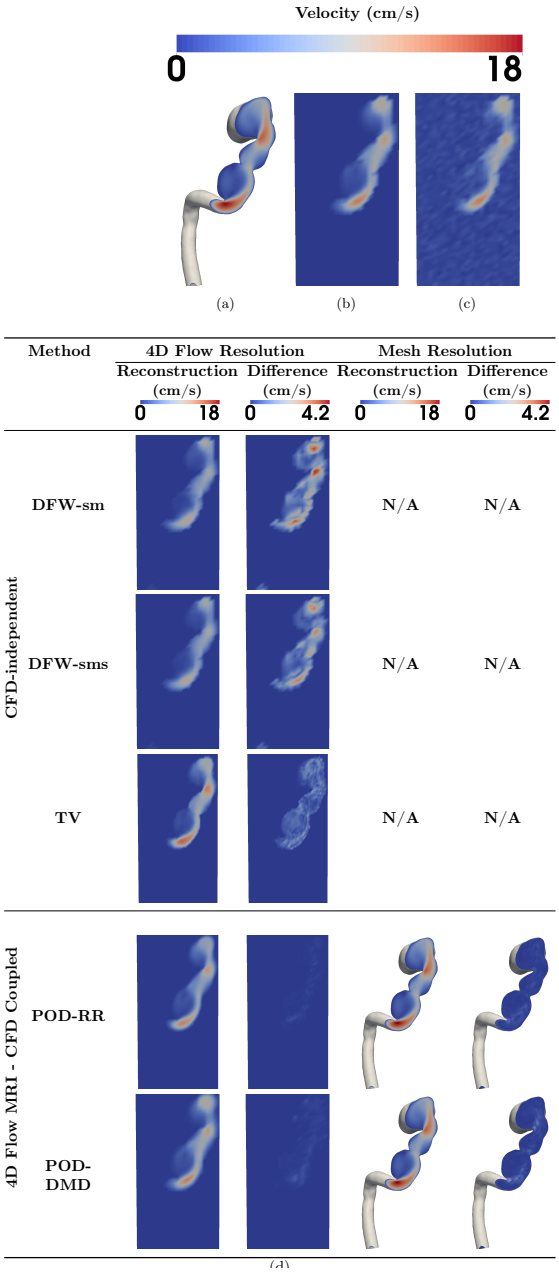

Figure 4.2: 4D-Flow MRI data reconstruction using different available methods. Image (a) shows the CFD reference (CFD ref.). (b) Shows the downsampled CFD ref. into 4D-Flow MRI grid (d-CFD ref.). (c) shows the result of adding simulated k space noise to d-CFD ref. to generate the numerical phantom (d-CFD ref. + noise). (d) shows the reconstruction results using different methods. Reconstruction in high spatial resolution (resolution of the CFD mesh) is only available for POD-DMD and POD-RR.

Comparison between POD-DMD and POD-RR

We compared the performance of POD-DMD and POD-RR on a second patient-specific aneurysm geometry. As before, Fig. 4.3 (a), (b), and (c) represent the slice of geometry, the CFD reference velocity field, and the numerical phantom with added noise equal to 15% of peak velocity, respectively. Fig. 4.3 (d) represents the result of pure CFD simulation with BFCs obtained from the numerical phantom. Fig. 4.3 (e), (f), (g) represents the result of POD-RR for β = 100,β = 0.01, β = 0.0001, respectively. Notice β = 0.01 has minimum error. This value is difficult to obtain when real patient data is the input. Fig. 4.3 (h), (i), and (j) represent the results of POD-DMD where the number of DMD modes for coefficient mapping are 3, 44, and 88 respectively. Fig. 4.3 (h), (j) represent the case for under-fitting and over-fitting, respectively. Fig. 4.3 (i) represents the case where the SVHT algorithm automatically selects the optimal number of modes (44). It can clearly be seen that the autonomous POD-DMD algorithm performs as well as the hand tuned POD-RR algorithm.

Comparing in-flow boundary conditions

One of the important parameters that can be computed using 4D-Flow MRI is volumetric flow at the inlet(s) and outlet(s). Here we tested the ability of our algorithms to recover the time-varying in-flow condition. We placed a plane perpendicular to the centerline of the proximal artery and computed the flow for the flow-field from the numerical phantom (d-CFD reference with noise), the downsampled CFD reference, POD-RR, and POD-DMD. From Fig. 4.4, it can clearly be seen that both POD-DMD, and POD-RR are able to recover the original in-flow that was used to generate the CFD reference.

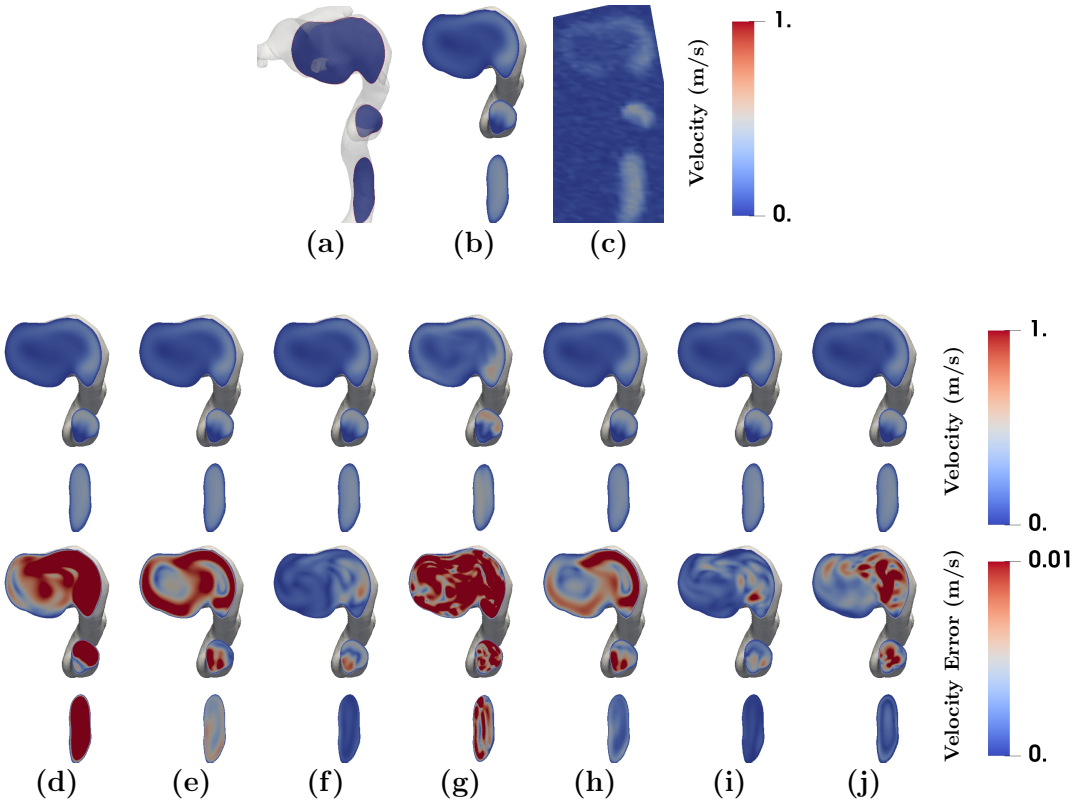

Figure 4.3: Error analysis of reconstructed data using pure CFD, POD-RR, and POD-DMD. (a) Shows the location of slice, image (b) represents the CFD reference simulation, (c) represents downsampled CFD reference after adding 15% of maximum velocity noise causing (vNRMSE=6.00, sNRMSE = 3.85, DE = 9.58) . This is the simulated 4D-Flow MRI data. For (d)-(j), the top row represents the magnitude of velocity and the bottom row represents the absolute error against CFD reference. (d) is pure CFD using boundary conditions measured from the simulated 4D-Flow MRI. This resulted in (vNRMSE=2.0, sNRMSE=1.2, DE=2.3). (e) is reconstruction using POD-RR with β = 100. This resulted in (vNRMSE=2.0, sNRMSE=1.3, DE=3.2). (f) shows the reconstruction using POD-RR with β = 0.01. This resulted in (vNRMSE=0.4, sNRMSE=0.77, DE=0.46). (g) shows the reconstruction using POD-RR with β = 0.00001, resulted in (vNRMSE=2.0, sNRMSE=1.5, DE=2.4), (h) is a reconstruction using POD-DMD with manual selection of coefficient mapping DMD modes equal to 3. This resulted in (vNRMSE=1.2, sNRMSE=1.7, DE=2.0). This is a case of of under-fitting. (i) shows the reconstruction using POD-DMD with autonomous mode selection using SVHT (resulting in 44 DMD modes) for coefficient mapping. This resulted in (vNRMSE=0.5, sNRMSE=0.69, DE=0.44). (j) shows the reconstruction and error using POD-DMD by manually selecting coefficient mapping DMD modes equal to 88. This resulted in (vNRMSE=0.98, sNRMSE=0.87, DE=0.45). This is a case of over-fitting.

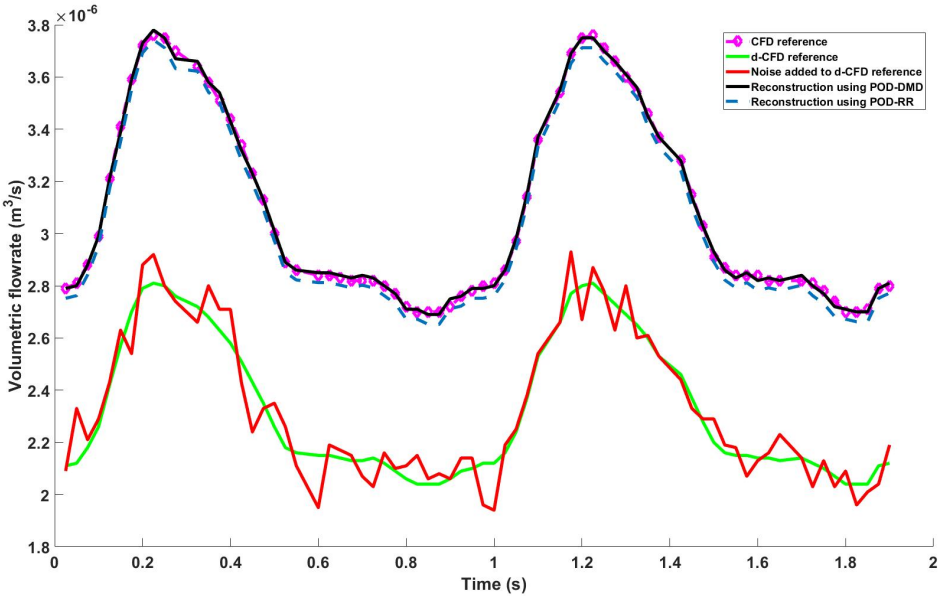

Figure 4.4: Boundary condition comparison for the numerical dataset.

4.3.2 *in-vivo* data

We finally tested our algorithm on *in-vivo* data (Fig. 4.5). 4D-Flow imaging was performed on an aneurysm patient using a 3T MRI scanner (GE, Discovery MR750). We used a 3D phase-contrast peripherally-gated sequence in the axial plane to cover the Circle of Willis focusing on the region of aneurysm. The data was processed using an in-house code to corrected for random noise and eddy currents. We used the method described by Walker et al. [129] for eddy current corrections. For this dataset, pre-emphasis in the sequence takes care of gradient field nonlinearities. In this test, we compared the flow field resulting from a pure CFD simulation using boundary flow conditions obtained from 4D-Flow MRI, POD-RR, and POD-DMD. While the flow field patterns are similar, pure CFD shows much higher peak velocities as compared to 4D-Flow MRI and reconstructed POD-RR and POD-DMD. Meanwhile, POD-RR and POD-DMD flow fields are nearly identical with peak velocity values between those of pure CFD and 4D-Flow MRI.

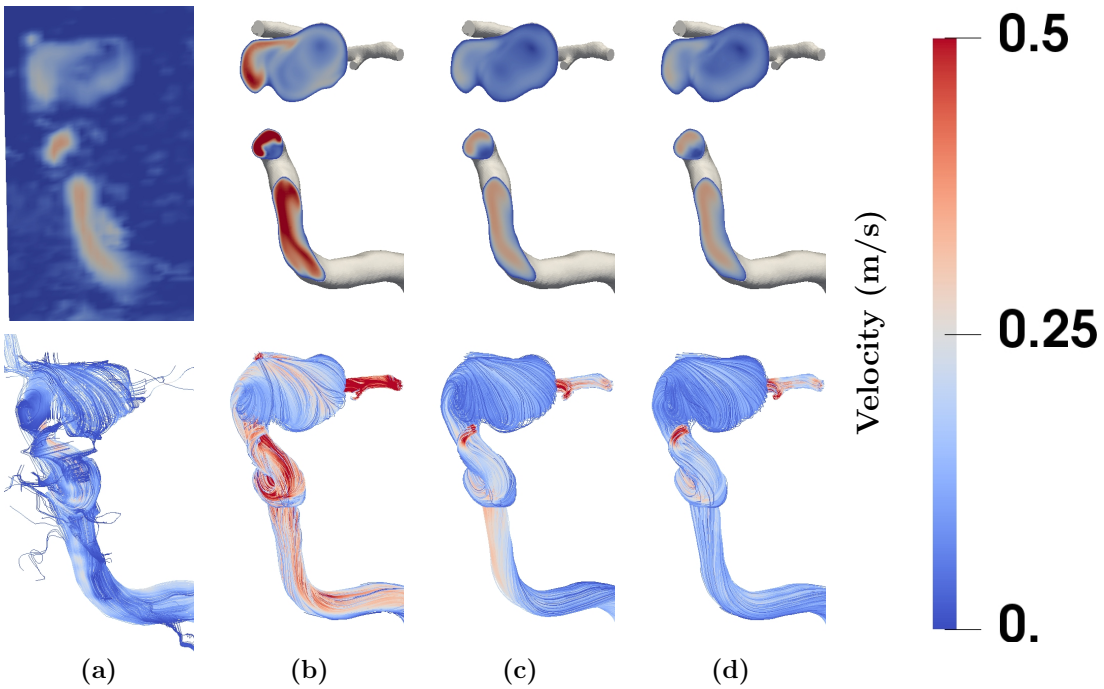

Figure 4.5: *in-vivo* datasets, image (a) shows the velocity profiles in the eddy current corrected dataset, (b) represents the patient-specific model, (c) is the reconstruction using POD-RR with $\beta = 0.01$, and (d) is reconstruction using POD-DMD.

4.4 Discussion

While 4D-Flow MRI has emerged as a potent new tool for in-vivo measurement of time-resolved velocity fields, issues such as spatio-temporal resolution and noise have limited its use in a clinical setting. Our previous paper showed that it is possible to improve spatio-temporal resolution by merging CFD and 4D-Flow MRI (POD-RR). In this paper, we report on improvements that make the method autonomous (POD-DMD). The key idea was the reformulation of the projection coefficient mapping process in terms of DMD[124]. Furthermore, the selection of the number of DMD modes was automated using the SVHT algorithm[54].

Test results on two numerical phantoms Fig. 4.3,4.2 show that autonomous POD-DMD does not suffer from loss in accuracy as compared to the hand-tuned POD-RR method. Figs. 3(e)-3(g) show that selecting a wrong parameter β for

POD-RR can significantly impact the error. Similarly, manually selecting the number of DMD modes in POD-DMD can also impact accuracy (Figs. 3(h)-3(j)). Pure CFD with boundary flow conditions obtained from 4D-Flow MRI is affected by inaccuracy in the BFCs and is less accurate (Fig. 3(d)) when compared to POD-DMD/RR. Fig. 4 illustrates the effect of spatial resolution on flow quantification and validates other research in this area [32], i.e., spatial resolution distorts the velocity field because of averaging. Incredibly, our approach (POD-RR/DMD) is able to recover the original prescribed BFC for the reference, given as input the low resolution noisy flow-field of the numerical phantom.

Tests on the *in-vivo* data set shows significant difference between pure CFD and POD-DMD/RR unlike the numerical phantom in Fig 3. Visually, POD-DMD/RR is much closer to the *in-vivo* data set. We suspect that this difference could be because of the incorrect assumption on the flow model (newtonian vs non-newtonian, laminar vs turbulent) in the pure CFD simulation. Our algorithm tries to correct for this error by merging CFD and 4D-Flow MRI. In depth analysis of this topic will be the subject of a forthcoming publication.

There are other issues such as segmentation and registration errors that should be investigated. Also, the method has to be verified using *in-vitro* models of actual patient geometry using flow measuring techniques such as particle image velocimetry (PIV). Finally, the number of patient geometries and data sets that we have applied this technique to is quite small (3). We are in the process of collecting up to 15 patient data sets to run small cohort trials.

4.5 Conclusions

In this work we have developed a completely autonomous method for physics-based super resolution of 4D-Flow MRI data. This work has the potential to address some of the major limitations of 4D-Flow including partial voluming [138], complex flow pattern resolution in low-velocity regions[27], and acquisition noise. This will enable accurate computation of spatio-temporal maps of parameters such as wall shear stresses (WSS) [23]. This may enable new risk stratification parameters/protocols with significant impact on patient-specific prognosis and treatment decisions resulting in improved outcomes in patients with ICAs and other cerebrovascular diseases.

Chapter 5

Effect of Physics-based Superresolution of 4D flow MRI on Wall Shear Stress Values and Patterns[1]

5.1 Introduction

Wall shear stress (WSS) is the tangential force on the luminal wall due to velocity gradients and viscosity of the fluid [51]. WSS has been implicated in many pathological conditions in intra-cranial aneurysms (ICAs) including ICA formation[75], ICA progression [17], and rupture [26]. It is believed that WSS on endothelial cells lining the vessel lumen provides mechanical stimuli which in turn result in biological signals to regulate vascular homeostasis [91]. Prolonged changes in WSS from physiological levels leads to several cell-mediated processes such as vascular remodeling, extracellular matrix degeneration, cell mortality and inflammatory responses. Based on histological findings, Meng et al. [88] have proposed that high WSS can lead to mural-cell mediated destructive cell remodeling leading to ICA initiation. Subsequently, the change in flow patterns can lead to aberrantly low WSS, which in turn lead to inflammatory response and ICA growth.

[1]The preliminary results from this chapter was presented in the following conference paper:

[7] **Bakhshinejad, A.**, Fathi, M. F., Saloner, D., Nael, K., Rayz, V. L., & DSouza, R. M. (2018). Case study: Coupling 4D flow MRI with CFD using Proper Orthogonal Decomposition and Dynamic Mode Decomposition. In 8th World Congress of Biomechanics. Dublin, Ireland.

5.1.1 Estimating WSS

Two dimensional phase contrast magnetic resonance imaging (2D-PCMRI) has been used to non-invasively measure blood velocities in the cardio-vascular system. Researchers have used this data to further compute local WSS based on these velocity measurements [82]. The simplest approach is based on the average flow rate computed from 2D-PCMRI with the equation

$$\text{WSS} = \frac{4\eta Q}{\pi r^3} \tag{5.1}$$

where Q is the volume flow rate, η is the viscosity and r is the radius of the blood vessel. This assumes a circular cross-section of the blood vessel with fully developed. The flow rate is computed from the 2D-PCMRI velocities as

$$Q = 2\pi \int_0^r v(\eta)\eta \, \mathrm{d}\eta \tag{5.2}$$

where $v(\eta)$ is the velocity as measured by 2D-PCMRI at a distance of η from the center of the blood vessel. This method cannot handle cross-sections that are not circular nor radial asymmetries in the velocity profile.

Oshinski et al. [97] overcame the problem of asymmetric velocity profiles by using linear interpolation. In their approach, a straight line is drawn from a point on the boundary where the velocity is zero ($v_{wall} = 0$) to an interior point at a distance $\mathrm{d}x$ along the surface normal of the vessel boundary. The velocity v_{int} at the interior point is sampled from 2D-PCMRI data and the WSS at the boundary point is calculated as

$$\text{WSS} = \eta \frac{\mathrm{d}v}{\mathrm{d}x} = \eta \left(\frac{v_{int} - v_{wall}}{\mathrm{d}x} \right) \tag{5.3}$$

Since the flow inside the blood vessel with fully developed Poiseuille flow is

parabolic, Oyre et al. [98] developed a method to locally fit a 3D paraboloid whose equation is given by

$$v(x, y) = a(x^2 + y^2) + bx + cy + d \tag{5.4}$$

The WSS was computed by transforming the paraboloid to a radial coordinate system. The equation for WSS in the radial coordinate system is given by

$$\text{WSS} = \eta \left.\frac{\mathrm{d}v}{\mathrm{d}r}\right|_{wall} \tag{5.5}$$

Only points in a band between the center and vessel wall boundary were selected for the fit. Using this method, WSS at several points along the boundary may be calculated.

The methods described above are susceptible to vessel wall segmentation errors, truncation errors and errors due to effects of partial voluming [120, 99] near the boundary. There are several prescribed methods to mitigate these errors.

Frequently, the velocity profiles inside the blood vessel may other than parabolic. To account for this, Cheng et al. [30], used a local Lagrangian polynomial fit. Given this fit, the WSS was calculated as

$$\text{WSS}(x, y) = \eta \left(\nabla v(x, y) \cdot \boldsymbol{n}\right) \tag{5.6}$$

With the advent of 4D flow MRI, it has now become possible to scan 3 dimensional time resolved velocities. This allows for retrospective placements of planes in any location and computing flow velocities at the plane cross-section. Unlike 2D-PCMRI, planes do not have be orthogonal to the flow direction in order to accurately quantify flow. Consequently, the computations of WSS are likely to be more accurate. On the other hand, due to the scan times involved, the spatio-temporal

resolution is much lower as compared to 2D-PCMRI.

The basic approach to computing WSS from 4D flow MRI has been to retrospectively place planes at given locations and sample the 3D velocity field on the plane. Next, either a high order polynomial interpolation or a piecewise continuous (B-Spline) interpolation is used to fit the available velocity data to a continuous function [73, 115]. Finally, the WSS tensor is computed as

$$\vec{\mathrm{WSS}} = 2\eta\dot{\epsilon} \cdot \boldsymbol{n} \tag{5.7}$$

where $\dot{\boldsymbol{\epsilon}}$ is the strain rate tensor whose components are given by

$$\dot{\epsilon}_{ij} = \frac{1}{2}\left(\frac{\partial v_i}{\partial x_j} + \frac{\partial v_j}{\partial x_i}\right) \tag{5.8}$$

The main drawback of computing WSS directly from 4D flow MRI is the issue of spatio-temporal resolution and noise. In cases of small blood vessels such as those that occur intra-cranially, frequently there are only 3-4 voxels of data in some blood vessel whose diameter is of the order of 2-3 mm. This data may not be sufficient to generate a good functional fit. Furthermore, polynomial interpolation of velocities will cause artifacts which can render the resulting interpolated field non-divergence free.

Alternatively, several researchers have used CFD to compute WSS [102, 18]. The boundary conditions, typically inflow and outflow are computed from 4D flow MRI data. Furthermore, there are certain logical assumption that are made regarding the type of flow (laminar vs newtonian vs non-newtonian) and model constants (dynamic viscosity). The spatio-temporal resolution is only limited by the computing and memory power available. Furthermore, commercial CFD packages such as CFX,

Fluent and open source packages such as OpenFoam have function to compute the WSS tensor once the velocity field is computed.

In this chapter, we apply the POD-DMD method developed in chapter 4 to compute WSS in high resolution. We generate a numerical phantom using actual patient geometry and realistic boundary conditions. Time averaged wall shear stress patterns were generated for the reference velocity field, numerical phantom, pure CFD, and the results of POD-DMD. Finally, the POD-DMD method was applied to 3 different patient data sets to generated detailed spatial WSS maps.

5.2 Method

In this section we describe data preparation for the POD-DMD method as well as the generation of the numerical phantom. POD-DMD requires a CFD simulation which in turn requires vessel geometry and boundary conditions. Furthermore, the 4D flow MRI data has to be registered with the CFD simulation data. These steps are explained in detail in the following sections. We also describe the process of creating a realistic numerical phantom.

5.2.1 Lumen segmentation and Registration

The Vascular Modeling Toolkit (VMTK) package was used for lumen segmentation. The magnitude image from 4D flow MRI gives an anatomical view of arteries, however, the resolution of this image is not sufficient to be used for patient-specific simulation models (Fig. 5.1). Therefore, another segmentation was performed on high resolution time of flight (TOF). The two segmentations have to be co-located in order to do point-by-point association of velocities. Due to different imperfections, these two models never match exactly in the three dimensional space. To resolve

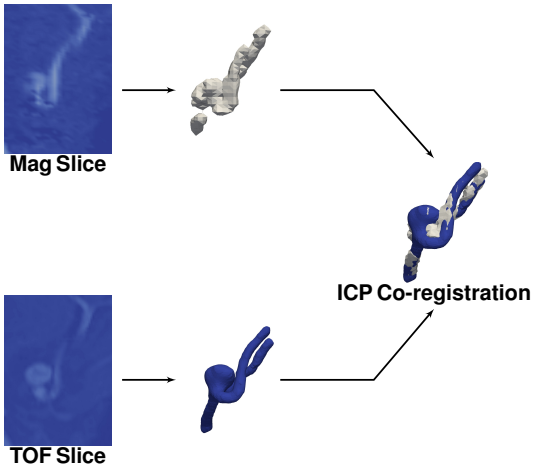

Figure 5.1: Steps of lumen segmentation. The process starts with two parallel segmentations, the first from the magnitude image of 4D flow (Mag Slice in the figure) and the second from the time of flight (TOF Slice). After obtaining both surface files, the low resolution reconstructed surface from Mag Slice will be used as the base mesh and the high resolution surface from TOF Slice will be co-registered to the same location. We are using Iterative Closest Point (ICP) co-registration algorithm.

the problem, we are using an Iterative Closest Point (ICP) co-registration algorithm to match the location. In this method, up to five identical points were selected by the user and the algorithm tries to minimize the error using the selected five points as the base.

5.2.2 Volumetric mesh

The segmented lumen geometry from the TOF images is used to construct the descritized mesh for numerical solving the flow. We used the ANSYS ICEM CFD package to generate our volumetric mesh. Near wall regions were segmented with a fine mesh $\tilde{0}$.1mm size. This typically resulted in a mesh size of 600,000-1,200,000 finite volumes. The co-registered lumen surface is the input for the meshing processes and the output is a mesh file in the format of a series of vertices and their connectivity.

5.2.3 Boundary condition calculation

The boundary flow conditions (inflow in the proximal arteries and outflow in distal arteries) were estimated form the 4D flow MRI data (Fig. 1.4). Using the co-registered lumen segmentation, the centerline of the lumen surface needs to be calculated. The VMTK package was used for this purpose. Several planes normal to the centerline were place at the inlet(s) and outlet(s). The flow rates were calculated by integrating the velocity over the area as

$$Q = \int_A \vec{v} \cdot \vec{n}_A \, \mathrm{d}A \tag{5.9}$$

where $\vec{n}_A$ is the normal to the plane. For each inlet and outlet, the flow was estimated at several locations and averaged. The mean inflow was taken as calculated. Due to noise and error in measurements, the measured inflow will not match measured outflow. Therefore, for each outflow, the flow was divided proportionally according to the measured mean outlfow. This balanced the flow conditions. For example, the balanced outflow Q^*_{oi} from the i^{th} distal branch was computed as

$$Q^*_{oi} = \frac{Q_{oi}}{\sum_j Q_{oj}} \cdot \sum Q_{in} \tag{5.10}$$

5.2.4 Merging 4D flow MRI and CFD

We use the POD-DMD algorithm described in chapter 4 to merge 4D flow MRI data and CFD. Using the approximate boundary conditions from the 4D flow MRI data computed as described previously, a CFD simulation was executed on the patient specific geometry. The Semi-Implicit Method for Pressure Linked Equations (SIMPLE) algorithm was used by finite-volume solver OpenFOAM. The flow was modeled as an incompressible and Newtonian fluid with the density of $1060 kg/m^3$ and dynamic viscosity of $0.0035 Pa.s$. It has been shown in different papers that a

rigid wall is a good assumption for an intra-cranial aneurysm [102, 6]. Therefore, we adopted the same assumption and ran our models with rigid wall and the no-slip boundary condition at walls. The simulation was carried out for upto 4 cardiac cycles to ensure that the flow patterns through the cardiac cycles were repitative. Finally, solution snapshots of the final cardiac cycle was used in the POD-DMD algorithm described previously.

5.2.5 Wall Shear Stress Algorithm

3D shear stress vector was computed as in equations 5.7, 5.8. In the expanded form, the shear stress vector is given by

$$\vec{WSS} = 2\mu \left[\begin{array}{l} \frac{\partial v_x}{\partial x} \cdot n_x + \frac{1}{2}\left(\frac{\partial v_y}{\partial x} + \frac{\partial v_x}{\partial y}\right) \cdot n_y + \frac{1}{2}\left(\frac{\partial v_z}{\partial x} + \frac{\partial v_x}{\partial z}\right) \cdot n_z \\ \frac{1}{2}\left(\frac{\partial v_x}{\partial y} + \frac{\partial v_y}{\partial x}\right) \cdot n_x + \frac{\partial v_y}{\partial y} \cdot n_y + \frac{1}{2}\left(\frac{\partial v_z}{\partial y} + \frac{\partial v_y}{\partial z}\right) \cdot n_z \\ \frac{1}{2}\left(\frac{\partial v_x}{\partial z} + \frac{\partial v_z}{\partial x}\right) \cdot n_x + \frac{1}{2}\left(\frac{\partial v_y}{\partial z} + \frac{\partial v_z}{\partial y}\right) \cdot n_y + \frac{\partial v_z}{\partial z} \cdot n_z \end{array} \right]\Bigg|_{\partial\Omega} \tag{5.11}$$

with μ be blood viscosity ($3.2\times10^{-3}Pa$),v_x, v_y, v_z are the velocity coordinates and n_x, n_y, n_z are the surface normal coordinates in the global coordinate system. The wall shear stress vector is evaluated at all points on the lumen boundary $\partial\Omega$.
The WSS vector can be split into two components: one that is parallel to the normal $\vec{n}$ given by

$$\vec{WSS}_{\vec{n}} = (\vec{WSS} \cdot \vec{n})\vec{n} \tag{5.12}$$

and one that is the tangential plane given by

$$\vec{WSS}_{\vec{t}} = \vec{WSS} - (\vec{WSS} \cdot \vec{n})\vec{n} \tag{5.13}$$

The WSS vector in 4D flow MRI grid was computed using the open-source software Paraview. In order to be able to calculate the velocity gradient on the wall of the re gion of interest, the 4D flow velocity data were re-sampled on the

surface generated from the lumen segmentation step. Then the gradient tensor was calculated for the velocities on the wall surface. Using the surface from the segmentation and the gradient tensor, we were able to solve Eq. 5.11. The WSS vector in the CFD mesh was computed using OpenFoam which provides a dedicated library function.

5.2.6 Building a numerical flow phantom

In order to test the accuracy of our algorithm, we used a numerical flow phantom. An actual aneurysm geometry was used in this exercise. The geometry was meshed using the ANSYS ICEM CFD package. Realistic boundary conditions were applied at the proximal and distal arteries. The simulation was run till the flow patterns stabilized between cardiac cycles. Snapshots of the simulation at 80ms intervals were collected and down sampled into the low resolution cartesian grid whose cell size mimicked that 4D flow MRI acquisition. Next k-space gaussian noise was added to the downsampled velocity field to generate the simulated 4D flow MRI data [25]. The process is illustrated in Fig. 5.2.

5.2.7 Study cohort and MR imaging

Three subjects were recruited, including a healthy subject (H1), and two cerebral aneurysm patients (A1 and A2), for this study and underwent MRI scans using a 3T MRI scanner (GE, Discovery MR750). ECG synchronized gated 4D flow MRI was performed using free breathing. Post-processing of 4D flow data included corrections of Eddy currents and random noise was performed using algorithm introduced by Walker et al. [129]. The study was approved by our local Institutional Review Board and informed consent was obtained from all subjects.

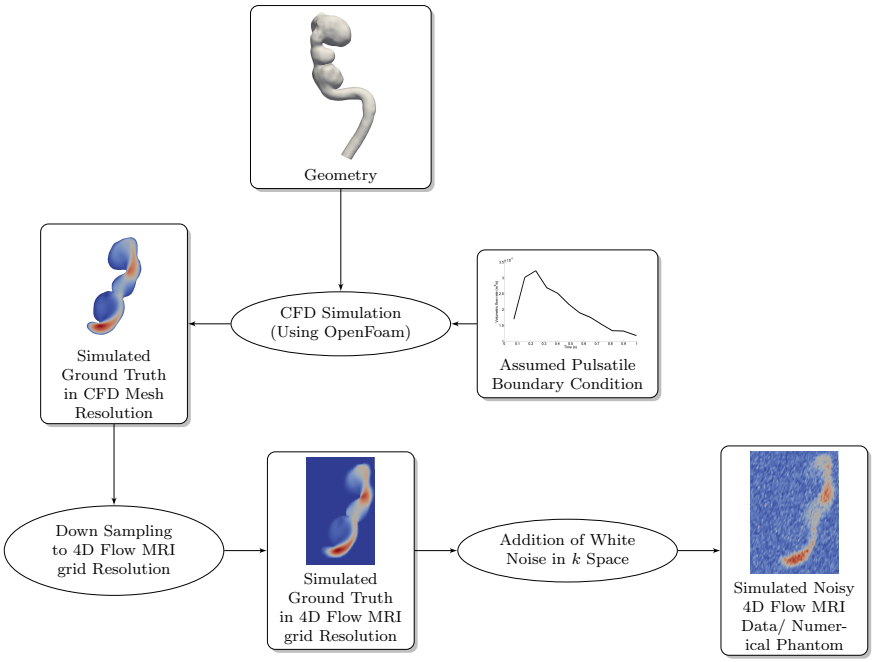

Figure 5.2: Building a numerical flow phantom

5.3 Results

In this section, we compared the results of computing WSS from velocity fields generated using pure CFD, POD-DMD, DFW-sms, and TV. DFW-sms and TV do not increase the resolution of the velocity beyond what is available in 4D flow MRI data. The resolution of pure CFD and POD-DMD is determined by the size of the CFD computational mesh.

5.3.1 Particle tracing analysis

Particle tracing has been shown to be a good visual aid to visualize the improvement in flow data after denoising. Our healthy subject data was used for this analysis. Around one thousand virtual particles were released into the region (Fig. 5.3) and particles leaving the area were counted at outlets. In case of raw 4D flow MRI data, Fig. 5.3(a), just less than 2% of particles were observed at the outlets. After removing random noise and phase errors (i.e. Eddy currents), the number of ob-

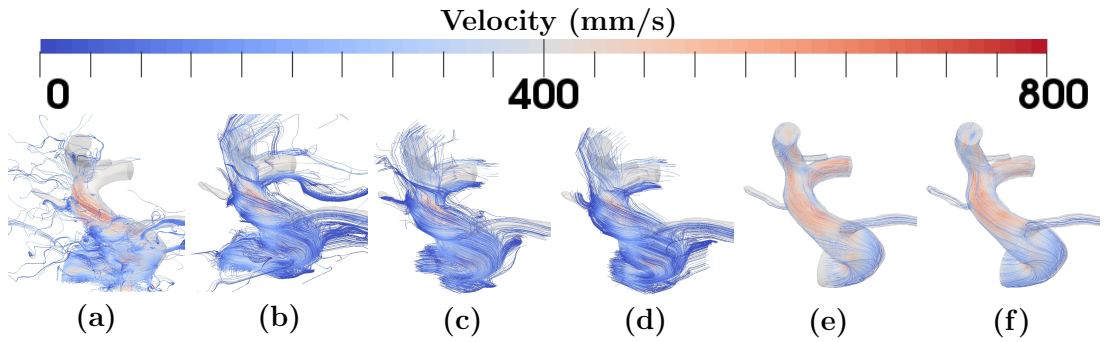

Figure 5.3: Particle tracing analysis for a healthy subject (H1) was performed. Image (a) shows the raw 4D flow MRI where about 2% of particles released from inlet were observed in the outlets. The number of particles increased significantly after removing random noise and eddy currents using a second order polynomial up to 30% as shown in image (b). Image (c) shows the particle traces after denoising using divergence free wavelets, the number of receiving particles reached to about 48%. Improved results using total variation algorithm shown in (d) which was about 61%. Image (e) shows results from computational fluid dynamics which is about 98%. And image (f) is results of proper orthogonal decomposition and dynamic mode decomposition around 96%.

served particles increased significantly up to about 30% (Fig. 5.3(b)). Removing the divergence in data using DFW-sms (Fig. 5.3(c)) further increased the number of observed particles to around 48%. As the secondary denoising method in 4D flow resolution, TVN was used (Fig. 5.3(d)). The observed particles after using TVN was up to around 61%. The patient-specific CFD model (Fig. 5.3(e)), provides the best results with more than 98% counted at outlets. Finally, coupling of CFD with 4D flow MRI, using POD-DMD algorithm, results in about 96% of particles leaving the area.

As reported by other researchers as well [32, 102], the velocity values are slightly higher in CFD and POD-DMD methods. However, high and low velocity regions are in good agreement.

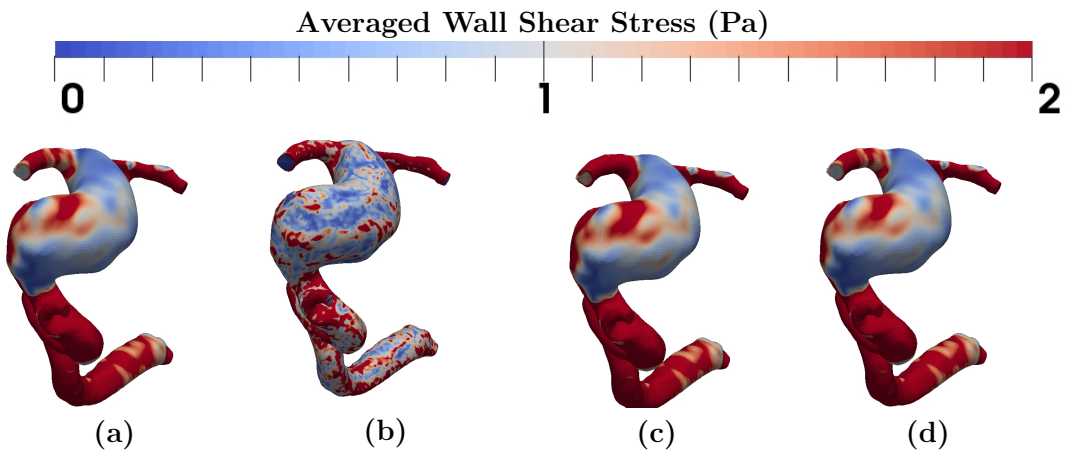

Figure 5.4: Comparison of WSS computation. (a) Reference WSS pattern. (b) Numerical phantom, (d) WSS from pure CFD with boundary conditions obtained from numerical phantom. (d)WSS from POD-DMD

5.3.2 Verification using a numerical phantom

A numerical phantom was generated as described previously. Time averaged WSS patterns were generated from the velocity field of the reference CFD simulation (Fig. 5.4(a)), the numerical phantom (downsampled reference CFD with added k-space noise) (Fig. 5.4(b)), pure CFD simulation using boundary conditions from the numerical phantom 5.4(c)), and finally from the POD-DMD algorithm 5.4(d)). Clearly, it can be seen that WSS computations from downsampled noisy velocity fields is quite different from the reference. While the patterns resulting from pure CFD and POD-DMD are quite similar, there are differences in the pattern on the body of the aneurysm as can be seen in Fig 5.4 (a,c,d). The small differences in POD-DMD and pure CFD WSS patterns are due to the uncertainty in boundary conditions (which are measured from the noisy numerical phantom) are model parameter uncertainties (dynamic viscosity).

5.3.3 Wall Shear Stress using *in-vivo* data

WSS was calculated for three different patient datasets. First the WSS was calculated directly using raw 4D flow (Fig. 5.5(a)). The second column of Fig. 5.5(b)

shows the WSS after correcting for eddy currents. The WSS for denoised data using DFW-sms is shown in column c of Fig. 5.5. Next WSS for denoised data using TVN was calculated as shown in Fig. 5.5(d). WSS using a patient-specific CFD model is shown in column (e) of Fig. 5.5. Finally, WSS using denoised data using POD-DMD algorithm is shown in Fig. 5.5(f).

As it can be observed in Fig. 5.5, WSS calculated directly using patient-specific CFD has the highest value. Followed by POD-DMD reconstructed data, and raw 4D flow MRI, respectively. Eddy current corrected data, DFW-sms, and TVN corrections are look almost identical, however, small pattern detail differences can be observed. Overall, all datasets share high and low WSS areas regardless of exact values and method.

5.4 Discussion

In this study, we have evaluated the accuracy of computing WSS using different methods. We calculated WSS using six different methods: (1) raw 4D flow MRI, (2) eddy current corrected 4D flow MRI, (3) DFW-sms, (4) TV, (5) pure CFD, and (6) POD-DMD. To the best of our knowledge, this is the first study to compare WSS values calculated from multiple different velocity reconstruction methods. Therefore, we believe this study provides a broader understanding of different methods.

While the results shown similar patterns for WSS, the values are quite different with raw eddy current corrected 4D flow MRI data and reconstruction methods such as DFW-sms and TV which reconstruct velocity fields in 4D flow MRI resolution being lower that those obtained from high resolution CFD and POD-DMD. It appears that low resolution acquisition and the averaging effects that it has on the acquired data lowers WSS values. The effect of lowering spatial resolution (Fig.

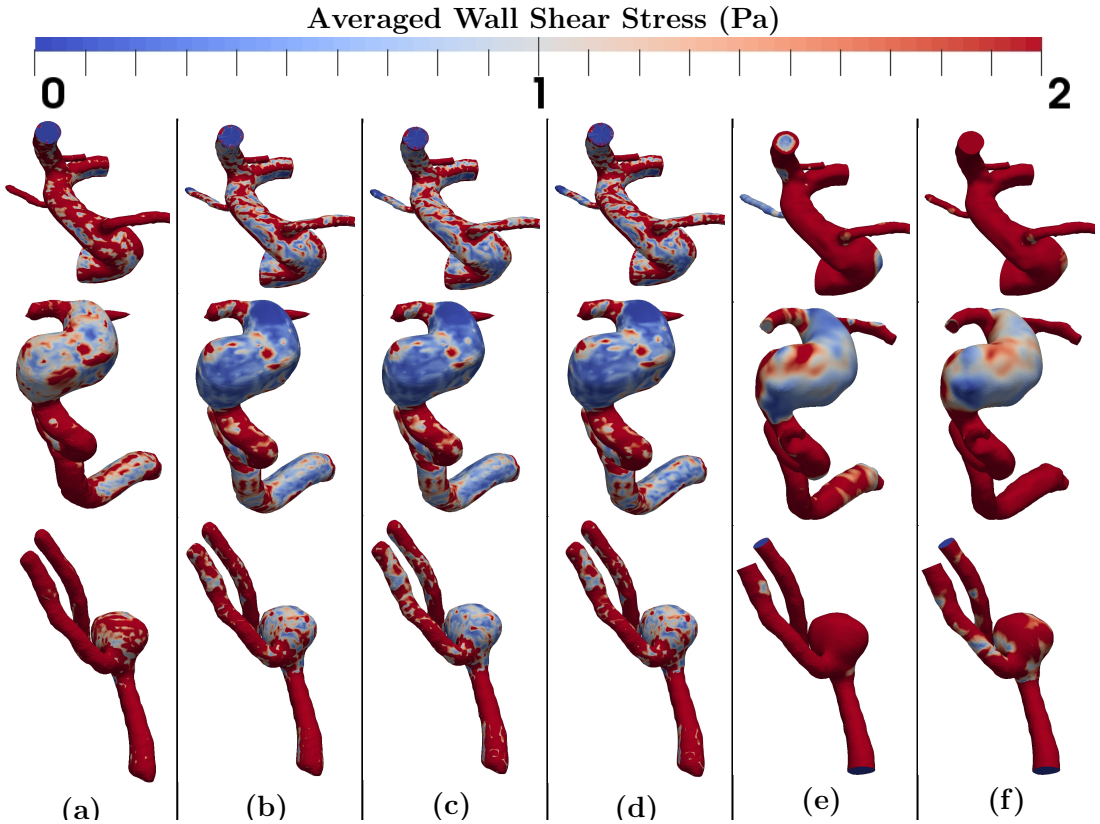

Figure 5.5: Wall shear stress comparison using different reconstruction methods. Column (a) shows raw 4D flow datasets. Column (b) is after removing the random noise and correcting Eddy currents using second order polynomial. Results from removing divergence using DFW-sms is represented in column (c). Next, the removal of divergence using TVN is shown in column (d). Column (e) shows patient-specific CFD results and the last column shows results using POD-DMD algorithm.

5.4(b)) can clearly be seen in tests using a numerical phantom where the reference WSS is known. We have further shown that WSS can be accurately reconstructed using POD-DMD method. It is also seen that in case of tests on the numerical phantom, the results of pure CFD and POD-DMD are nearly identical with small differences which we can attribute to difference in model parameters between the reference and reconstruction methods. While applying the method to actual patient data (Fig. 5.5) we can see significant differences between pure CFD and POD-DMD. In case of the actual patient data, we attribute this difference to inaccuracy in model parameters as well as errors in segmentations. The POD-DMD method attempts to correct for these errors. In depth research into the performance of POD-DMD method in presence of segmentation errors will be the subject future research.

5.5 Conclusion

In this work we have evaluated the differences between WSS values calculated using velocity fields constructed using different methods. We found that WSS calculated from 4D flow MRI results in an underestimation of these values due to the low resolution, as suggested by other researchers [33]. Therefore, the same problem can be seen in other CFD-independent methods, such as DFW-sms and TV. However, CFD alone cannot be used due to the unavoidable errors in the model assumptions such as segmentation and viscosity model selection errors. Therefore, a correction method such as POD-DMD is required to minimize these kinds of errors.

Chapter 6

Concluding Remarks

6.1 Summary of Contributions

In this thesis we addressed some of the main limitations of 4D-Flow MRI that have prevented its use in routine clinical practice, namely, spatial resolution and noise. We achieved this by merging 4D-Flow MRI data with CFD using data assimilation techniques. We have successfully implemented and tested three different methods.

In chapter 2 we describe implementation of Ensemble Kalman Filter Algorithm (EnKF)-based method for super resolution of 4D-Flow MRI. Based on boundary conditions and geometry derived from scanned data, an ensemble of CFD simulations was used to generate the predictor. Using the ensemble of predicted state values, various matrices used in computing the Kalman gain were computed using sampling. A novel QR-based matrix inversion method was used to handle large matrix sizes in computing the Kalman gain. However, the ensemble CFD simulations are computationally expensive and consume significant computing resources. This method may not be practical in a clinical setting.

In chapter 3, we describe a second method based on proper orthogonal decomposition (POD). Using boundary conditions and geometry derived from scan data, a sample CFD simulation was executed. The snapshots of the simulation were used to generate the POD basis vectors. The POD basis spans the local space of solutions. Downsampled snapshots were used to generate the POD basis in the regular grid

domain of the 4D-Flow MRI data as well. Next, a process of projection of scan data onto the POD basis followed by projection coefficient mapping was used to generate the solution in high resolution of the CFD mesh. We used ridge regression to map the projection coefficients, which required the manual specification of the regression weighting parameter. While the method generated accurate reconstructions when tested with numerical phantoms, the selection of the ridge regression weighting parameter is a major drawback since it makes the method semi-autonomous.

In chapter 3, we describe a modification of the POD-based algorithm described in chapter 2 by replacing the ridge-regression based projection coefficient mapping algorithm with one based on dynamic mode decomposition (DMD). The main contribution was the identification of projection coefficient mapping algorithm with well-researched DMD method. This made the POD-based super-resolution method completely autonomous. Tests on numerical phantoms have shown results that are equal to or superior to the ones using the ridge-regression algorithm.

In chapter 5, we compared the estimation of wall shear stress (WSS), an important hemodynamic parameter, using 4D-Flow MRI, pure CFD, and POD-based methods. In studies on a numerical phantom it was observed that in general, 4D-Flow MRI underestimated WSS. On the other hand pure CFD (based off of estimated boundary conditions and geometry from scan data) produced results with much lower error. However, the accuracy of CFD was affected by errors in boundary conditions, and model assumption. The POD-based method significantly reduced the errors of pure CFD.

6.2 Future work

There are several avenues to further this research. Currently, our method relies on the user to specify the type of flow (laminar/turbulent/newtonian/non-newtonian). An interesting direction of research would include a set of possible flow models in generating the POD basis and find if the method is able to correctly able to select the flow model. Among many factors, CFD solutions are most affected by geometry. Another direction of research would be to research techniques to handle errors in luminal geometry due to segmentation. The current method assume rigid luminal walls. This restricts its application in the areas where the vasculature is surrounded by solid tissue. In case of vessels near the heart such as the aortic arch, there is significant vessel wall motion. Another direction of research would be to include fluid-structure interaction to handle wall motion. Treatment of aneurysms typcially includes insertion of metallic stents and coils. These devices can significantly effect the MRI signal in the local region. Therefore, 4D-Flow MRI is quite limited in the post treatment scenario. One area of research would be to further develop the method to handle gappy data and data with significant metal artifacts.

While the methods presented in this thesis have worked very well with numerically generated data sets, there is a need to verify them using *in-vitro* studies before applying them to studies in clinical trials. Particle image velocimetry (PIV) provides a way to generate velocity fields in transparent models with much higher spatio-temporal resolution compared to 4D-Flow. A final test of the methods presented in this thesis would be to create *in-vitro* models and scan data with controlled flow rates both using PIV and 4D-Flow MRI. The resolution of the 4D-Flow MRI could be enhanced using the aforementioned algorithm to match that of PIV and then results could be compared to check the accuracy.

Finally, our studies so far are limited with low number of patient data. In order to show the effectiveness of these methods, larger study cohorts with different kinds of aneurysms will have to be conducted.

Bibliography

[1] B. Ali, M. F. Fathi, A. Baghaie, R. H. Sacho, K. Nael, D. Saloner, V. L. Rayz, R. M. D'Souza, and D'Souza. 4D Flow MRI Denoising and Spatial Resolution Enhancement: Application of Proper Orthogonal Decomposition Coupled with Dynamic Mode Decomposition. *Under review at Journal of Biomechanics*, 2018.

[2] M. Arigovindan, M. Suhling, C. Jansen, P. Hunziker, and M. Unser. Full Motion and Flow Field Recovery From Echo Doppler Data. *IEEE Transactions on Medical Imaging*, 26(1):31–45, jan 2007.

[3] P. M. Arvidsson, J. Töger, E. Heiberg, M. Carlsson, and H. Arheden. Quantification of left and right atrial kinetic energy using four-dimensional intracardiac magnetic resonance imaging flow measurements. *Journal of applied physiology (Bethesda, Md. : 1985)*, 114(10):1472–81, may 2013.

[4] A. Bakhshinejad, A. Baghaie, V. L. Rayz, and R. M. D'Souza. A proper orthogonal decomposition approach towards merging cfd and 4d-pcmr flow data. In *The 28th Society for Magnetic Resonance Angiography, Chicago, IL, USA*, 2016.

[5] A. Bakhshinejad, A. Baghaie, V. L. Rayz, and R. M. D'Souza. Towards Reconstructing Blood Velocity Profiles from Noisy and Sparse Time Resolved Phase Contrast Magnetic Resonance Flow Data. *University of Wisconsin-Milwaukee, CEAS graduate student poster competition*, March 2016.

[6] A. Bakhshinejad, A. Baghaie, A. Vali, D. Saloner, V. L. Rayz, and R. M. D'Souza. Merging computational fluid dynamics and 4D Flow MRI using

proper orthogonal decomposition and ridge regression. *Journal of Biomechanics*, 58:162–173, jun 2017.

[7] A. Bakhshinejad, M. F. Fathi, D. Saloner, K. Nael, V. L. Rayz, and R. M. D'Souza. Case study: Coupling 4D-Flow MRI with CFD using Proper Orthogonal Decomposition and Dynamic Mode Decomposition. In *8th World Congress of Biomechanics*, Dublin, Ireland, 2018.

[8] A. Bakhshinejad, V. Rayz, and R. M. D'Souza. Reconstructing blood velocity profiles from noisy 4d-pcmr data using ensemble kalman filtering. In *Biomedical Engineering Society (BMES) 2016 Annual Meeting, Minneapolis, MN, USA*, 2016.

[9] G. Berkooz, P. Holmes, and J. L. Lumley. THE PROPER ORTHOGONAL DECOMPOSITION IN THE ANALYSIS OF TURBULENT FLOWS. *Annu. Rev. Fluid Mech*, 25:539–75, 1993.

[10] M. A. Bernstein, X. J. Zhou, J. A. Polzin, K. F. King, A. Ganin, N. J. Pelc, and G. H. Glover. Concomitant gradient terms in phase contrast MR: Analysis and correction. *Magnetic Resonance in Medicine*, 39(2):300–308, feb 1998.

[11] R. B. Bird, R. C. Armstrong, and O. Hassager. *Dynamics of polymeric liquids*. Wiley, 1987.

[12] A. F. Bolger, E. Heiberg, M. Karlsson, L. Wigström, J. Engvall, A. Sigfridsson, T. Ebbers, J.-P. E. Kvitting, C. J. Carlhäll, and B. Wranne. Transit of blood flow through the human left ventricle mapped by cardiovascular magnetic resonance. *Journal of cardiovascular magnetic resonance : official journal of the Society for Cardiovascular Magnetic Resonance*, 9(5):741–7, 2007.

[13] E. Bostan, S. Lefkimmiatis, O. Vardoulis, N. Stergiopulos, and M. Unser.

Improved Variational Denoising of Flow Fields with Application to Phase-Contrast MRI Data. *IEEE Signal Processing Letters*, 22(6):762–766, jun 2015.

[14] E. Bostan, D. P. Tafti, and M. Unser. A dual algorithm for l1-regularized reconstruction of vector fields. In *IEEE International Symposium on Biomedical Imaging (ISBI)*, pages 1579–1582, 2012.

[15] E. Bostan, O. Vardoulis, D. Piccini, P. D. Tafti, N. Stergiopulos, and M. Unser. Spatio-temporal regularization of flow-fields. In *2013 IEEE 10th International Symposium on Biomedical Imaging*, pages 836–839. IEEE, apr 2013.

[16] L. Boussel, V. Rayz, A. Martin, G. Acevedo-Bolton, M. T. Lawton, R. Higashida, W. S. Smith, W. L. Young, and D. Saloner. Phase-contrast magnetic resonance imaging measurements in intracranial aneurysms in vivo of flow patterns, velocity fields, and wall shear stress: Comparison with computational fluid dynamics. *Magnetic Resonance in Medicine*, 61(2):409–417, feb 2009.

[17] L. Boussel, V. Rayz, C. McCulloch, A. Martin, G. Acevedo-Bolton, M. Lawton, R. Higashida, W. S. Smith, W. L. Young, and D. Saloner. Aneurysm growth occurs at region of low wall shear stress: patient-specific correlation of hemodynamics and growth in a longitudinal study. *Stroke*, 39(11):2997–3002, 2008.

[18] L. Boussel, V. Rayz, C. McCulloch, A. Martin, G. Acevedo-Bolton, M. Lawton, R. Higashida, W. S. Smith, W. L. Young, and D. Saloner. Aneurysm Growth Occurs at Region of Low Wall Shear Stress: Patient-Specific Correlation of Hemodynamics and Growth in a Longitudinal Study. *Stroke*, 39(11):2997–3002, nov 2008.

[19] J. Brackbill, D. Kothe, and H. Ruppel. Flip: A low-dissipation, particle-in-cell method for fluid flow. *Computer Physics Communications*, 48(1):25–38, 1988.

[20] J. Bürk, P. Blanke, Z. Stankovic, A. Barker, M. Russe, J. Geiger, A. Frydrychowicz, M. Langer, and M. Markl. Evaluation of 3D blood flow patterns and wall shear stress in the normal and dilated thoracic aorta using flow-sensitive 4D CMR. *Journal of cardiovascular magnetic resonance : official journal of the Society for Cardiovascular Magnetic Resonance*, 14:84, dec 2012.

[21] J. Busch, D. Giese, L. Wissmann, and S. Kozerke. Reconstruction of divergence-free velocity fields from cine 3D phase-contrast flow measurements. *Magnetic Resonance in Medicine*, 69(1):200–210, jan 2013.

[22] F. M. Callaghan, R. Kozor, A. G. Sherrah, M. Vallely, D. Celermajer, G. A. Figtree, and S. M. Grieve. Use of multi-velocity encoding 4d flow mri to improve quantification of flow patterns in the aorta. *Journal of Magnetic Resonance Imaging*, 43(2):352–363, 2016.

[23] A. Can and R. Du. Association of hemodynamic factors with intracranial aneurysm formation and rupture: systematic review and meta-analysis. *Neurosurgery*, 78(4):510–520, 2015.

[24] C. Canstein, P. Cachot, A. Faust, A. Stalder, J. Bock, A. Frydrychowicz, J. Küffer, J. Hennig, and M. Markl. 3D MR flow analysis in realistic rapid-prototyping model systems of the thoracic aorta: Comparison with in vivo data and computational fluid dynamics in identical vessel geometries. *Magnetic Resonance in Medicine*, 59(3):535–546, mar 2008.

[25] B. Casas, J. Lantz, P. Dyverfeldt, and T. Ebbers. 4D Flow MRI-based pressure loss estimation in stenotic flows: Evaluation using numerical simulations. *Magnetic Resonance in Medicine*, 75(4):1808–1821, apr 2016.

[26] M. A. Castro, C. M. Putman, M. Sheridan, and J. Cebral. Hemodynamic

patterns of anterior communicating artery aneurysms: a possible association with rupture. *American journal of neuroradiology*, 30(2):297–302, 2009.

[27] J. R. Cebral, C. M. Putman, M. T. Alley, T. Hope, R. Bammer, and F. Calamante. Hemodynamics in normal cerebral arteries: qualitative comparison of 4d phase-contrast magnetic resonance and image-based computational fluid dynamics. *Journal of engineering mathematics*, 64(4):367, 2009.

[28] A. Chatterjee. An introduction to the proper orthogonal decomposition. *Current science*, 78(7):808–817, 2000.

[29] W. Chen, C. T. Sica, and C. H. Meyer. Fast conjugate phase image reconstruction based on a chebyshev approximation to correct for b0 field inhomogeneity and concomitant gradients. *Magnetic resonance in medicine*, 60(5):1104–1111, 2008.

[30] C. P. Cheng, D. Parker, and C. A. Taylor. Quantification of wall shear stress in large blood vessels using lagrangian interpolation functions with cine phase-contrast magnetic resonance imaging. *Annals of biomedical engineering*, 30(8):1020–1032, 2002.

[31] J. Y. Cheng, J. M. Santos, and J. M. Pauly. Fast concomitant gradient field and field inhomogeneity correction for spiral cardiac imaging. *Magnetic resonance in medicine*, 66(2):390–401, 2011.

[32] M. Cibis, K. Jarvis, M. Markl, M. Rose, C. Rigsby, A. J. Barker, and J. J. Wentzel. The effect of resolution on viscous dissipation measured with 4D flow MRI in patients with Fontan circulation: Evaluation using computational fluid dynamics. *Journal of Biomechanics*, 48:2984–2989, 2015.

[33] M. Cibis, W. V. Potters, M. Selwaness, F. J. Gijsen, O. H. Franco, A. M. Arias Lorza, M. de Bruijne, A. Hofman, A. van der Lugt, A. J. Nederveen,

and J. J. Wentzel. Relation between wall shear stress and carotid artery wall thickening MRI versus CFD. *Journal of Biomechanics*, 49(5):735–741, mar 2016.

[34] R. R. Coifman and D. L. Donoho. *Translation-invariant de-noising*. Springer, 1995.

[35] R. Cusack and N. Papadakis. New Robust 3-D Phase Unwrapping Algorithms: Application to Magnetic Field Mapping and Undistorting Echoplanar Images. *NeuroImage*, 16(3):754–764, 2002.

[36] M. Darwish and F. Moukalled. A fully coupled navier-stokes solver for fluid flow at all speeds. *Numerical Heat Transfer, Part B: Fundamentals*, 65(5):410–444, 2014.

[37] P. F. Davies, A. Remuzzitt, E. J. Gordon, C. F. Dewey, and M. A. Gimbrone. Turbulent fluid shear stress induces vascular endothelial cell turnover in vitro (hemodynamic forces/endothelial growth control/atherosclerosis). *Cell Biology*, 83:2114–2117, 1986.

[38] N. de Hoon, R. van Pelt, A. Jalba, and A. Vilanova. 4D MRI Flow Coupled to Physics-Based Fluid Simulation for Blood-Flow Visualization. *Computer Graphics Forum*, 33(3):121–130, jun 2014.

[39] D. L. Donoho and I. M. Johnstone. Ideal spatial adaptation by wavelet shrinkage. *Biometrika*, 81(3):425–455, sep 1994.

[40] D. L. Donoho and I. M. Johnstone. Adapting to Unknown Smoothness via Wavelet Shrinkage. *Journal of the American Statistical Association*, 90(432):1200–1224, dec 1995.

[41] R. M. D'Souza, A. Bakhshinejad, A. Baghaie, and V. L. Rayz. Reconstructing high fidelity hemodynamic flow fields by merging patient-specific computa-

tional fluid dynamics (cfd) and 4d phase contrast magnetic resonance data. In *ISMRM Workshop on Quantitative MR Flow: Innovation & Implementation for Clinical & Physiological Insights, San Francisco, CA, USA*, 2016.

[42] Y. P. Du, X. Joe Zhou, and M. A. Bernstein. Correction of concomitant magnetic field-induced image artifacts in nonaxial echo-planar imaging. *Magnetic resonance in medicine*, 48(3):509–515, 2002.

[43] T. Ebbers, H. Haraldsson, P. Dyverfeldt, A. Sigfridsson, M. J. B. Warntjes, and L. Wigström. Higher order weighted least-squares phase offset correction for improved accuracy in phase-contrast MRI. In *ISMRM*, 2008.

[44] J. Eriksson, A. F. Bolger, T. Ebbers, and C.-J. Carlhäll. Four-dimensional blood flow-specific markers of LV dysfunction in dilated cardiomyopathy. *European heart journal cardiovascular Imaging*, 14(5):417–24, may 2013.

[45] J. Eriksson, C. J. Carlhäll, P. Dyverfeldt, J. Engvall, A. F. Bolger, and T. Ebbers. Semi-automatic quantification of 4d left ventricular blood flow. *Journal of Cardiovascular Magnetic Resonance*, 12(1):9, 2010.

[46] G. Evensen. The Ensemble Kalman Filter: theoretical formulation and practical implementation. *Ocean Dynamics*, 53(4):343–367, nov 2003.

[47] M. F. Fathi, A. Bakhshinejad, A. Baghaie, D. Saloner, R. H. Sacho, V. L. Rayz, and R. M. D'Souza. Denoising and Spatial Resolution Enhancement of 4D Flow MRI Using Proper Orthogonal Decomposition and Lasso Regularization. *Computerized Medical Imaging and Graphics*, aug 2018.

[48] J. U. Fluckiger, J. J. Goldberger, D. C. Lee, J. Ng, R. Lee, A. Goyal, and M. Markl. Left atrial flow velocity distribution and flow coherence using four-dimensional FLOW MRI: a pilot study investigating the impact of age and

Pre- and Postintervention atrial fibrillation on atrial hemodynamics. *Journal of magnetic resonance imaging : JMRI*, 38(3):580–7, sep 2013.

[49] M. D. Ford, H. N. Nikolov, J. S. Milner, S. P. Lownie, E. M. DeMont, W. Kalata, F. Loth, D. W. Holdsworth, and D. A. Steinman. PIV-Measured Versus CFD-Predicted Flow Dynamics in Anatomically Realistic Cerebral Aneurysm Models. *Journal of Biomechanical Engineering*, 130(2):021015, 2008.

[50] A. Frydrychowicz, M. Markl, D. Hirtler, A. Harloff, C. Schlensak, J. Geiger, B. Stiller, and R. Arnold. Aortic hemodynamics in patients with and without repair of aortic coarctation: in vivo analysis by 4D flow-sensitive magnetic resonance imaging. *Investigative radiology*, 46(5):317–25, may 2011.

[51] A. Frydrychowicz, A. F. Stalder, M. F. Russe, J. Bock, S. Bauer, A. Harloff, A. Berger, M. Langer, J. Hennig, and M. Markl. Three-dimensional analysis of segmental wall shear stress in the aorta by flow-sensitive four-dimensional-mri. *Journal of Magnetic Resonance Imaging: An Official Journal of the International Society for Magnetic Resonance in Medicine*, 30(1):77–84, 2009.

[52] A. Fyrenius, L. Wigström, T. Ebbers, M. Karlsson, J. Engvall, and A. F. Bolger. Three dimensional flow in the human left atrium. *Heart (British Cardiac Society)*, 86(4):448–55, oct 2001.

[53] U. Galvanetto and G. Violaris. Numerical investigation of a new damage detection method based on proper orthogonal decomposition. *Mechanical Systems and Signal Processing*, 21(3):1346–1361, 2007.

[54] M. Gavish and D. L. Donoho. The optimal hard threshold for singular values is $4/\sqrt{3}$. *IEEE Transactions on Information Theory*, 60(8):5040–5053, Aug 2014.

[55] G. H. Golub and C. Reinsch. Singular value decomposition and least squares solutions. *Numerische mathematik*, 14(5):403–420, 1970.

[56] L. Graftieaux, M. Michard, and N. Grosjean. Combining PIV, POD and vortex identification algorithms for the study of unsteady turbulent swirling flows. *Measurement Science and Technology*, 12(9):1422–1429, sep 2001.

[57] H. Gudbjartsson and S. Patz. The rician distribution of noisy mri data. *Magnetic resonance in medicine*, 34(6):910–914, 1995.

[58] S. Gupta and J. Prince. On div-curl regularization for motion estimation in 3-D volumetric imaging. In *Proceedings of 3rd IEEE International Conference on Image Processing*, volume 1, pages 929–932. IEEE, 1996.

[59] A. Harloff, F. Albrecht, J. Spreer, A. F. Stalder, J. Bock, A. Frydrychowicz, J. Schöllhorn, A. Hetzel, M. Schumacher, J. Hennig, and M. Markl. 3D blood flow characteristics in the carotid artery bifurcation assessed by flow-sensitive 4D MRI at 3T. *Magnetic resonance in medicine*, 61(1):65–74, jan 2009.

[60] Y. Hoi, S. H. Woodward, M. Kim, D. B. Taulbee, and H. Meng. Validation of CFD Simulations of Cerebral Aneurysms With Implication of Geometric Variations. *Journal of Biomechanical Engineering*, 128(6):844, jun 2006.

[61] P. Holmes, J. L. Lumley, and G. Berkooz. *Turbulence, Coherent Structures, Dynamical Systems and Symmetry:*. Cambridge University Press, Cambridge, 1996.

[62] M. D. Hope, T. A. Hope, S. E. Crook, K. G. Ordovas, T. H. Urbania, M. T. Alley, and C. B. Higgins. 4D Flow CMR in Assessment of Valve-Related Ascending Aortic Disease. *JACC: Cardiovascular Imaging*, 4(7):781–787, 2011.

[63] M. D. Hope, T. A. Hope, A. K. Meadows, K. G. Ordovas, T. H. Urbania, M. T. Alley, and C. B. Higgins. Bicuspid aortic valve: four-dimensional MR

evaluation of ascending aortic systolic flow patterns. *Radiology*, 255(1):53–61, apr 2010.

[64] H. W. Jeong, J. H. Seo, S. T. Kim, C. K. Jung, and S.-I. Suh. Clinical practice guideline for the management of intracranial aneurysms. *Neurointervention*, 9(2):63–71, sep 2014.

[65] K. M. Johnson and M. Markl. Improved SNR in phase contrast velocimetry with five-point balanced flow encoding. *Magnetic resonance in medicine*, 63(2):349–55, Feb 2010.

[66] Y. M. Kadah and X. Hu. Simulated phase evolution rewinding (sphere): a technique for reducing b0 inhomogeneity effects in mr images. *Magnetic Resonance in Medicine*, 38(4):615–627, 1997.

[67] R. E. Kalman. A New Approach to Linear Filtering and Prediction Problems. *Journal of Basic Engineering*, 82(1):35, 1960.

[68] N. Kaneko, T. Mashiko, K. Namba, S. Tateshima, E. Watanabe, and K. Kawai. A patient-specific intracranial aneurysm model with endothelial lining: a novel in vitro approach to bridge the gap between biology and flow dynamics. *Journal of neurointerventional surgery*, 10(3):306–309, mar 2018.

[69] E. I. Kao. *Complementary 4D-Flow and CFD Analysis Methods for Investigating Pathological Hemodynamics*. PhD thesis, UC Berkeley, 2017.

[70] G. Kerschen, J.-c. Golinval, A. F. VAKAKIS, and L. A. BERGMAN. The Method of Proper Orthogonal Decomposition for Dynamical Characterization and Order Reduction of Mechanical Systems: An Overview. *Nonlinear Dynamics*, 41(1-3):147–169, aug 2005.

[71] P. J. Kilner, G.-Z. Yang, A. J. Wilkes, R. H. Mohiaddin, D. N. Firmin, and

M. H. Yacoub. Asymmetric redirection of flow through the heart. *Nature*, 404(6779):759–761, apr 2000.

[72] U. Köhler, I. Marshall, M. B. Robertson, Q. Long, X. Y. Xu, and P. R. Hoskins. MRI measurement of wall shear stress vectors in bifurcation models and comparison with CFD predictions. *Journal of Magnetic Resonance Imaging*, 14(5):563–573, nov 2001.

[73] U. Köhler, I. Marshall, M. B. Robertson, Q. Long, X. Y. Xu, and P. R. Hoskins. Mri measurement of wall shear stress vectors in bifurcation models and comparison with cfd predictions. *Journal of Magnetic Resonance Imaging: An Official Journal of the International Society for Magnetic Resonance in Medicine*, 14(5):563–573, 2001.

[74] T. S. Koltukluoglu, S. Hirsch, C. Binter, S. Kozerke, G. Szekely, and A. Laadhari. A robust comparison approach of velocity data between MRI and CFD based on divergence-free space projection. In *2015 IEEE 12th International Symposium on Biomedical Imaging (ISBI)*, pages 1393–1397. IEEE, apr 2015.

[75] Z. Kulcsár, A. Ugron, Z. Berentei, G. Paál, I. Szikora, et al. Hemodynamics of cerebral aneurysm initiation: the role of wall shear stress and spatial wall shear stress gradient. *American Journal of neuroradiology*, 2011.

[76] F. Lanata and A. D. Grosso. Damage detection and localization for continuous static monitoring of structures using a proper orthogonal decomposition of signals. *Smart Materials and Structures*, 15(6):1811–1829, dec 2006.

[77] E. Liberge and A. Hamdouni. Reduced order modelling method via proper orthogonal decomposition (POD) for flow around an oscillating cylinder. *Journal of Fluids and Structures*, 26(2):292–311, 2010.

[78] M. Loecher, E. Schrauben, K. M. Johnson, and O. Wieben. Phase unwrapping in 4d mr flow with a 4d single-step laplacian algorithm. *Journal of Magnetic Resonance Imaging*, 43(4):833–842, 2016.

[79] R. Lorenz, J. Bock, J. Snyder, J. G. Korvink, B. A. Jung, and M. Markl. Influence of eddy current, Maxwell and gradient field corrections on 3D flow visualization of 3D CINE PC-MRI data. *Magnetic Resonance in Medicine*, 72(1):33–40, jul 2014.

[80] S. Lowitzsch. *Approximation and interpolation employing divergence-free radial basis functions with applications*. PhD thesis, 2002.

[81] G. Y. Lu and D. W. Wong. An adaptive inverse-distance weighting spatial interpolation technique. *Computers & Geosciences*, 34(9):1044–1055, 2008.

[82] A. M. Malek, S. L. Alper, and S. Izumo. Hemodynamic shear stress and its role in atherosclerosis. *Jama*, 282(21):2035–2042, 1999.

[83] L.-C. Man, J. M. Pauly, and A. Macovski. Multifrequency interpolation for fast off-resonance correction. *Magnetic resonance in medicine*, 37(5):785–792, 1997.

[84] M. Markl, R. Bammer, M. Alley, C. Elkins, M. Draney, A. Barnett, M. Moseley, G. Glover, and N. Pelc. Generalized reconstruction of phase contrast MRI: Analysis and correction of the effect of gradient field distortions. *Magnetic Resonance in Medicine*, 50(4):791–801, oct 2003.

[85] M. Markl, A. Frydrychowicz, S. Kozerke, M. Hope, and O. Wieben. 4D flow MRI. *Journal of Magnetic Resonance Imaging*, 36(5):1015–1036, nov 2012.

[86] M. Markl, F. Wegent, T. Zech, S. Bauer, C. Strecker, M. Schumacher, C. Weiller, J. Hennig, and A. Harloff. In vivo wall shear stress distribution in the carotid artery: effect of bifurcation geometry, internal carotid

artery stenosis, and recanalization therapy. *Circulation. Cardiovascular imaging*, 3(6):647–55, nov 2010.

[87] S. Meckel, L. Leitner, L. H. Bonati, F. Santini, T. Schubert, A. F. Stalder, P. Lyrer, M. Markl, and S. G. Wetzel. Intracranial artery velocity measurement using 4D PC MRI at 3 T: comparison with transcranial ultrasound techniques and 2D PC MRI. *Neuroradiology*, 55(4):389–98, mar 2013.

[88] H. Meng, V. Tutino, J. Xiang, and A. Siddiqui. High wss or low wss? complex interactions of hemodynamics with intracranial aneurysm initiation, growth, and rupture: toward a unifying hypothesis. *American Journal of Neuroradiology*, 2013.

[89] J. S. Milner, J. A. Moore, B. K. Rutt, and D. A. Steinman. Hemodynamics of human carotid artery bifurcations: Computational studies with models reconstructed from magnetic resonance imaging of normal subjects. *Journal of Vascular Surgery*, 28(1):143–156, 1998.

[90] F. Moukalled, L. Mangani, and M. Darwish. *The Finite Volume Method in Computational Fluid Dynamics : an Advanced Introduction with OpenFOAM® and Matlab*. Springer International Publishing, 1 edition, 2015.

[91] A. M. Nixon, M. Gunel, and B. E. Sumpio. The critical role of hemodynamics in the development of cerebral vascular disease: a review. *Journal of neurosurgery*, 112(6):1240–1253, 2010.

[92] D. C. Noll, C. H. Meyer, J. M. Pauly, D. G. Nishimura, and A. Macovski. A homogeneity correction method for magnetic resonance imaging with time-varying gradients. *IEEE transactions on medical imaging*, 10(4):629–637, 1991.

[93] D. G. Norris and J. M. Hutchison. Concomitant magnetic field gradients and their effects on imaging at low magnetic field strengths. *Magnetic resonance imaging*, 8(1):33–37, 1990.

[94] F. Ong, M. Uecker, U. Tariq, A. Hsiao, M. Alley, S. Vasanawala, and M. Lustig. Improved visualization and quantification of 4D flow MRI data using divergence-freewavelet denoising. In *2013 IEEE 10th International Symposium on Biomedical Imaging*, pages 1186–1189. IEEE, apr 2013.

[95] F. Ong, M. Uecker, U. Tariq, A. Hsiao, M. Alley, S. Vasanawala, and M. Lustig. Compressed sensing 4d flow reconstruction using divergence-free wavelet transform. In *Proceedings of international society for magnetic resonance in medicine*, volume 22, page 0326, 2014.

[96] F. Ong, M. Uecker, U. Tariq, A. Hsiao, M. T. Alley, S. S. Vasanawala, and M. Lustig. Robust 4D flow denoising using divergence-free wavelet transform. *Magnetic resonance in medicine*, 73(2):828–42, feb 2015.

[97] J. N. Oshinski, J. L. Curtin, and F. Loth. Mean-average wall shear stress measurements in the common carotid artery. *Journal of cardiovascular magnetic resonance*, 8(5):717–722, 2006.

[98] S. Oyre, S. Ringgaard, S. Kozerke, W. P. Paaske, M. Erlandsen, P. Boesiger, and E. M. Pedersen. Accurate noninvasive quantitation of blood flow, cross-sectional lumen vessel area and wall shear stress by three-dimensional paraboloid modeling of magnetic resonance imaging velocity data. *Journal of the American College of Cardiology*, 32(1):128–134, 1998.

[99] S. Petersson, P. Dyverfeldt, and T. Ebbers. Assessment of the accuracy of mri wall shear stress estimation using numerical simulations. *Journal of Magnetic Resonance Imaging*, 36(1):128–138, 2012.

[100] M. Raschi, F. Mut, G. Byrne, C. M. Putman, S. Tateshima, F. Viñuela, T. Tanoue, K. Tanishita, and J. R. Cebral. CFD and PIV analysis of hemodynamics in a growing intracranial aneurysm. *International journal for numerical methods in biomedical engineering*, 28(2):214–28, feb 2012.

[101] V. L. Rayz, A. Abla, L. Boussel, J. R. Leach, G. Acevedo-Bolton, D. Saloner, and M. T. Lawton. Computational Modeling of Flow-Altering Surgeries in Basilar Aneurysms. *Annals of Biomedical Engineering*, 43(5):1210–1222, may 2015.

[102] V. L. Rayz, L. Boussel, G. Acevedo-Bolton, A. J. Martin, W. L. Young, M. T. Lawton, R. Higashida, and D. Saloner. Numerical Simulations of Flow in Cerebral Aneurysms: Comparison of CFD Results and In Vivo MRI Measurements. *Journal of Biomechanical Engineering*, 130(5):051011, 2008.

[103] V. C. Rispoli, J. F. Nielsen, K. S. Nayak, and J. L. A. Carvalho. Computational fluid dynamics simulations of blood flow regularized by 3D phase contrast MRI. *Biomedical engineering online*, 14(1):110, jan 2015.

[104] M. Salfity, J. Huntley, M. Graves, O. Marklund, R. Cusack, and D. Beauregard. Extending the dynamic range of phase contrast magnetic resonance velocity imaging using advanced higher-dimensional phase unwrapping algorithms. *Journal of The Royal Society Interface*, 3(8):415–427, 2006.

[105] C. Santelli, M. Loecher, J. Busch, O. Wieben, T. Schaeffter, and S. Kozerke. Accelerating 4d flow mri by exploiting vector field divergence regularization. *Magnetic resonance in medicine*, 75(1):115–125, 2016.

[106] S. Schnell, J. Garcia, C. Wu, and M. Markl. Dual-velocity encoding phase-contrast mri: extending the dynamic range and lowering the velocity to noise ratio. In *Proc. Intl. Soc. Mag. Reson. Med*, volume 23, page 4546, 2015.

[107] H. Schomberg. Off-resonance correction of mr images. *IEEE transactions on medical imaging*, 18(6):481–495, 1999.

[108] J. K. Seo and E. J. E. J. Woo. *Nonlinear inverse problems in imaging*. Wiley, 2013.

[109] M. Sigovan, V. Rayz, W. Gasper, H. F. Alley, C. D. Owens, and D. Saloner. Vascular remodeling in autogenous arterio-venous fistulas by mri and cfd. *Annals of biomedical engineering*, 41(4):657–668, 2013.

[110] L. Sirovich. Method of snapshots. *Q. Appl. Math*, 45:561–571, 1987.

[111] O. Skrinjar, A. Bistoquet, J. Oshinski, K. Sundareswaran, D. Frakes, and A. Yoganathan. A divergence-free vector field model for imaging applications. In *Biomedical Imaging: From Nano to Macro, 2009. ISBI'09. IEEE International Symposium on*, pages 891–894. IEEE, 2009.

[112] H. Sohn and C. R. Farrar. Damage diagnosis using time series analysis of vibration signals. *Smart Materials and Structures*, 10(3):446–451, jun 2001.

[113] S. M. Song, S. Napel, G. H. Glover, and N. J. Pelc. Noise reduction in three-dimensional phase-contrast MR velocity measurementsl. *Journal of Magnetic Resonance Imaging*, 3(4):587–596, jul 1993.

[114] S. M. Song, S. Napel, N. J. Pelc, and G. H. Glover. Phase unwrapping of mr phase images using poisson equation. *IEEE Transactions on Image Processing*, 4(5):667–676, 1995.

[115] A. F. Stalder, M. Russe, A. Frydrychowicz, J. Bock, J. Hennig, and M. Markl. Quantitative 2d and 3d phase contrast mri: optimized analysis of blood flow and vessel wall parameters. *Magnetic resonance in medicine*, 60(5):1218–1231, 2008.

[116] D. A. Steinman, J. S. Milner, C. J. Norley, S. P. Lownie, and D. W. Holdsworth. Image-Based Computational Simulation of Flow Dynamics in a Giant Intracranial Aneurysm. *AJNR Am. J. Neuroradiol.*, 24(4):559–566, apr 2003.

[117] D. Suter and F. Chen. Left ventricular motion reconstruction based on elastic vector splines. *IEEE Transactions on Medical Imaging*, 19(4):295–305, apr 2000.

[118] P. D. Tafti, R. Delgado-Gonzalo, A. F. Stalder, and M. Unser. Variational enhancement and denoising of flow field images. In *2011 IEEE International Symposium on Biomedical Imaging: From Nano to Macro*, pages 1061–1064. IEEE, mar 2011.

[119] P. D. Tafti and M. Unser. On Regularized Reconstruction of Vector Fields. *IEEE Transactions on Image Processing*, 20(11):3163–3178, nov 2011.

[120] C. Tang, D. D. Blatter, and D. L. Parker. Accuracy of phase-contrast flow measurements in the presence of partial-volume effects. *Journal of Magnetic Resonance Imaging*, 3(2):377–385, 1993.

[121] Y. Tao, G. Rilling, M. Davies, and I. Marshall. Carotid blood flow measurement accelerated by compressed sensing: validation in healthy volunteers. *Magnetic resonance imaging*, 31(9):1485–91, nov 2013.

[122] J. B. Thomas, J. S. Milner, B. K. Rutt, and D. A. Steinman. Reproducibility of image-based computational fluid dynamics models of the human carotid bifurcation. *Annals of Biomedical Engineering*, 31(2):132–141, feb 2003.

[123] J. Töger, M. Carlsson, G. Söderlind, H. Arheden, and E. Heiberg. Volume tracking: A new method for quantitative assessment and visualization of in-

tracardiac blood flow from three-dimensional, time-resolved, three-component magnetic resonance velocity mapping. *BMC Medical Imaging*, 11(1):10, 2011.

[124] J. Tu, D. Luchtenberg, C. Rowley, S. Brunton, and J. Kutz. Generalizing dynamic mode decomposition to a larger class of datasets. *Journal of Computational Dynamics*, 2013.

[125] M. Untenberger, M. Hüllebrand, L. Tautz, A. A. Joseph, D. Voit, K. D. Merboldt, and J. Frahm. Spatiotemporal phase unwrapping for real-time phase-contrast flow mri. *Magnetic resonance in medicine*, 74(4):964–970, 2015.

[126] A. Vali, A. A. Abla, M. T. Lawton, D. Saloner, and V. L. Rayz. CFD modeling of contrast transport in basilar aneurysm following flow-altering surgeries. *Journal of Biomechanics*, 0(0):409–417, nov 2016.

[127] M. W. Vernooij, M. A. Ikram, H. L. Tanghe, A. J. Vincent, A. Hofman, G. P. Krestin, W. J. Niessen, M. M. Breteler, and A. van der Lugt. Incidental Findings on Brain MRI in the General Population. *New England Journal of Medicine*, 357(18):1821–1828, nov 2007.

[128] F. von Knobelsdorff-Brenkenhoff, R. F. Trauzeddel, A. J. Barker, H. Gruettner, M. Markl, and J. Schulz-Menger. Blood flow characteristics in the ascending aorta after aortic valve replacement–a pilot study using 4D-flow MRI. *International journal of cardiology*, 170(3):426–33, jan 2014.

[129] P. G. Walker, G. B. Cranney, M. B. Scheidegger, G. Waseleski, G. M. Pohost, and A. P. Yoganathan. Semiautomated method for noise reduction and background phase error correction in MR phase velocity data. *Journal of Magnetic Resonance Imaging*, 3(3):521–530, may 1993.

[130] G. Welch and G. Bishop. An Introduction to the Kalman Filter. 2006.

[131] H. G. Weller, G. Tabor, H. Jasak, and C. Fureby. A tensorial approach to computational continuum mechanics using object-oriented techniques. *Computers in Physics*, 12(6):620, 11 1998.

[132] A. L. Wentland, T. M. Grist, and O. Wieben. Repeatability and internal consistency of abdominal 2D and 4D phase contrast MR flow measurements. *Academic radiology*, 20(6):699–704, jun 2013.

[133] L. Wigstrom, T. Ebbers, A. Fyrenius, M. Karlsson, J. Engvall, B. Wranne, and A. F. Bolger. Particle trace visualization of intracardiac flow using time-resolved 3D phase contrast MRI. *Magnetic Resonance in Medicine*, 41(4):793–799, apr 1999.

[134] Q.-S. Xiang. Temporal phase unwrapping for cine velocity imaging. *Journal of Magnetic Resonance Imaging*, 5(5):529–534, sep 1995.

[135] G. Z. Yang, P. Burger, P. J. Kilner, S. P. Karwatowski, and D. N. Firmin. Dynamic range extension of cine velocity measurements using motion registered spatiotemporal phase unwrapping. *Journal of Magnetic Resonance Imaging*, 6(3):495–502, 1996.

[136] T. I. Yiallourou, J. R. Kröger, N. Stergiopulos, D. Maintz, B. A. Martin, and A. C. Bunck. Comparison of 4D Phase-Contrast MRI Flow Measurements to Computational Fluid Dynamics Simulations of Cerebrospinal Fluid Motion in the Cervical Spine. *PLoS ONE*, 7(12), 2012.

[137] J. Zajac, J. Eriksson, P. Dyverfeldt, A. F. Bolger, T. Ebbers, and C.-J. Carlhäll. Turbulent kinetic energy in normal and myopathic left ventricles. *Journal of Magnetic Resonance Imaging*, 41(4):1021–1029, apr 2015.

[138] I. Zbicinski, N. Veshkina, and L. Stefańczyk. 4d model of hemodynamics in the

abdominal aorta. *Bio-medical materials and engineering*, 26(s1):S257–S264, 2015.

[139] G. Zhou, Y. Zhu, Y. Yin, M. Su, and M. Li. Association of wall shear stress with intracranial aneurysm rupture: systematic review and meta-analysis. *Scientific Reports*, 7(1):5331, dec 2017.

Ali Bakhshinejad

Education

University of Wisconsin-Milwaukee **Milwaukee - USA**
Doctor of Philosophy *2014–2018*

University of Iceland (HI) **Reykjavik - Iceland**
Master of Science - Mechanical Engineering *June 2013*
First Class Honors

University of Yasouj **Yasouj - Iran**
Bachelor of Science - Mechanical Engineering *June 2008*

Professional Experience

Medical College Of Wisconsin **Milwaukee - USA**
Research Scientist *Nov 2017 – May 2018*
Project: The purpose of this project was to research, develop, and implementation of 4D flow MRI data processing using CFD on newly diagnosed brain aneurysm patients.

University of Wisconsin-Milwaukee **Milwaukee - USA**
Research Assistant *2014–Present*
Project: The aim of the project is to de-noise 4D flow MRI data as well as enhance their resolution for that I did:

- Developed an algorithm using Proper Orthogonal Decomposition (POD) to de-noise 4D flow MRI data.
- Developed a parallel algorithm using Ensemble Kalman Filter (EnKF) to de-noise 4D flow MRI data.
- Developed a parallel simulation pipeline using Open∇FOAM and Octave on a computational grid using HTCondor to simulate blood flow in the brain for patient specific geometries.
- Developed a solver using Open∇FOAM and MATLAB to calculate blood resident time in vessel based on the patient specific velocity field using 4D MRI data.

University of Iceland **Reykjavik - Iceland**
Research Assistant *2013*

- Designed a heat sink for sampling vessel in order to work in high temperature/pressure geothermal wells using MATLAB and ANSYS Fluent.
- Studied the behavior of brine inside the geothermal wells to improve well's structure.

Certificates

2016: **OpenFOAM: Programming CFD** CFD Direct Ltd

2016: **Winter 2016 I-Corps Program** Milwaukee I-Corps site

Computer skills

Advanced: OpenFOAM, LAMMPS, ANSYS CFX, FLUENT, CATIA V5, CAESAR II, MATLAB, Wolfram Mathematica, Octave , LaTeX

Intermediate: Python, Shell scripting, CUDA C, OpenMP, MPI, C/C++, VB programming

Awards

2016/2017: Best poster award at UWM College of Engineering & Applied Science poster competition sponsored by GE Healthcare.

2016: Biomedical Engineering Society (BMES) Graduate Design and Research Awards

from the BMES Annual Meeting in Minneapolis, MN.

2016: University of Wisconsin Milwaukee graduate student travel award to attend to the BMES 2016 in Minneapolis, MN.

2016: Second place at IEEE Larry Hause student poster competition 2016.

2016: I-Corps award for AlphaCore Solutions start-up idea.

2015: UWM College of Engineering & Applied Science Dean's Scholarship.

2014: UWM College of Engineering & Applied Science Dean's Scholarship.

2014: University of Iceland's travel award to attend to the Thirty-Eight Workshop on Geothermal Reservoir Engineering Stanford University.

Invited Talks

[T4]: **Ali Bakhshinejad**, *4D Flow MRI Resolution Enhancement Methods*, February 2018, Translation and Molecular Imaging Institute (TMII), Icahn school of medicine at Mount Sinai.

[T3]: **Ali Bakhshinejad**, *what we talk about, when we talk about 4D Flow MRI*, UWRF Spring 2017 Lunch and learn.

[T2]: **Ali Bakhshinejad**, Ahmadreza Baghaie, Vitaliy L. Rayz and Roshan M. D'Souza, *A Novel Algorithm Towards Merging CFD and 4D Flow MRI data*, The 1st UWM Graduate Student Research Symposium for Math, Engineering, and the Natural Sciences

[T1]: **Ali Bakhshinejad**, *Numerical Simulations of Blood Flow in Patient-Specific Models of Cerebral Aneurysms*, Third Midwest OpenFOAM Users Group Meeting

Teaching Experience

[L3]: **Ali Bakhshinejad**, *Introduction to OpenFOAM*, University of Wisconsin-Milwaukee. http://uwm.edu/hpc/intro-to-openfoam/

[L3]: **Ali Bakhshinejad**, *Introduction to Finite Element Analysis*, University of Wisconsin-Milwaukee.

[L2]: **Ali Bakhshinejad**, *Hands-on experience - Potential Flow example*, Third Midwest OpenFOAM Users Group Meeting.

[L1]: **Ali Bakhshinejad**, *Introduction to C++ Programming Using OpenFOAM Libraries*, Third Midwest OpenFOAM Users Group Meeting.

Publication

Book Chapter

[B1]: **Bakhshinejad, A.**, Nezafati, M., Kim, C.-S., & D'Souza, R. M. (2018). Molecular Dynamics Simulation of Friction in Self-Lubricating Materials: An Overview of Theories and Available Models. In Self-Lubricating Composites (pp. 251-272). Berlin, Heidelberg: Springer Berlin Heidelberg.

Journal Article

[J4]: **Bakhshinejad A.**, Fathi M., Baghaie A., Nael K., Rayz V.L., D'Souza R.M. (2017) *4D Flow MRI Denoising and Spatial Resolution Enhancement: Application of Proper Orthogonal Decomposition Coupled with Dynamic Mode Decomposition*. Under review at the Journal of Biomechanics.

[J3]: Fathi, M. F., **Bakhshinejad, A.**, Baghaie, A., Saloner, D., Sacho, R. H., Rayz, V. L.,

& D'Souza, R. M. (2018). Denoising and Spatial Resolution Enhancement of 4D Flow MRI Using Proper Orthogonal Decomposition and Lasso Regularization. Computerized Medical Imaging and Graphics.
https://doi.org/10.1016/J.COMPMEDIMAG.2018.07.003

[J2]: **Bakhshinejad, A.**, Baghaie, A., Vali, A., Saloner, D., Rayz, V. L., & D'Souza, R. M. (2017). *Merging computational fluid dynamics and 4D Flow MRI using proper orthogonal decomposition and ridge regression*. Journal of Biomechanics, 58, 162-173.
https://doi.org/10.1016/j.jbiomech.2017.05.004

[J1]: **Ali Bakhshinejad**, Piroz Zamankhan, *Swirling flows in horizontally vibrated beds of dense granular materials*, Particuology, Available online 23 August 2012, ISSN 1674-2001, 10.1016/j.partic.2012.06.005.

Conference Presentations

[C5]: **Bakhshinejad, A.**, Fathi, M. F., Saloner, D., Nael, K., Rayz, V. L., & D'Souza, R. M. (2018). Case study: Coupling 4D-Flow MRI with CFD using Proper Orthogonal Decomposition and Dynamic Mode Decomposition. In 8th World Congress of Biomechanics. Dublin, Ireland.

[C4]: Roshan M. D'Souza, **Ali Bakhshinejad**, Ahmadreza Baghaie and Vitaliy L. Rayz *Reconstructing High Fidelity Hemodynamic Flow Fields by Merging Patient-Specific Computational Fluid Dynamics (CFD) and 4D Phase Contrast Magnetic Resonance Data*, ISMRM Workshop.

[C3]: **Ali Bakhshinejad**, Ahmadreza Baghaie, Vitaliy L. Rayz and Roshan M. D'Souza, *A proper orthogonal decomposition approach towards merging CFD and 4D-PCMR flow data*, The 28th Society for Magnetic Resonance Angiography

[C2]: **Bakhshinejad, A.**, & D'Souza, R. M. (2015). *A brief comparison between available bioprinting methods.* In 2015 IEEE Great Lakes Biomedical Conference (GLBC) (pp. 1-3). IEEE.
http://doi.org/10.1109/GLBC.2015.7158294

[C1]: **Bakhshinejad, A.**, Jonsson, M. Th., Palsson, H. *Numerical Model for Mist Separators.* Standford: Thirty-Eighth Workshop on Geothermal Reservoir Engineering Stanford University.

Poster Presentations

[P4]: **Bakhshinejad A.**, Rayz V.L and D'Souza R.M. *Post-processing 4D Flow MRI using Ensemble Kalman Filter* University of Wisconsin-Milwaukee: Graduate student poster competition 2017.

[P3]: **Ali Bakhshinejad**, Vitaliy L. Rayz and Roshan M. D'Souza, *Reconstructing Blood Velocity Profiles from Noisy 4D-PCMR Data using Ensemble Kalman Filtering*, BMES 2016 Annual Meeting. Selected as one of the five award winners.

[P2]: **Bakhshinejad, A.**, Baghaie A., Rayz V.L and D'Souza, R.M. *Towards Reconstructing Blood Velocity Profiles from Noisy and Sparse Time Resolved Phase Contrast Magnetic Resonance Flow Data* University of Wisconsin-Milwaukee: Graduate student poster competition 2016.

[P1]: **Bakhshinejad A.**, D'Souza R.M., Boussel L. and Rayz V.L *Contrast Agent Transport Simulations using 4D PC-MRI Derived Flow Fields* University of Wisconsin-Milwaukee: Graduate student poster competition 2015.

Review work

- BioMedical Engineering OnLine
- International Conference on Biological Information and Biomedical Engineering